ANALYSIS OF VADOSE ZONE WELL INJECTION PERFORMANCE

A Dissertation

by

CUITING QI

Submitted to the Graduate and Professional School of
Texas A&M University
in partial fulfillment of the requirements for the degree of

DOCTOR OF PHILOSOPHY

Chair of Committee,	Hongbin Zhan
Committee Members,	Peter Knappett
	David Sparks
	Huilin Gao
Head of Department,	Julie Newman

December 2021

Major Subject: Geophysics

ABSTRACT

Vadose zone well (VZW) injection is an effective method utilized in managed aquifer recharge and it plays an important role in semi-arid and arid regions. Accurately prediction of the recharge of VZW injection is still a challenge in the field of hydrology due to the nonlinear nature of the process in the vadose zone. To improve the water budget evaluation and management of VZW injection, three studies are conducted to investigate the influences of time-dependent ground surface flux (GSF) generated by infiltration or evapotranspiration on the VZW injection, the geometric and soil properties control on the recharge of VZW, and the subsurface heterogeneity control on the recharge of VZW. The semi-analytical solutions for the hydraulic head increments and recharge rate are derived for the coupled unsaturated-saturated governing equations by using Laplace-Hankel transforms. The analysis of the solutions indicates that GSF generated by infiltration can improve the recharge of VZW whereas GSF generated by evapotranspiration has the opposite influence. The influences of GSF on recharge of VZW are affected by the properties of the unsaturated zone. A finite-element numerical model based on the Van Genuchten-Mualem soil constitutive model is developed utilizing the COMSOL Multiphysics software to simulate VZW injection in a homogeneous aquifer and several numerical experiments are conducted to estimate the characteristic arrival time and cumulative recharge volume of injected water for different subsurface conditions. The simulation results indicate that coarser soils are beneficial to the recharge and the influences of well geometric properties (screen length and screen depth) on recharge are mainly reflected in affecting the travel distance of the injected water. The injection plan including the injection rate setting and schedule arrangement also has a great influence on recharge when the total volume of injected water is constant. A finite-element numerical model is developed with COMSOL Multiphysics to simulate VZW injection in a heterogeneous aquifer and the subsurface heterogeneity is conceived as the presence of a low permeable layer or lens. The presence of a low permeable layer in the aquifer hinders the infiltration of injected water and reduces recharge rate and cumulative recharge volume. These influences are affected by depth, lateral extension, thickness and hydraulic conductivity of the low permeable layer and the condition of whether the well screen cuts through the low permeable layer or lens. The knowledge of the influences of GSF, soil properties, geometric properties and subsurface heterogeneity on the recharge of VZW provides physically-based guidance for the design and management of VZWs.

ACKNOWLEDGEMENTS

I would like to express my sincere appreciation to my advisor, Dr. Hongbin Zhan, who has supervised me all though my PhD studies. Dr. Zhan gave me a lot of encouragement and helped me overcome many difficulties in my research. His enthusiasm and seriousness for research set an excellent example for me and encouraged me to improve myself continuously.

I would like to thank my committee members, Dr. Peter Knappett, Dr. David Sparks, and Dr. Huilin Gao, for their guidance and support throughout this research.

I would like to thank Dr. Chong Ma and Dr. Xiuyu Liang for their guidance of deriving the semi-analytical solutions. I would like to thank Dr. Yang Xian for his guidance in numerical modeling.

Finally, thanks to my parents and friends Tianyue Qu, Kaiyi Zhang, Renjie Zhou, Kewei Chen, Xin Peng, Xin Liu, Yinuo Wang, Zehao Chen, Yonghui Zhu, Kaixi Yang and Yun Tang for their support and encouragement during my studies and life.

CONTRIBUTORS AND FUNDING SOURCES

Contributors

This work was supported by a dissertation committee consisting of Professor Hongbin Zhan [advisor], Professor Peter Knappett, Professor David Sparks of the Department of Geology and Geophysics, and Professor Huilin Gao of the Department of Civil Engineering.

All work conducted for the dissertation was completed by the student independently.

Funding Sources

Graduate study was supported by financial aid from the Department of Geology and Geophysics, Texas A&M University and a graduate fellowship from ConocoPhillips Company.

NOMENCLATURE

Nomenclature of Chapter 2

a	initial unsaturated zone thickness [L]
b	initial saturated zone thickness [L]
$C(\theta)$	soil moisture capacity at water content θ [L^{-1}]
C_0(z)	zero-order approximation of the soil moisture capacity at the initial water content [L^{-1}]
d	elevation of the well screen bottom [L]
GSF	ground surface influx
$H(\cdot)$	Heaviside step function
h_s	hydraulic head in the saturated zone [L]
h_u	hydraulic head in the unsaturated zone [L]
$I(t)$	time-dependent ground surface flux generated by infiltration or evapotranspiration [LT^{-1}]
$J_0(\cdot)$	zero-order Bessel function of the first kind [-]
j	elevation of the well screen top [L]
K_r	saturated principal hydraulic conductivity in the horizontal (*r*) direction [LT^{-1}]
K_z	saturated principal hydraulic conductivity in the vertical (z) direction [LT^{-1}]
$k(\theta)$	relative hydraulic conductivity at water content θ [-]
k_0(z)	zero-order approximation of relative hydraulic conductivities at initial water contents [-]
p	parameter of the Laplace transformation [-]
Q	injection rate [L^3T^{-1}]

q	infiltration rate at the interface of unsaturated and saturated zones [LT^{-1}]
S_s	specific storage [L^{-1}]
S_y	drainable porosity or specific yield [-]
s	hydraulic head increment in the saturated zone [L]
t	time [T]
u	hydraulic head increment in the unsaturated zone [L]
ω	constitutive exponent of the unsaturated zone [L^{-1}]
θ	volumetric water content [-]
θ_r	residual water content [-]
θ_s	saturated water content [-]
$\Theta(z)$	Box function
ψ	pressure head in the unsaturated zone [L]
ψ_a	pressure head at which the aquifer starts to desaturate [L]
α	parameter of the Hankel transformation [-]
A, B, F	dummy parameters of solutions (2.30) - (2.41)
M, N, R	dummy parameters of solutions (2.30) - (2.41)
U_{10}, Y, η	dummy parameters of solutions (2.30) - (2.41)

Nomenclature of Chapters 3 and 4

a	initial unsaturated zone thickness [L]
B_c	the thickness of the clay loam layer [L]
b	initial saturated zone thickness [L]
C	the specific soil moisture capacity [L^{-1}]
D	the elevation head [L]
D_c	the depth of the top surface of the clay loam layer [L]
d	distance between the well screen bottom and the water table [L]
h_u	hydraulic head in the unsaturated zone [L]
h_0	initial hydraulic head [L]
J_0	the zero-order Bessel function of the first kind
j	distance between the well screen top and the water table [L]
$K(\theta)$	hydraulic conductivity at water content θ [LT^{-1}]
K_s	the saturated hydraulic conductivity [LT^{-1}]
k_r	the relative permeability [-]
l	the pore size interaction term of the VGM model [-]
m	shape parameter of the VGM model [-]
n	shape parameter of the VGM model [-]
p	the Laplace transform parameter
Q	injection rate of VZW [L^3T^{-1}]
Q_{wt}	water recharge rate at the initial water table [L^3T^{-1}]
R_c	the width of the clay loam layer [L]

S_e	the effective saturation [-]
S_s	the specific storage [L^{-1}]
S_y	the specific yield [-]
t	time [T]
t_a	the travel time of injected water to reach the saturated zone [T]
u	hydraulic head increment in the unsaturated zone [L]
V_{wt}	the cumulative recharge volume at the initial water table [L^3]
α	a parameter corresponding approximately to the inverse of the air-entry value [L^{-1}]
α_0	the parameter of the Hankel transformation
ω	constitutive exponent of the unsaturated zone [L^{-1}]
σ	recharge index which equals to the ratio of the volumetric recharge rate at the water table over the injection rate of VZW.
θ	volumetric water content [-]
θ_r	residual water content [-]
θ_s	saturated water content [-]
ψ	pressure head [L]
ψ_a	the air entry pressure head [L]

TABLE OF CONTENTS

LIST OF FIGURES

Page

LIST OF TABLES

Page

CHAPTER 1

INTRODUCTION

Despite the significant improvements in relevant infrastructure, updated water management plans and technological solutions improving water use efficiency, water scarcity remains a major constraint to socio-economic development and a threat to livelihoods in expanding portions of the world (Liu et al., 2017; WEF, 2019). Millions of families around the world are vulnerable to water scarcity or do not have access to clean and adequate drinking water (Tzanakakis et al., 2020). Causes of water scarcity are related to drought, overuse, anthropogenic pollution, physical distance to drinking water sources and political and social stress (Gude, 2017). Managed aquifer recharge (MAR) is one of the effective measures that can alleviate water scarcity to realize sustainable water management. MAR entails the intentional recharge and storage of water within an aquifer for subsequent recovery or for environmental benefits (Sprenger et al., 2017). MAR is a cross-cutting technology which can be applied to: 1) secure water supply (Ghayoumian et al., 2007; Karlsen et al., 2012; Lacher et al., 2014); 2) process and handle groundwater quality and quantity (Kuster et al., 2010; Sharma and Kennedy, 2017); and 3) protect and sustain groundwater dependent ecosystems (García-Menéndez et al., 2018; Shammas, 2008; Shi et al., 2016). MAR is expected to become increasingly important as growing populations require more water and greater storage capacity is needed to save water in times of surplus for use in times of shortage (Bouwer, 2002; Dillon, 2005; Dillon et al., 2010).

Based on storage and recharge techniques, Zhang et al. (2020) summarized that the five major categories of MAR techniques are: (1) spreading methods, (2) in-channel modifications, (3) recharge by wells or shafts and boreholes, (4) induced bank filtration, and (5) runoff harvesting. Figure 1-1 shows the schematic diagrams of these common MAR techniques. The application conditions are described in Table 1-1. Spreading methods are the most common and economical ways to implement MAR. These methods include infiltration ponds and basins, and soil aquifer treatment. In-channel modifications are techniques where rivers, streams or canals are modified to store water and to enhance vertical recharge. These methods include percolation ponds, and sand storage dams. The methods wells, shafts and boreholes include open wells and shafts, aquifer storage and recovery (ASR), and aquifer storage, transfer and recovery (ASTR). Induced bank filtration methods include bank filtration, which is extracting groundwater from a well near or under the surface water body to induce infiltration through the bank to improve the quality of recovered water. Runoff harvesting methods include rainwater harvesting. Rainwater is collected and redirected into a deep pit with percolation, and then reused by further purposes.

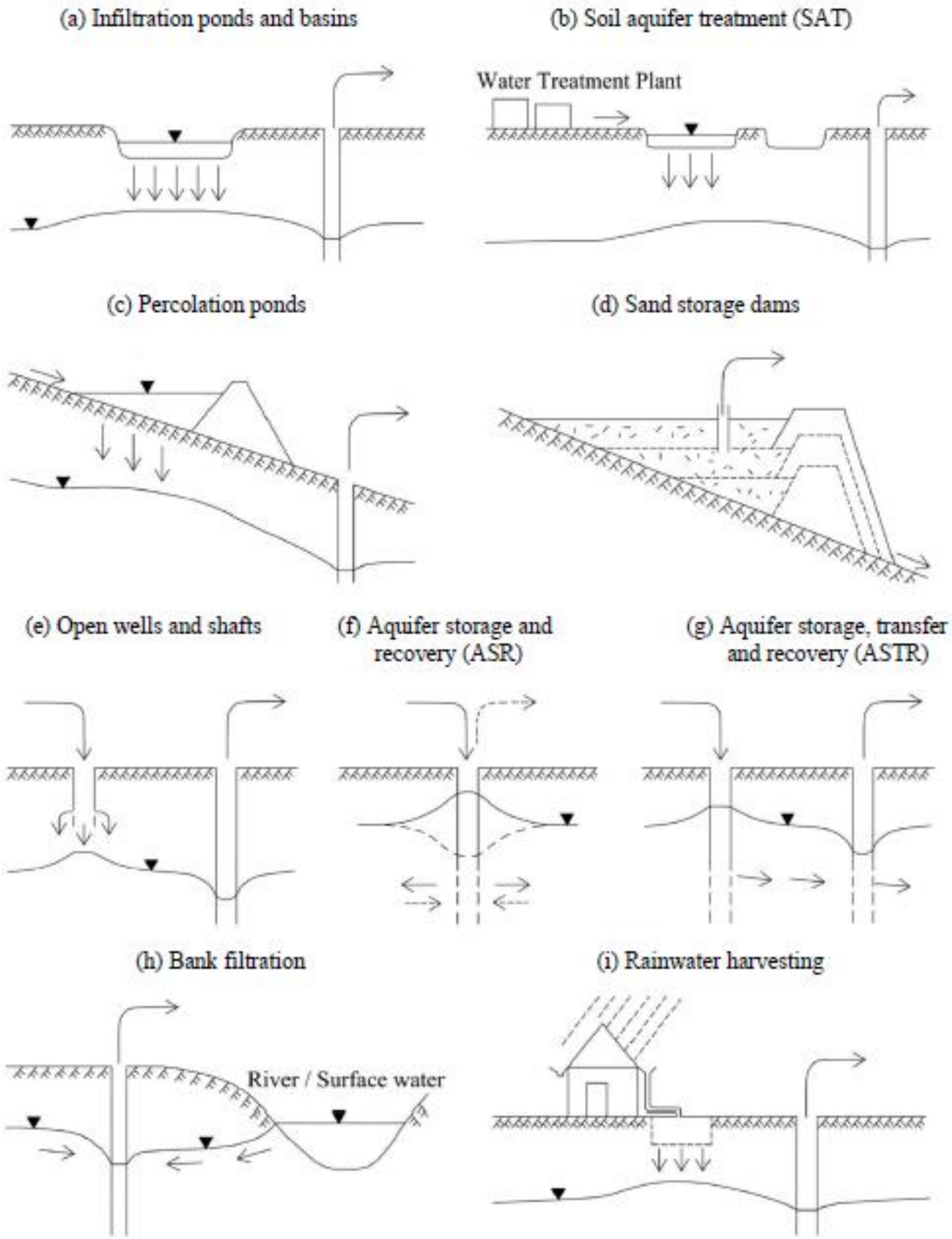

Figure 1-1 The schematic diagrams of common MAR techniques modified from Zhang et al. (2020)

Table 1-1 MAR technologies and their application conditions modified from Zhang et al. (2020)

Graph letter	MAR types	MAR sub-types	Applications
(a), (b)	Spreading methods	Infiltration ponds and basins; Soil aquifer treatment (SAT); Controlled flooding; Excess irrigation, ditches, trenches, sprinkler irrigation.	Where the unconfined aquifer to be recharged is at or near to the ground surface. Aquifer type: alluvium, sandstone and sometimes carbonate aquifers.
(c), (d)	In-channel modifications	Percolation ponds; gabions among others; Sand storage dams; Subsurface dams; Leaky dams and recharge releases.	Where it runs off in order to have water retention and storage. Especially used for flooding events.
(e), (f), (g)	Well, shaft and borehole recharge	Open wells and shafts; Aquifer storage and recovery (ASR); Aquifer storage, transfer and recovery (ASTR).	Where impermeable layer lies above the aquifer. Aquifer type: deep and clay covered aquifers.
(h)	Induced bank infiltration	Bank filtration; Dume filtration.	Where close to a surface water body, lowering the water pressure at the lake or river bank, and inducing the water to infiltrate into the aquifer. Aquifer type: Dry rivers with (subsurface) dams/sand dams or at perennial rivers or streams with adjacent permeable sand layers.
(i)	Run off/Rainwater harvesting	Rainwater harvesting; Rainwater recharge from open spaces.	Where runoff can be collected for productive use.

Among these techniques, the type of well, shaft and borehole recharge is one of the most popular applications. Vadose zone wells (VZWs), also known as dry wells or recharge shafts (Figure 1-1e), are boreholes drilled in the vadose zone and then backfilled with highly permeable sands and gravels. VZW injection allows recharge to begin further below ground. It is an important technique to implement MAR in semi-arid and arid regions where the groundwater table is deep or sufficiently permeable soils and/or sufficiently large land areas for surface infiltration are not available (Bouwer, 2002). VZW injection has several advantages over surface infiltration and direct injections wells, including a minimal evaporative loss of water, a small installation area, removal of contaminants in the vadose zone, and a relatively low cost compared with deep well injection (Edwards et al., 2016; Sasidharan et al., 2018). VZW has been widely implemented around the world, including the United States (Bouwer et al., 2008; Jansen et al., 2007; Liu et al., 2016; Lluria, 2009), China (Hao et al., 2014; Wang et al., 2010), Austria (Händel et al., 2016), Finland (Jokela and Kallio, 2015; Sprenger et al., 2017), and Portugal (San-Sebastián-Sauto et al., 2018).

Therefore, the goal of this dissertation is to improve the understanding of VZW injection performance and to obtain more efficient and effective VZW injection management. Three studies are conducted to: 1) investigate the influences of time-dependent GSF generated by infiltration or evapotranspiration on the VZW injection; 2) the control of geometric and soil properties on recharge rate and recharge volume of VZW, and 3) the control of subsurface heterogeneity on recharge rate and recharge volume of VZW. The background and questions motivating the research are summarized in the following sections 1.1-1.3.

1.1 Influence of time-dependent ground surface flux on aquifer recharge with VZW

VZW injection is an important technique to implement MAR in semi-arid and arid regions and it enables recharge to begin further below ground. In these regions, ground surface infiltration, which is often the sole source of water replenishment, and evapotranspiration, as a major source of water depletion, make a great difference on hydrological processes (Liu et al., 2013). Many studies have focused on understanding possible factors that affect the infiltration pattern (Kargas et al., 2012; Wang et al., 2007) and developing improved evapotranspiration estimation models (DehghaniSanij et al., 2004; Weiß and Menzel, 2008). To enhance the efficiency of water management and to obtain more accurate water budget, it is of great importance to investigate the influences of ground surface flux (GSF) generated by infiltration or evapotranspiration on VZW injection.

Hydrological models are effective tools for predicting and understanding hydrological processes, and making a quantitative assessment of the recharge capacity of MAR (Kim et al., 2012; Rahman et al., 2012). Since wells, shafts and boreholes are the most frequently applied methods to recharge an aquifer, most modeling studies were conducted for direct injection into saturated zones (Ringleb et al., 2016). For the VZW injection, Glover (1953) proposed a simple formula to calculate recharge rate of the well by assuming that the groundwater was deep and the downward flow has constant flow rate. Then a lot of groundwater flow models based on the hydraulics of wells were developed (Taneja and Khepar, 1996; Wang et al., 2012). Numerical models for constant-head borehole injection in the unsaturated zone were constructed by Stephens and Neuman (1982) to examine previously derived formulae. Unsaturated flow models coupled with saturated flow models were recently developed and the applications of this type of model has proliferated (Liang et al., 2018; Ringleb et al., 2016). However, the existing VZW injection models usually do not take the influences of GSF generated by infiltration or evapotranspiration into consideration, which can cause some errors to the water budget estimation.

This study focuses on obtaining a better understanding of the influences of GSF generated by infiltration or evapotranspiration on VZW injection to improve the efficiency and feasibility of artificial recharge in semi-arid and arid regions. The derivation of the mathematical model and results are explained in Chapter 2.

1.2 Geometric and soil property control on the recharge of VZW

The prediction of recharge rate and cumulative recharge volume of VZW injection is pivotal for sustainable management of water resources and successful design of VZW. Due to the nonlinear nature of the fluid flow process in the vadose zone, it is still a challenge to accurately predict the recharge of VZW in the field of hydrology (Scanlon et al., 2006; Wang et al., 2016). Some hydrological models have been proposed as effective tools to understand the process of VZW injection and many existing methods for evaluating VZW injection consider ideal scenarios which assume that the aquifer is homogeneous. Liang et al. (2018) solved the linearized Richards' equation based on the Gardner (1958) model and Kroszynski and Dagan (1975) work, and developed a semi-analytical model to investigate hydraulic responses and recharge capacity of VZW with a constant injection rate. Besides, although the VZW method has been applied in many countries, the data from most projects are not publicly available and published field tests on VZW injection are still limited. Jokela and Kallio (2015) performed short duration infiltration tests in VZWs to study the applicability of well infiltration in the neighborhood of the city of Tampere, Finland to provide potable water. Sasidharan et al. (2018) conducted experiments on drywells located at the National Training Center in Fort Irwin, California and a commercial complex in Torrance, California. Their study contributed to improving the knowledge of modern drywell system by developing a numerical model for the Maxwell Type IV drywell and simulating the dynamics of the drywell. A point to note is that the term of VZW used in this study is exchangeable with the term of drywell used in other published studies such as Sasidharan et al. (2018).

With limited experimental data, numerical modeling has become one of the most powerful tools to evaluate the recharge of VZW and it has already been widely used in assessment of many MAR facilities (Ringleb et al., 2016). Groundwater flow models are widely used to examine the influence of hydraulic parameters on the various techniques within MAR (Figure 1-1). Händel et al. (2014) performed numerical simulations in the software HYDRUS (2D/3D) and investigated the impacts of the van Genuchten model parameters and saturated hydraulic conductivity (K_s) on recharge rates of small-diameter wells and surface basins. A point to note is that the small-diameter wells are installed using the direct-push (DP) technology and water is recharged entirely by gravity, so it is very different from either deep aquifer storage and recovery (ASR) wells or shallow

VZWs in which pumps are commonly used to inject pressurized water. Furthermore, the small-diameter wells cannot be used to simulate constant-rate injection scenario (which is the primary concern of this investigation) because of its reliance on gravity only. Händel et al. (2014) found that the recharge rates of small-diameter wells and surface basins had different sensitivity to van Genuchten parameters and K_s, and those parameters affected the downward infiltration area and time of water. Qi et al. (2021) built numerical models of infiltration basin in HYDRUS (2D/3D) to investigate the impacts of vadose zone characteristics such as thickness and lithology. Their results showed that vadose zone factors had various impacts on water distribution and the vadose zone played a significant role during artificial recharge via the infiltration basin. Therefore, the systematic research on soil property control on VZW injection with constant rate is necessary and it can serve as the basis for the research on VZW injection in heterogeneous aquifers, which is more common in field applications than the ideal homogeneous aquifer. Geometric property is another important factor that can greatly impact the recharge of VZW, which is analyzed in this study. In addition, the influences of different injection rate schedules with a given total injection water volume are also investigated in this study. For instance, we address the question: is it better to inject with a larger rate over a relatively short duration, or is it better to inject with a smaller rate over a relatively long duration?

1.3 VZW injection in heterogeneous aquifers

Subsurface heterogeneity can substantially complicate the flow pattern of injected water and increase the difficulty in VZW management. Ringleb et al. (2016) reviewed 216 studies dealing with flow and transport modeling of MAR from 37 countries to evaluate different modeling approaches. Specifically, Ringleb et al. (2016) focused on each MAR method and comprised applications and the choice of modeling software for each technique. For well, shaft and borehole recharge, they found that the aquifer heterogeneity was one of the key parameters that influenced the recovery rate. Most of these studies concerning aquifer heterogeneity in Ringleb et al. (2016) focused on aquifer storage and recovery (ASR) systems in the saturated zone without consideration of the unsaturated zone process (Guo et al., 2015; Vacher et al., 2006).

The research examining the role of subsurface heterogeneity in hydraulic properties on drywell performance in the unsaturated zone is still limited (Sasidharan et al., 2019; Sasidharan et al., 2020). Sasidharan et al. (2019) conducted numerical experiments to systematically study the influence of subsurface heterogeneity on drywell infiltration under constant or falling head conditions and the heterogeneity was described deterministically by defining a high permeable layer/lens or by generating stochastic realizations of soil hydraulic properties. Their direct and indirect numerical experiments demonstrated how to develop field scale falling head and constant head experimental methods for drywells to determine the soil hydraulic properties and to characterize drywell infiltration. Sasidharan et al. (2020) studied the influence of various homogeneous soil types and subsurface heterogeneity on recharge from drywells under constant head conditions by conducting numerical experiments using the HYDRUS (2D/3D) software package. The subsurface heterogeneity was described by generating stochastic realizations of soil hydraulic properties with selected stochastic subsurface heterogeneity parameters and the influence of these parameters on drywell infiltration and recharge were investigated.

A few points are notable after a careful examination of the papers including Sasidharan et al. (2019) and Sasidharan et al. (2020). First, the geometry of drywell used in these studies is quite complex and close to reality, which is an advancement in technique and probably should be considered more often than the conventional vertical wellbore (which is often simplified as a cylinder shape) for future investigations of VZW. Second, although a stochastic method is employed to generate the random subsurface heterogeneity in these two studies, such a random subsurface heterogeneity must be axisymmetric because the simulations conducted in these two studies are all limited to axisymmetric cases only. Axisymmetric random subsurface heterogeneity is rarely seen in real settings, and it is not representative of realistic random subsurface heterogeneity which is three-dimensional (3D) in nature. Therefore, the extension of findings based on such an axisymmetric random subsurface heterogeneity to the realistic 3D subsurface heterogeneity is questionable and not recommended.

Our study simulates the deterministic subsurface heterogeneity in the axisymmetric model. When the geologic records show that the horizontal strata are continuous and have distinctively different hydraulic properties which can be quantified using various hydrological and geophysical methods such as slug tests (Bouwer and

Rice, 1976), multi-level tests with inflatable packers (Holloway and Waddell, 2008), flow meters (Hanson and Nishikawa, 1996), etc., this permits the layered subsurface heterogeneity to be characterized in great detail. Under such conditions, our model can be used to represent the deterministic subsurface heterogeneity.

To date, analysis of the subsurface heterogeneity control on the recharge of VZW injection with constant rate is still lacking. VZW injection with constant rate can be used as a major MAR method in certain areas and can be used to inject large amounts of water. The investigation of the subsurface heterogeneity control on it is essential for efficient design, execution and long-term operation of VZW. Furthermore, the constant rate injection scheme can be used as a reference to study the variable rate injection scheme in a straightforward manner through superposition principle (or convolution computation). This study focuses on improving the knowledge of VZW recharge by conducting numerical experiments to study the influences of subsurface heterogeneity.

CHAPTER 2

INFLUENCE OF TIME-DEPENDENT GROUND SURFACE FLUX ON AQUIFER RECHARGE WITH A VADOSE ZONE INJECTION WELL*

The objective of this study is to advance our understanding of the influences of ground surface flux (GSF) generated by infiltration or evapotranspiration on VZW injection, which can improve the efficiency and feasibility of artificial recharge in semi-arid and arid regions. The mathematical models presented here were derived based on the linearized Richards' equation and the groundwater governing equation to couple the unsaturated and saturated flows during VZW injection. The coupled equations are solved after application of the Laplace and Hankel transformations. The Laplace domain solutions are inversed by the de Hoog algorithm (De Hoog et al., 1982) to obtain the time domain solutions for the hydraulic head and recharge rate. A finite-element numerical simulation is developed with COMSOL Multiphysics (COMSOL Inc., Burlington, MA, USA) to test our solutions. The obtained solutions can help people to get a more accurate water budget estimation and a better evaluation of VZW management.

2.1 The conceptual model

A vadose zone well in the unsaturated-saturated porous media is considered in this study, which is schematically shown in Figure 2-1. The initial water table is

*Reprinted with permission from "Influence of time-dependent ground surface flux on aquifer recharge with a vadose zone injection well" by Qi, C., Zhan, H., Liang, X., & Ma, C., 2020, *Journal of Hydrology*, 584, 1-11, Copyright [2020] by Elsevier B. V.

horizontal and the saturated zone is below the water table with a uniform thickness of *b*. The unsaturated zone lies above the saturated zone and has a uniform thickness of *a*. Both the unsaturated and saturated zones are homogeneous and anisotropic. The bottom of the saturated zone is an impermeable horizontal boundary. At the horizontal top of the unsaturated zone, i.e. ground surface, a time-dependent GSF $I(t)$ is applied. A vadose zone well with a constant recharge rate Q partially penetrates the aquifer and is screened from j to d, where j and d are distances from the top and bottom of the screen to the initial position of water table, respectively. The origin of the cylindrical coordinate system is set at the intercept of the central axis of the well and the water table. The r-axis is oriented horizontally, and the z-axis is oriented vertically where is positive upward. The initial elevation of the water table is z=0.

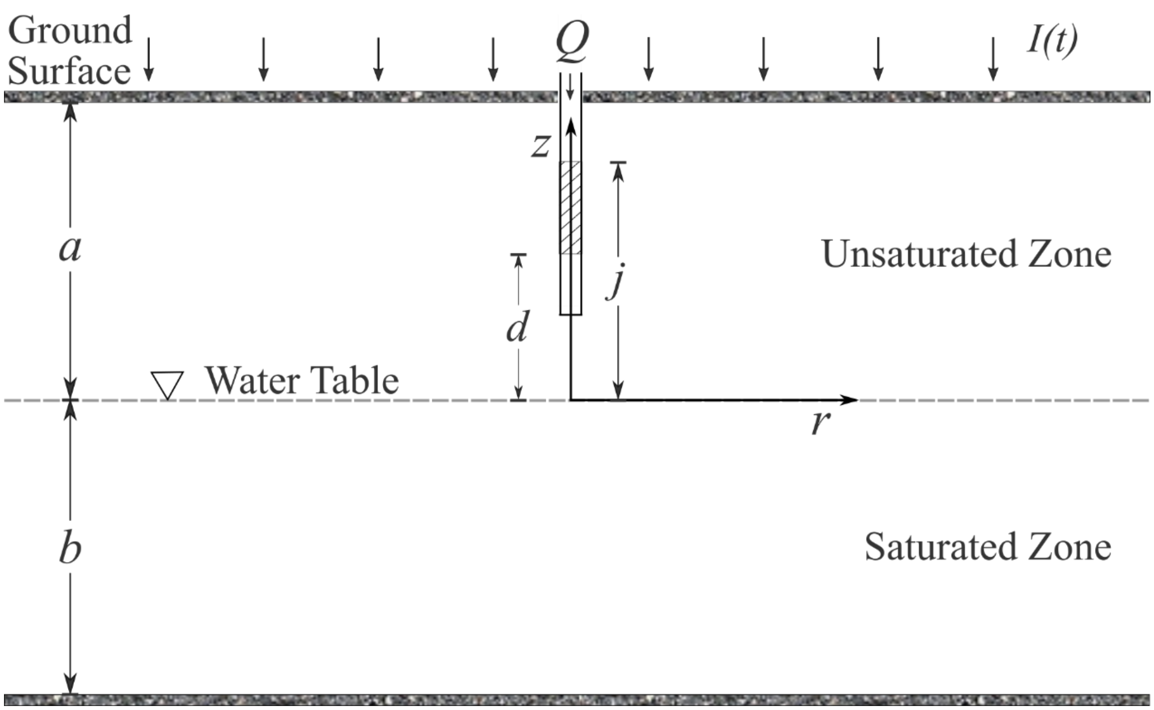

Figure 2-1 The schematic diagram of unsaturated-saturated flow induced by the vadose zone well injection and ground surface flux.

2.2 The mathematical models

Based on the conceptual model described above, the mathematical models for unsaturated and saturated flows induced by VZW injection and GSF were derived. Then the settings of GSF generated by infiltration or evapotranspiration is discussed.

2.2.1 Mathematical models of unsaturated and saturated flow

The flow in the unsaturated zone is governed by Richards' equation. The system described in Figure 2-1 is highly nonlinear because of (1) the nonlinear nature of Richards' equation and (2) the presence of a moving interface (water table) between two different (saturated and unsaturated) flow regimes (Tartakovsky and Neuman, 2007). To solve this problem, Kroszynski and Dagan (1975) employed the method of perturbation expansion to simplify the Richards' equation. The flow is assumed to depart slightly from equilibrium and the dependent variables in Richards' equation can be expanded in perturbation series, whose higher order terms are neglected. Then the remaining terms are substituted into the equation to obtain a first-order linearized equation. This linearization method is widely used in previous studies on coupling unsaturated-saturated flow problems (Chang et al., 2018; Liang et al., 2017b; Lin et al., 2017; Mathias and Butler, 2006; Mishra et al., 2012; Tartakovsky and Neuman, 2007).

The linearized governing equation for the unsaturated zone describing groundwater flow response to the vadose zone injection well and the time-dependent ground surface infiltration is

$$K_r k_0(z) \frac{1}{r} \frac{\partial}{\partial r}\left(r \frac{\partial u}{\partial r}\right) + K_z \frac{\partial}{\partial z}\left(k_0(z) \frac{\partial u}{\partial z}\right) = C_0(z) \frac{\partial u}{\partial t}, \quad 0 \leq z \leq a \tag{2.1}$$

$$u(r, z, 0) = 0 \tag{2.2}$$

$$K_z k_0(z) \frac{\partial u}{\partial z}(r,z,t)\Big|_{z=a} = I(t) \tag{2.3}$$

$$\lim_{r\to\infty} u(r,z,t) = 0 \tag{2.4}$$

$$\lim_{r\to 0} r \frac{\partial u(r,z,t)}{\partial r} = -\frac{Q\Theta(z)}{2\pi K_r (j-d)}, \quad 0 \le z \le a \tag{2.5}$$

$$k_0(z) = k(\theta_0), C_0(z) = C(\theta_0) \tag{2.6}$$

where $u = h_u - h_0$ is the hydraulic head increment in the unsaturated zone or buildup [L], h_0 is the initial hydraulic head [L], and h_u is the hydraulic head in the unsaturated zone [L]; K_r and K_z are the saturated principal hydraulic conductivities in the radial (r) and vertical (z) directions, respectively [LT^{-1}]; Q is the constant injection rate [$\mathrm{L}^3\mathrm{T}^{-1}$]; $\Theta(z)$ is the Box function and is defined as $\Theta(z) = H(z-d) - H(z-j)$ [−], and $H(\cdot)$ is the Heaviside step function ($H(x) = \begin{cases} 0, \text{for } x < 0 \\ 1, \text{for } x \ge 0 \end{cases}$); k_0(z) and C_0(z) are the zero-order approximations of the relative hydraulic conductivity $k(\theta)$ $(0 \le k \le 1)$ [−] and the specific soil moisture capacity $C(\theta) = \mathrm{d}\theta/\mathrm{d}\psi$ (≥ 0) [L^{-1}] at the initial water content of θ_0 [−], respectively; ψ is the pressure head in the unsaturated zone [L]; θ is the volumetric water content [−]; $I(t)$ is the time-dependent GSF generated by infiltration or evapotranspiration [LT^{-1}], and it is positive when water flows vertically downward.

It is noted that in Eq. (2.3) the real boundary condition of the ground surface should be $K_z k_0(z) \frac{\partial u}{\partial z}\Big|_{z=a} = K_z k_0(z) \frac{\partial h_u}{\partial z}\Big|_{z=a} - K_z k_0(z) \frac{\partial h_0}{\partial z}\Big|_{z=a} = I(t)$ since $u = h_u - h_0$. Define $I_u = K_z k_0(z) \frac{\partial h_u}{\partial z}\Big|_{z=a}$ as the total flux on ground surface and $I_0 =$

$K_z k_0(z) \frac{\partial h_0}{\partial z}\Big|_{z=a}$ as the initial ground surface flux. Then $I(t) = I_u - I_0$ describes the change in the time-dependent GSF with respect to that in the natural state. To make sure that the natural state can result in a static hydraulic condition before VZW injection, we make the assumption that $I_0 = 0$.

The key properties of the unsaturated soils are represented by the exponential constitutive relationship (Gardner, 1958), $k = e^{\omega(\psi-\psi_a)}$ and $\theta = \theta_r + S_y e^{\omega(\psi-\psi_a)}$, where θ_r is the residual water content $[-]$; θ_s is the saturated water content $[-]$; ψ_a is the pressure head at which the aquifer starts to desaturate ($\psi \leq \psi_a$); $S_y = \theta_s - \theta_r$ is drainable porosity or the specific yield $[-]$; $\omega > 0$ is a constitutive exponent [L^{-1}], reflecting the ability of the water holding in the unsaturated zone, and its value for most applications may range from 0.2 to 5 m^{-1} (Philip, 1969). According to works of Kroszynski and Dagan (1975), the specific soil moisture capacity follows that $C = \mathrm{d}\theta/\mathrm{d}\psi = S_y e^{\omega(\psi-\psi_a)}$. Then the zero-order approximation functions $k_0(z)$ and $C_0(z)$ are given by

$$k_0(z) = e^{-\omega z} \tag{2.7}$$

$$C_0(z) = S_y \omega e^{-\omega z} \tag{2.8}$$

The governing equation for the saturated zone, which describes the groundwater flow induced by the vadose zone injection, is given by

$$K_r \frac{1}{r}\frac{\partial}{\partial r}\left(r\frac{\partial s}{\partial r}\right) + K_z \frac{\partial^2 s}{\partial z^2} = S_s \frac{\partial s}{\partial t}, \quad -b \leq z \leq 0 \tag{2.9}$$

$$s(r, z, 0) = 0 \tag{2.10}$$

$$\frac{\partial s}{\partial z}(r,z,t)\Big|_{z=-b} = 0 \tag{2.11}$$

$$\lim_{r\to\infty} s(r,z,t) = 0 \tag{2.12}$$

$$\lim_{r\to 0} r\frac{\partial s(r,z,t)}{\partial r} = 0, \quad -b \le z \le 0 \tag{2.13}$$

where $s = h_s - h_0$ is the hydraulic head increment in the saturated zone [L], and h_s is the hydraulic head in the saturated zone [L]; S_s is the specific storage [L^{-1}].

At the water table, the unsaturated and saturated flows are coupled by interface conditions representing continuity of pressure and normal flux across the water table (Tartakovsky and Neuman, 2007). The linearized interface conditions at the water table are denoted as

$$s - u = 0, \quad z = 0 \tag{2.14}$$

$$\frac{\partial s}{\partial z} - \frac{\partial u}{\partial z} = 0, \quad z = 0 \tag{2.15}$$

2.2.2 The setting of GSF generated by infiltration or evapotranspiration

The time-dependent ground surface flux can be generated by the ground surface infiltration and evapotranspiration processes. However, those processes are complex and always dependent on the saturation of near-surface soils (Beven, 1979; Chu, 1978; Patil et al., 2019). To simplify the model and focus on their influences on flow induced by VZW injection, $I(t)$ is defined as a known time-dependent ground surface flux generated by infiltration or evapotranspiration. The sign of $I(t)$ value (positive and negative) represents its direction, and a positive value of $I(t)$ means that its direction is vertically downward.

For the demonstration purpose, the GSF $I(t)$ is considered as a piecewise function with time in this study

$$I(t) = I_i, \quad t \in [t_{i-1}, t_i), \quad i = 1, 2, 3, \ldots \tag{2.16}$$

where I_i is constant for the time interval $[t_{i-1}, t_i)$ and $t_0 = 0$.

In field cases, GSF generated by surface infiltration or evapotranspiration can be expressed as complex functions with several parameters (DehghaniSanij et al., 2004; Weiß and Menzel, 2008). The simplification of GSF $I(t)$ as a constant value during a certain time interval is not unreasonable. The actual $I(t)$ can be discretized over many small time intervals, and the discretized part on any small time interval can be approximated by a simple function like what are used in this study. Once the impact of GSF for each small time interval can be obtained, the overall GSF impact can be straightforwardly obtained using the principle of superposition because of the linear nature of the initial and boundary conditions involved in this study. Therefore, although this study uses one piecewise function of GSF for the demonstration purpose, the procedure can be directly extended to a sequence of rather arbitrary piecewise functions to mimic an actual time-dependent GSF function $I(t)$.

2.3 Solutions

The dimensionless variables are defined as follows:

$$s_D = \frac{2\pi K_r a s}{Q},\ u_D = \frac{2\pi K_r a u}{Q},\ r_D = \frac{r}{a},\ z_D = \frac{z}{a},\ b_D = \frac{b}{a},\ t_D = \frac{K_r}{S_s a^2} t,$$

$$K_D = \frac{K_z}{K_r},\ l_D = \frac{l}{a},\ d_D = \frac{d}{a},\ \omega_D = \omega a,\ \beta = \omega_D b_D S_{yD},\ S_{yD} = \frac{S_y}{S},$$

$$S = S_s b,\ \gamma = K_D \omega_D\ I_D = \frac{2\pi a^2}{Q} I(t),\ \xi = K_D e^{-\omega_D} \tag{2.17}$$

where the subscript *'D'* represents a dimensionless term hereinafter. Substituting these dimensionless variables into Eqs. (2.1) – (2.15), one obtains the dimensionless forms of the governing equations for the unsaturated zone,

$$\frac{1}{r_D}\frac{\partial}{\partial r_D}\left(r_D \frac{\partial u_D}{\partial r_D}\right) + K_D \frac{\partial^2 u_D}{\partial z_D{}^2} - \gamma \frac{\partial u_D}{\partial z_D} = \beta \frac{\partial u_D}{\partial t_D}\ , \quad 0 \le z_D \le 1 \tag{2.18}$$

$$u_D(r_D, z_D, 0) = 0 \tag{2.19}$$

$$\xi \frac{\partial u_D}{\partial z_D}(r_D, z_D, t_D)\Big|_{z_D=1} = I_D(t_D) \tag{2.20}$$

$$\lim_{r_D \to \infty} u_D(r_D, z_D, t_D) = 0 \tag{2.21}$$

$$\lim_{r_D \to 0} r_D \frac{\partial u_D(r_D, z_D, t_D)}{\partial r_D} = -\frac{\Theta(z_D)}{j_D - d_D}, \quad 0 \le z_D \le 1 \tag{2.22}$$

and for the saturated zone,

$$\frac{1}{r_D}\frac{\partial}{\partial r_D}\left(r_D \frac{\partial s_D}{\partial r_D}\right) + K_D \frac{\partial^2 s_D}{\partial z_D{}^2} = \frac{\partial s_D}{\partial t_D}, \quad -b_D \le z_D < 0 \tag{2.23}$$

$$s_D(r_D, z_D, 0) = 0 \tag{2.24}$$

$$\frac{\partial s_D}{\partial z_D}(r_D, z_D, t_D)\Big|_{z_D=-b_D} = 0 \tag{2.25}$$

$$\lim_{r_D \to \infty} s_D(r_D, z_D, t_D) = 0 \tag{2.26}$$

$$\lim_{r_D \to 0} r_D \frac{\partial s_D(r_D, z_D, t_D)}{\partial r_D} = 0\,, \quad -b_D \le z_D < 0 \tag{2.27}$$

For the interface between the unsaturated and saturated zones, one has

$$s_D - u_D = 0, \quad z_D = 0 \tag{2.28}$$

$$\frac{\partial s_D}{\partial z_D} - \frac{\partial u_D}{\partial z_D} = 0, \quad z_D = 0 \tag{2.29}$$

Eqs. (2.18) – (2.29) are solved through sequential application of the Laplace transformation and Hankel transformation. The details of derivation are presented in Supplementary Material of Qi et al. (2020).

The Laplace domain solution of hydraulic head increments in the unsaturated zone is

$$\bar{u}_D(r_D, z_D, p) = \int_0^\infty [Ae^{Mz_D} + Be^{Nz_D} + \Theta(z_D)Y]\alpha J_0(\alpha r_D)d\alpha \tag{2.30}$$

where

$$A = A_1 + B_1 \tag{2.31}$$

$$B = A_2 + B_2 \tag{2.32}$$

$$A_1(\mathrm{z}_D) = \frac{\left(e^{-Nl_\mathrm{D}} - e^{-Nd_D} + e^{-\Delta H(d_D - z_D) - Md_D} - e^{-\Delta H(l_D - z_D) - Ml_D}\right)NY}{(e^{-\Delta} - 1)\Delta} \tag{2.33}$$

$$A_2(\mathrm{z}_D) = \frac{\left(e^{-\Delta - Ml_D} - e^{-\Delta - M\mathrm{d}_D} + e^{-\Delta H(z_D - d_D) - Nd_D} - e^{-\Delta H(z_D - l_D) - Nl_D}\right)MY}{(e^{-\Delta} - 1)\Delta} \tag{2.34}$$

$$B_1 = -\frac{U_{10}\eta\left(\frac{N}{M}\right) + \left[\frac{\eta}{M} - \coth(\eta b_D)\right]\frac{N}{M} \cdot R}{Ncoth(\eta b_D) \cdot (e^{-\Delta} - 1) - \eta\left(e^{-\Delta} - \frac{N}{M}\right)} + \frac{R}{M} \tag{2.35}$$

$$B_2 = \frac{U_{10}\eta e^{-\Delta} + \left[\frac{\eta}{M} - \coth(\eta b_D)\right]e^{-\Delta} \cdot R}{Ncoth(\eta b_D) \cdot (e^{-\Delta} - 1) - \eta\left(e^{-\Delta} - \frac{N}{M}\right)} \tag{2.36}$$

the overbar represents a variable in the Laplace domain hereinafter; p is the Laplace transform parameter with respect to the dimensionless time; $J_0(\cdot)$ is the zero-order Bessel function of the first kind; α is the parameter of Hankel transformation, the definition of $M, N, \Delta, \eta, Y, U_{10}$ and R can be found in Supplementary Material of Qi et al. (2020).

The Laplace domain solution of hydraulic head increment for the saturated zone s_D is

$$\bar{s}_D = \int_0^{\infty} \left(F + \frac{R}{\eta}\right) \sin(\eta z_D) \left[1 + \coth(\eta b_D) \coth(\eta z_D)\right] \alpha J_0(\alpha r_D) d\alpha \tag{2.37}$$

where

$$F = \frac{Y\left(e^{-N l_D} - e^{-N d_D} + e^{-\Delta - M d_D} - e^{-\Delta - M l_D}\right) + \left[\frac{1}{M} - \frac{1}{\eta}\coth(\eta b_D)\right](e^{-\Delta} - 1) \cdot R}{coth(\eta b_D) \cdot (e^{-\Delta} - 1) - \eta\left(\frac{e^{-\Delta}}{N} - \frac{1}{M}\right)} \tag{2.38}$$

The dimensionless recharge rate from the unsaturated zone to the saturated zone is obtained by

$$\bar{q}_D(p) = K_D \frac{d\bar{s}_D}{dz_D}|_{z_D=0} = \left[\frac{K_D \eta Y\left(e^{-N l_D} - e^{-N d_D} + e^{-\Delta - M d_D} - e^{-\Delta - M l_D}\right)}{coth(\eta b_D) \cdot (e^{-\Delta} - 1) - \eta\left(\frac{e^{-\Delta}}{N} - \frac{1}{M}\right)} + R_1 + R_2\right]_{\alpha=0} \tag{2.39}$$

where

$$R_1 = \frac{\left[\frac{\eta}{M} - coth(\eta b_D)\right](e^{-\Delta} - 1) \cdot e^{-M} e^{\kappa_D} \bar{I}_D(p)}{coth(\eta b_D) \cdot (e^{-\Delta} - 1) - \eta\left(\frac{e^{-\Delta}}{N} - \frac{1}{M}\right)} \tag{2.40}$$

$$R_2 = e^{-M} e^{\kappa_D} \bar{I}_D(p) \tag{2.41}$$

$\bar{q}_D$ is the Laplace transform of q_D, and $q_D = \frac{2\pi a^2}{Q} q$; $q = K_z \frac{ds}{dz}\Big|_{z=0}$ is the infiltration rate at the interface of the unsaturated and saturated zones $[L^3 T^{-1}]$.

This study evaluates the integration of the inverse Hankel transformation in Eqs. (2.30) – (2.41) by a numerical method proposed by Ogata (2005). Ogata (2005) discussed a numerical integration formula which solves an infinite integral involving the Bessel function by the quadrature formula with the zeros of the Bessel functions as nodes for the integrals. This numerical method is convenient to implement and has a high accuracy (Liang et al., 2018).

Note that Eqs. (2.30) – (2.41) are Laplace domain solutions, which are sufficiently complex to defy analytical inversion to obtain the time domain solutions. Therefore, the de Hoog algorithm (De Hoog et al., 1982) is adopted to numerically invert the Laplace domain solutions into the time domain solutions.

The solutions of Eqs. (2.30) – (2.41) are tested by comparison with a finite-element numerical model constructed within COMSOL Multiphysics. The axisymmetric model simulates the flow in the unsaturated-saturated zone induced by a vertical VZW and GSF. The dimensionless parameter values are set as follows. The initial saturated zone thickness b_D is 1.0, the hydraulic conductivity anisotropy K_D is 1.0, the constitutive exponent ω_D is 1×10^{-2}, and the specific yield S_{yD} is 1×10^{3}. The screen top and bottom of the injection well are respectively $j_D = 0.7$ and $d_D = 0.3$. We assume that the GSF occurs during $t_D \in [10^{-2}, 50)$ with a constant rate of $I_D = 0.5$. The dimensionless governing equations are solved by the partial differential equation solver of COMSOL. This model is discretized by 36495 triangular elements. To improve accuracy, elements near the injection well, the ground surface, and the interface between the unsaturated and saturated zones are refined with the minimum element size of 0.001 and a growth rate of 1.1. The total simulation time $t_D = 1 \times 10^{3}$ and the time step grows exponentially, starting at $\Delta t_D = 1 \times 10^{-2}$.

Figure 2-2 demonstrates the comparison in which the present solution results are represented by solid curves and the numerical simulation results are represented by circle symbols. Figure 2-2a shows the dimensionless time t_D vs. the dimensionless hydraulic head increments u_D or s_D in the saturated zone ($z_D = -0.1$) and the unsaturated zone ($z_D = 0.1, 0.5,$ and 0.9) at $r_D = 0.1$. For the same z_D, the u_D and s_D values obtained by these two methods agree with each other well. Figure 2-2b shows the dimensionless hydraulic head increments u_D or s_D vs. z_D at $t_D = 0.1, 1, 10$ and 100. For the same t_D, the u_D and s_D values obtained by these two methods have very small differences which can be ignored. The comparison above indicates that our solution has sufficient accuracy to predict the hydraulic head changes induced by the VZW injection and GSF.

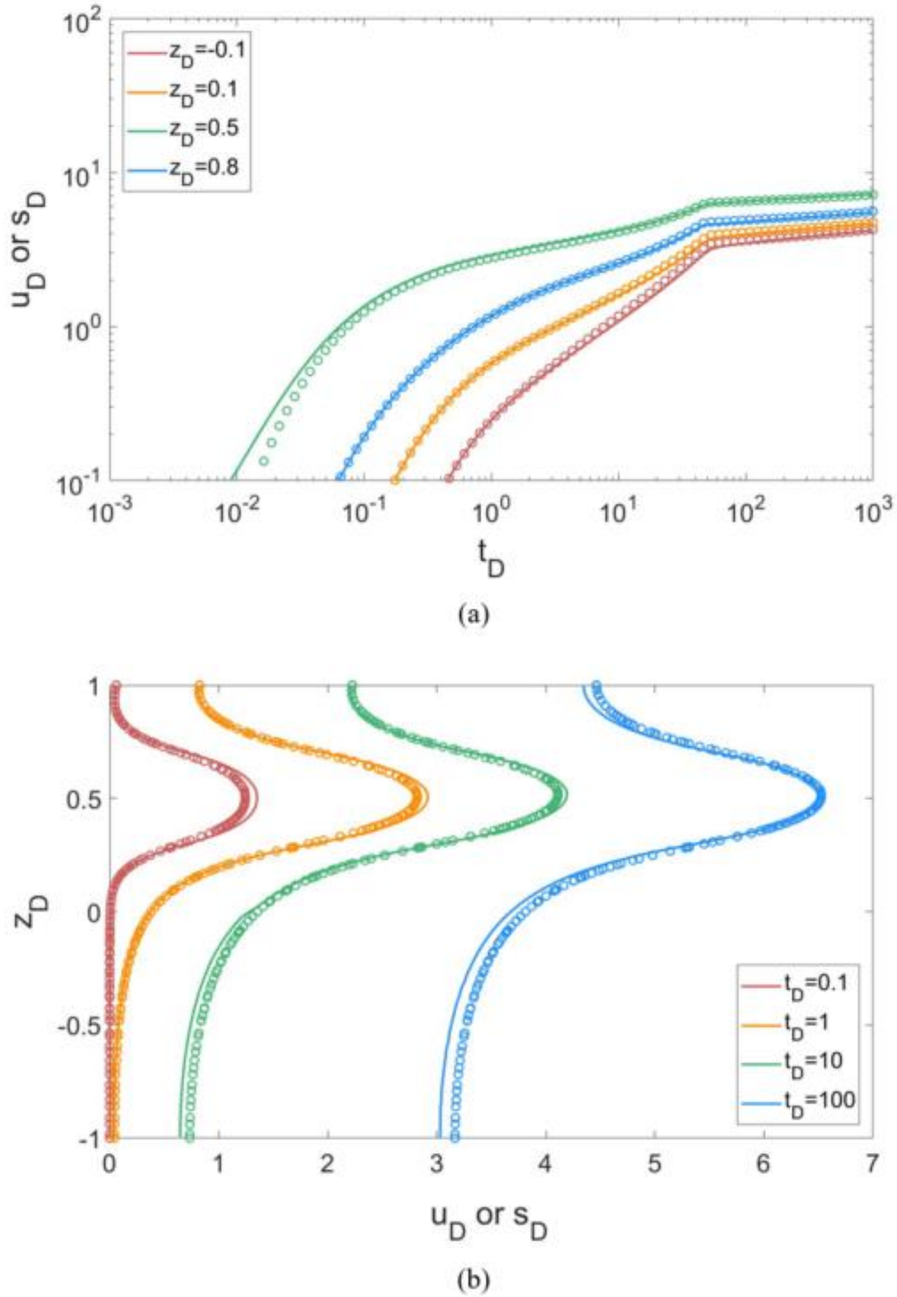

Figure 2-2 Comparison of the present solution (solid curves) with numerical solution (circle symbols).

2.4 Results

2.4.1 Influences of GSF generated by surface infiltration

The response pattern of the hydraulic heads in the unsaturated and saturated zones induced by VZW injection is affected by GSF as well as properties of unsaturated and saturated zones, such as constitutive exponent of the unsaturated zone, specific yield of the unsaturated zone, and the anisotropy of the unsaturated and saturated zone. To get better understanding of influences of GSF, the impacts of unsaturated and saturated aquifer properties have to be taken into consideration and relative analyses are adopted. Other parameter values of the well and unsaturated and saturated zones are the same as that in Section 2.3.

We first investigate how the hydraulic heads change with the GSF generated by infiltration for the dimensionless constitutive exponent $\omega_D = 1 \times 10^{-4}, 1 \times 10^{-3}, 1 \times 10^{-2}$ and 1×10^{-1}, where $S_{yD} = 1 \times 10^3$ and $K_D = 1$. Figure 2-3 shows changes of u_D and s_D with $I_D = 1$ during $t_D \in [10^{-2}, 50)$ (solid curves) and without I_D (dotted curves). In Figure 2-3a, the hydraulic head increment u_D increases with time and the presence of GSF I_D enhances this increase. After $t_D = 50$ when I_D stops, u_D gradually stops increasing and reaches a constant value. The value of ω_D has a significant effect on the influence of I_D on u_D. A smaller ω_D leads to stronger influences of I_D on u_D. A small ω_D means that the storage capacity and/or thickness of the unsaturated zone are small, resulting in relatively large hydraulic head changes induced by the VZW injection and GSF. In addition, more water can be drained downward into the saturated zone, giving rise to larger s_D. Figure 2-3b displays that the changes of s_D with t_D and the influences of I_D on s_D are similar to the curves of u_D in Figure 2-3a.

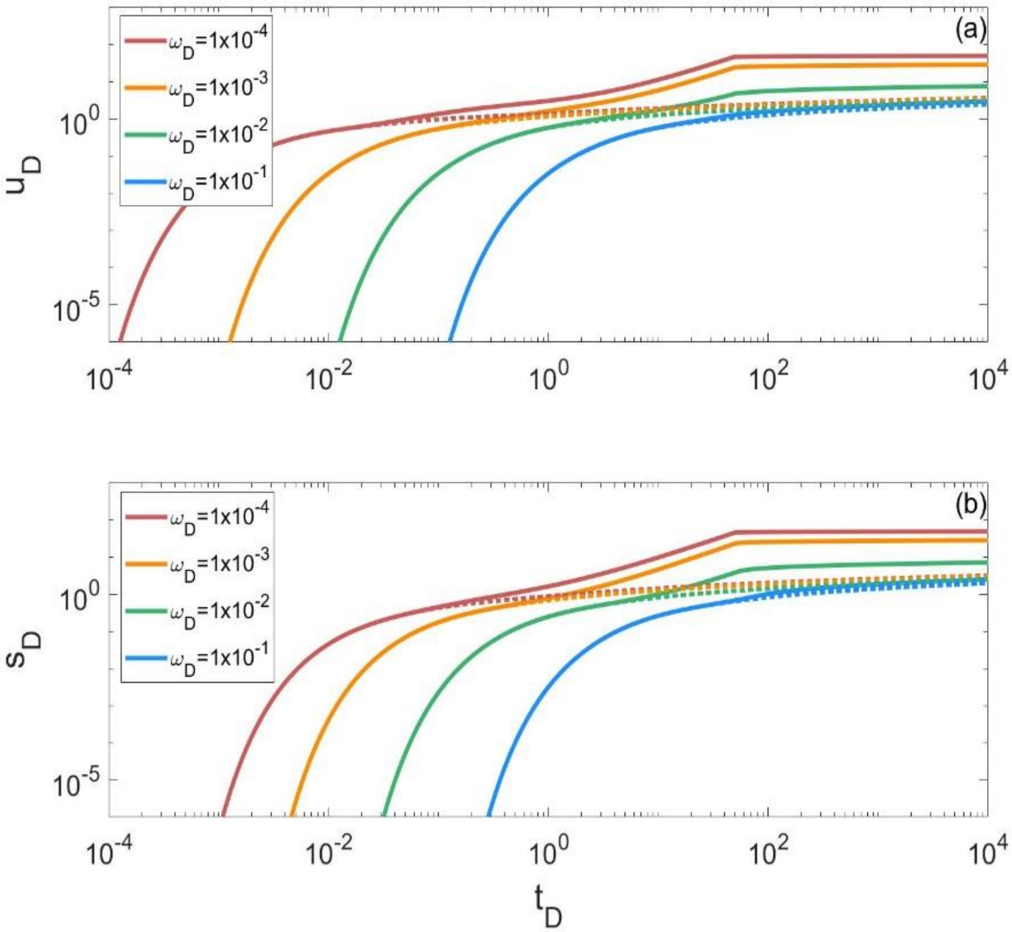

Figure 2-3 The dimensionless time t_D vs. the dimensionless hydraulic head increments u_D and s_D with I_D = 1 during $t_D \in [10^{-2}, 50]$ (solid curves) and without I_D (dotted curves): (a) t_D vs. u_D for different values of the dimensionless unsaturated constitutive exponent ω_D, where r_D = 0.1, z_D = 0.1, $S_{yD} = 1\times10^3$ and K_D = 1; (b) t_D vs. s_D for different values of ω_D, where r_D = 0.1, z_D = -0.1, $S_{yD} = 1\times10^3$ and K_D = 1.

Figure 2-4 shows the hydraulic heads change with the dimensionless GSF generated by infiltration $I_D = 1$ during $t_D \in [10^{-2}, 50)$ (solid curves) and without I_D (dotted curves) for the dimensionless specific yield $S_{yD} = 1 \times 10^2, 1 \times 10^3, 1 \times$

10^4 and 1×10^5, where $\omega_D = 1 \times 10^{-2}$ and $K_D = 1$. In Figure 2-4, the presence of I_D enlarges u_D and s_D, and the influence of I_D is decreased as S_{yD} increases. The dimensionless specific yield S_{yD} represents the storage capacity of the unsaturated zone. A larger S_{yD} means that more water can be stored in the unsaturated zone, reducing the influences of I_D and hydraulic head changes in the unsaturated and saturated zones.

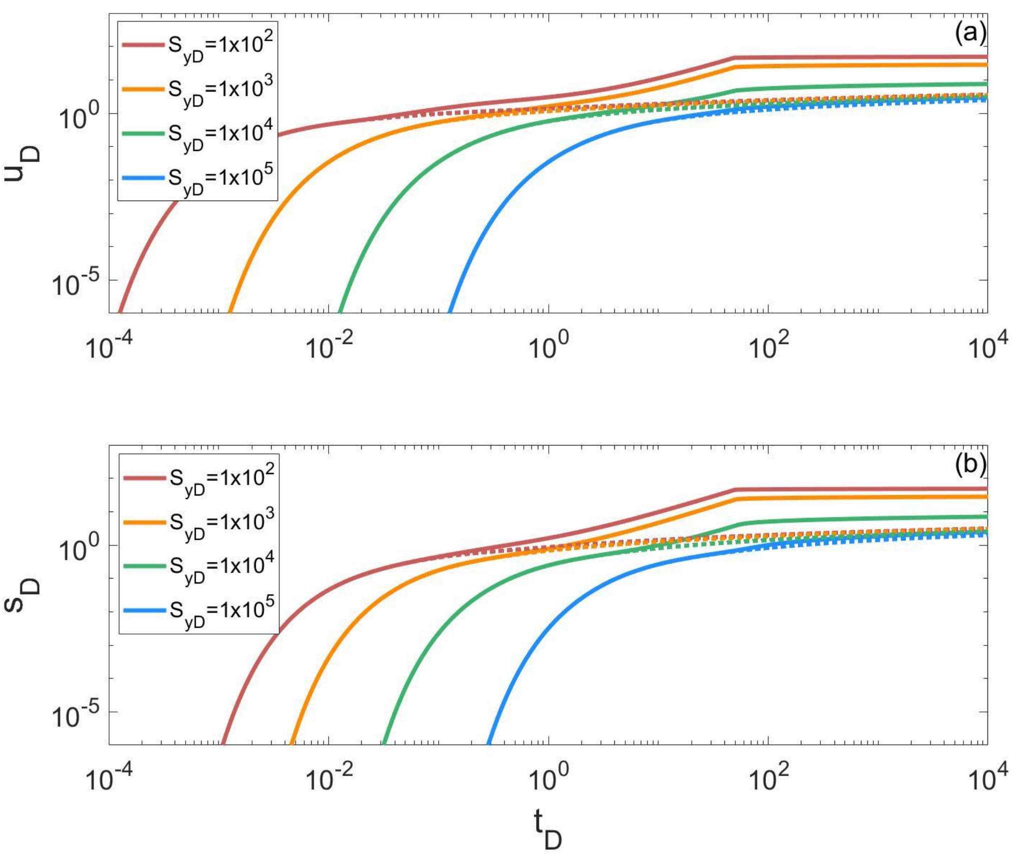

Figure 2-4 The dimensionless time t_D vs. the dimensionless hydraulic head increments u_D and s_D with I_D = 1 during $t_D \in [10^{-2}, 50]$ (solid curves) and without I_D (dotted curves): (a) t_D vs. u_D for different values of the dimensionless specific yield S_{yD}, where r_D = 0.1, z_D = 0.1, $\omega_D = 1\times10^{-2}$ and K_D = 1; (b) t_D vs. s_D for different values of the dimensionless specific yield S_{yD}, where r_D = 0.1, z_D = -0.1, $\omega_D = 1\times10^{-2}$ and K_D = 1.

Figure 2-5 displays the hydraulic head changes with the dimensionless GSF generated by infiltration $I_D = 1$ during $t_D \in [10^{-2}, 50)$ (solid curves) and without I_D (dotted curves) for the hydraulic conductivity anisotropy $K_D = 0.01, 0.1, 1, 10$, where $\omega_D = 1 \times 10^{-2}$ and $S_{yD} = 1 \times 10^3$. In Figure 2-5a, the presence of GSF I_D enlarges u_D and this influence is delayed further as K_D decreases. The reason is that a smaller K_D indicates that the horizontal flow is dominant in the unsaturated zone at early stage. After this early stage, the flow will move downward into the saturated zone, causing an obvious delay of s_D increment shown in Figure 2-5b.

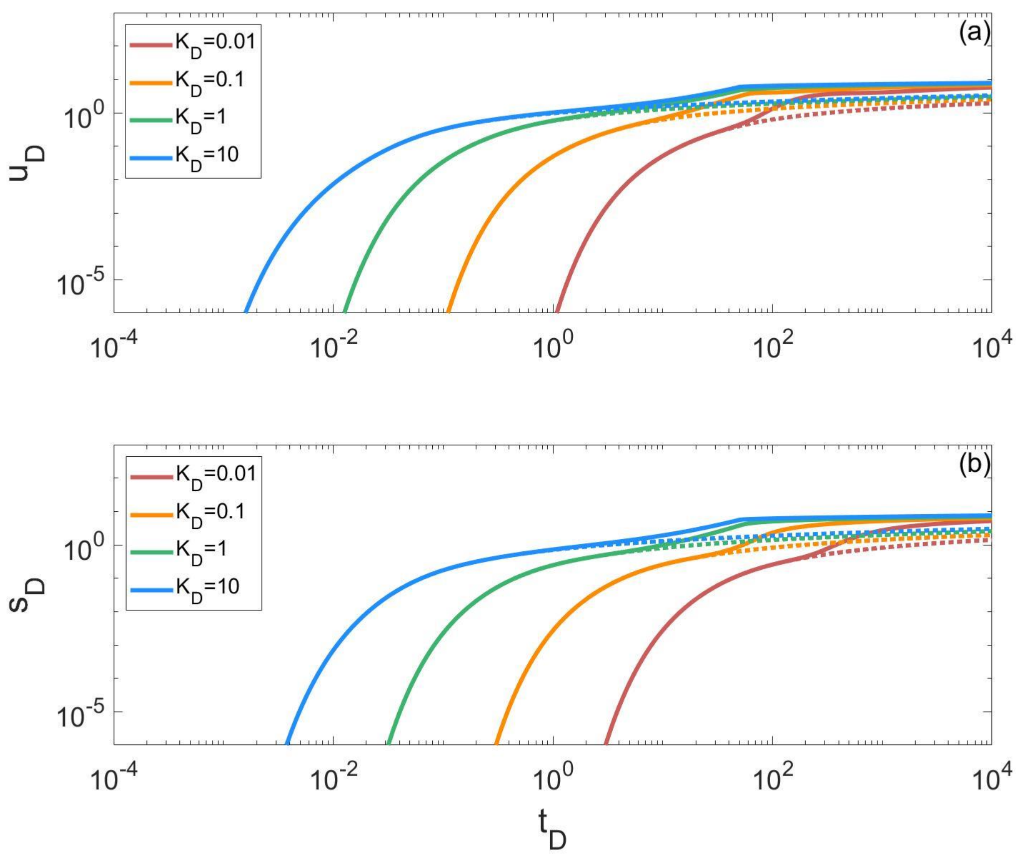

Figure 2-5 The dimensionless time t_D vs. the dimensionless hydraulic head increments u_D and s_D with $I_D = 1$ during $t_D \in [10^{-2}, 50]$ (solid curves) and without I_D (dotted curves): (a) t_D vs. u_D for different values of the hydraulic conductivity anisotropy K_D,

where r_D = 0.1, z_D = 0.1, ω_D = 1×10^{-2}, and S_{yD} = 1×10^3; (b) t_D vs. s_D for different values of the hydraulic conductivity anisotropy K_D, where r_D = 0.1, z_D = -0.1, ω_D = 1×10^{-2}, and S_{yD} = 1×10^3.

Figure 2-6 presents the hydraulic head changes with different dimensionless GSF generated by infiltration $I_D = 0, 0.5, 1,$ and 2, where $\omega_D = 1 \times 10^{-2}$, $S_{yD} = 1 \times 10^3$, and $K_D = 1$. In Figure 2-6(1), I_D is applied during $t_D \in [10^{-2}, 50)$. u_D increases as I_D increases. A larger I_D means more water can infiltrate into the unsaturated zone, leading to faster increase of u_D. Then the water enters the saturated zone, enlarging s_D. In Figure 2-6(2), I_D is applied during a later time $t_D \in [200, 250)$. After a relatively long period of VZW injection, the GSF is applied, which causes gradual increases of u_D and s_D. Then u_D and s_D will reach to constant values after I_D stops.

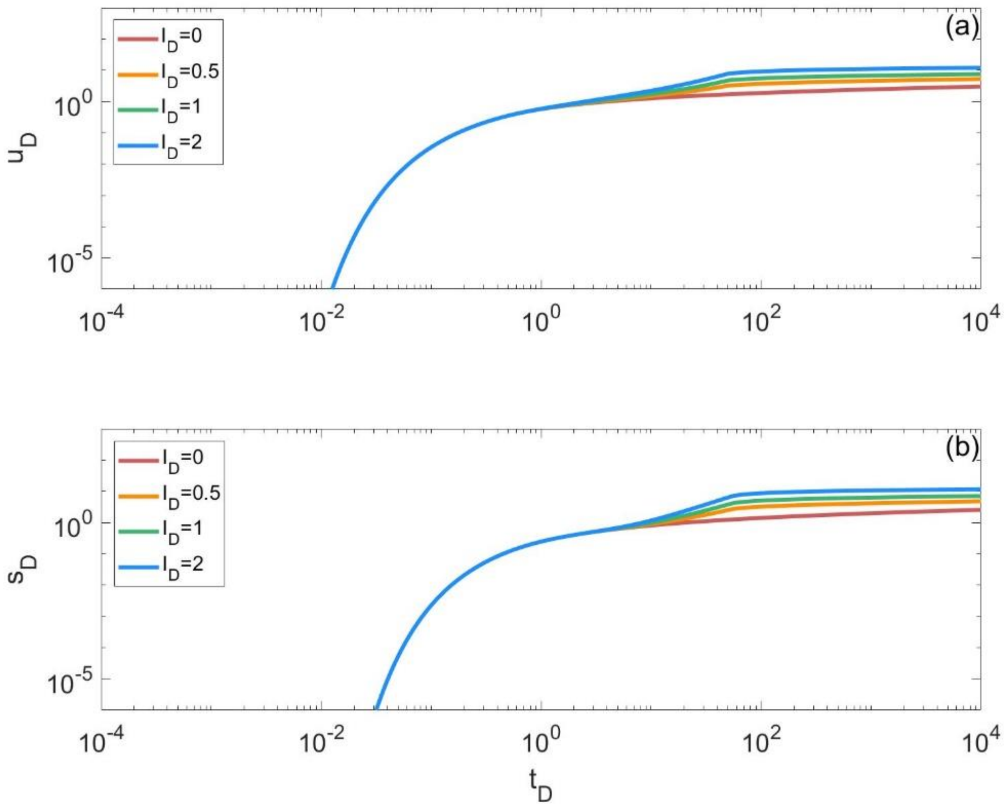

(a)
l_D=0
l_D=0.5
l_D=1
l_D=2
u_D
10^0
10^{-5}
10^{-4}
10^{-2}
10^0
10^2
10^4
(b)
l_D=0
l_D=0.5
l_D=1
l_D=2
s_D
10^0
10^{-5}
10^{-4}
10^{-2}
10^0
10^2
10^4
t_D

(1)

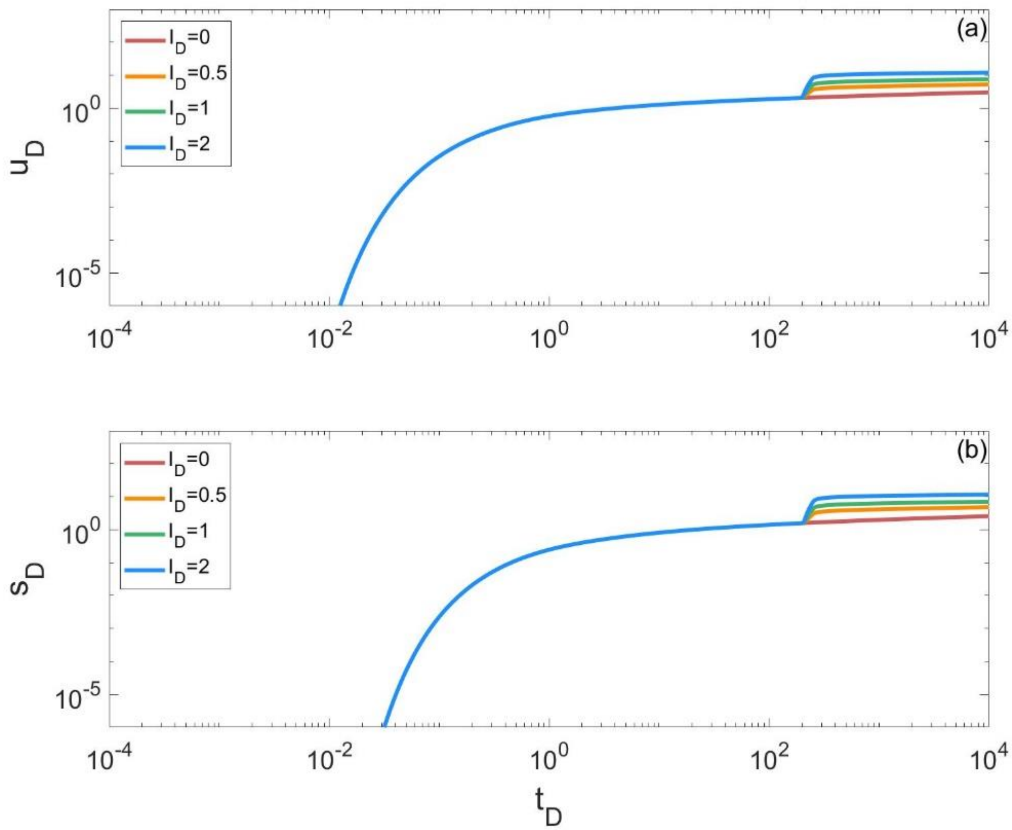

(2)

Figure 2-6 The dimensionless time t_D vs. the dimensionless hydraulic head increments for different values of the dimensionless GSF I_D generated by infiltration, where r_D = 0.1, $\omega_D = 1\times10^{-2}$, $S_{yD} = 1\times10^3$, and K_D = 1: (1) I_D is applied during $t_D \in [10^{-2}, 50]$: (a) t_D vs. u_D (z_D = 0.1); (b) t_D vs. s_D (z_D = -0.1). (2) I_D is applied during $t_D \in [200, 250]$: (a) t_D vs. u_D (z_D = 0.1); (b) t_D vs. s_D (z_D = -0.1).

Figure 2-7 demonstrates that the dimensionless infiltration rate at the interface of the unsaturated and saturated zones changes with different dimensionless GSF generated by infiltration $I_D = 0, 0.5, 1,$ and 2 during $t_D \in [10^{-2}, 50)$ where $\omega_D = 1 \times 10^{-2}$, $S_{yD} = 1 \times 10^3$, and $K_D = 1$. For $I_D = 0$, q_D increases as t_D increases at the early stage and then reaches a constant value. The presence of I_D increases q_D and a larger I_D induces a larger q_D. The figure at the lower right corner of Figure 2-7 zooms in the curves of $t_D \in [45, 55)$. It shows that after $t_D = 50$ when I_D stops, q_D gradually decreases to a constant value, which is not influenced by the value of I_D. The reason is that I_D increases the water into the unsaturated zone as well as the saturated zone, giving rise to higher q_D. When I_D stops, this influence also stops.

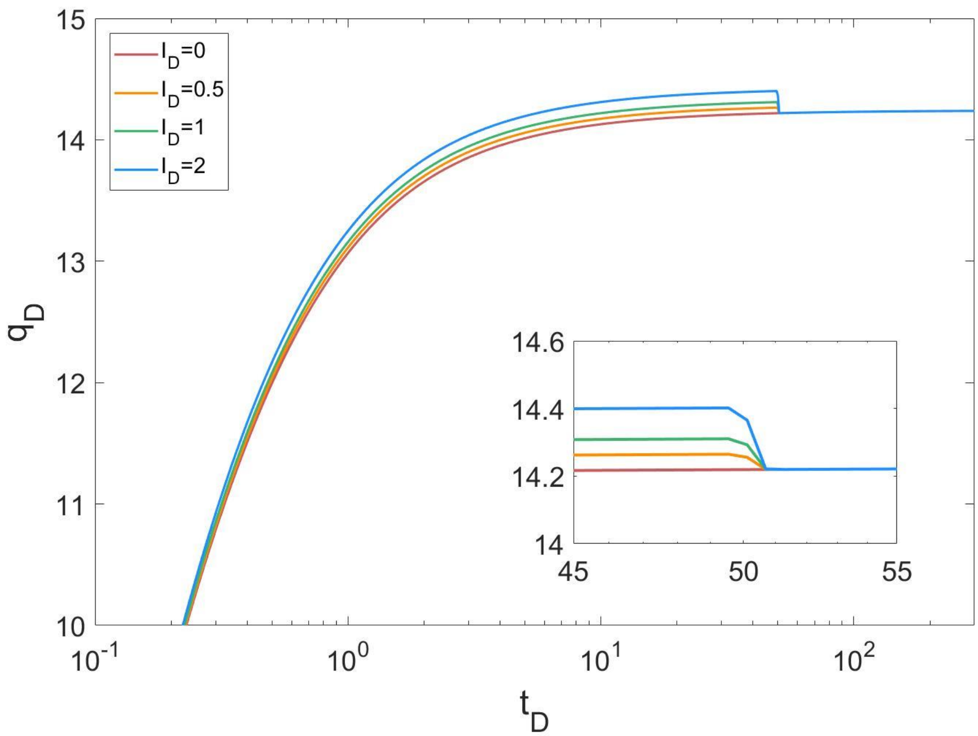

Figure 2-7 The dimensionless time t_D vs. the dimensionless infiltration rate at the interface of the unsaturated and saturated zones q_D for different values of the dimensionless GSF I_D generated by infiltration, where $r_D = 0.1$, $\omega_D = 1\times10^{-2}$, $S_{yD} = 1\times10^{3}$, and $K_D = 1$.

To examine the influence of GSF after the steady state flow is somewhat established by the VZW injection, Figure 2-8 displays the profile contours of u_D ($z_D > 0$) and s_D ($z_D < 0$) with different GSF I_D applied during $t_D \in [200, 250)$, where $\omega_D = 1 \times 10^{-2}$, $S_{yD} = 1 \times 10^{3}$, and $K_D = 1$. In Figure 2-8(1), when $I_D = 0$, the influence area of VZW injection increases as time increases. In Figure 2-8(2), $I_D = 0.5$ is applied during $t_D \in [200, 250)$. Before I_D starts, the changes of u_D and s_D are the same with that in Figure 2-8(1)a. The presence of I_D enlarges the influence area, especially at the top of the unsaturated zone. After I_D stops, u_D and s_D gradually reach to constant values, which are larger than that in Figure 2-8(1)c. In Figure 2-8(3), $I_D = 1$ is applied during $t_D \in [200, 250)$. The change tendency of u_D and s_D is the same with that in Figure 2-8(2), while the values of u_D and s_D are larger than those at the same time in Figure 2-8(2).

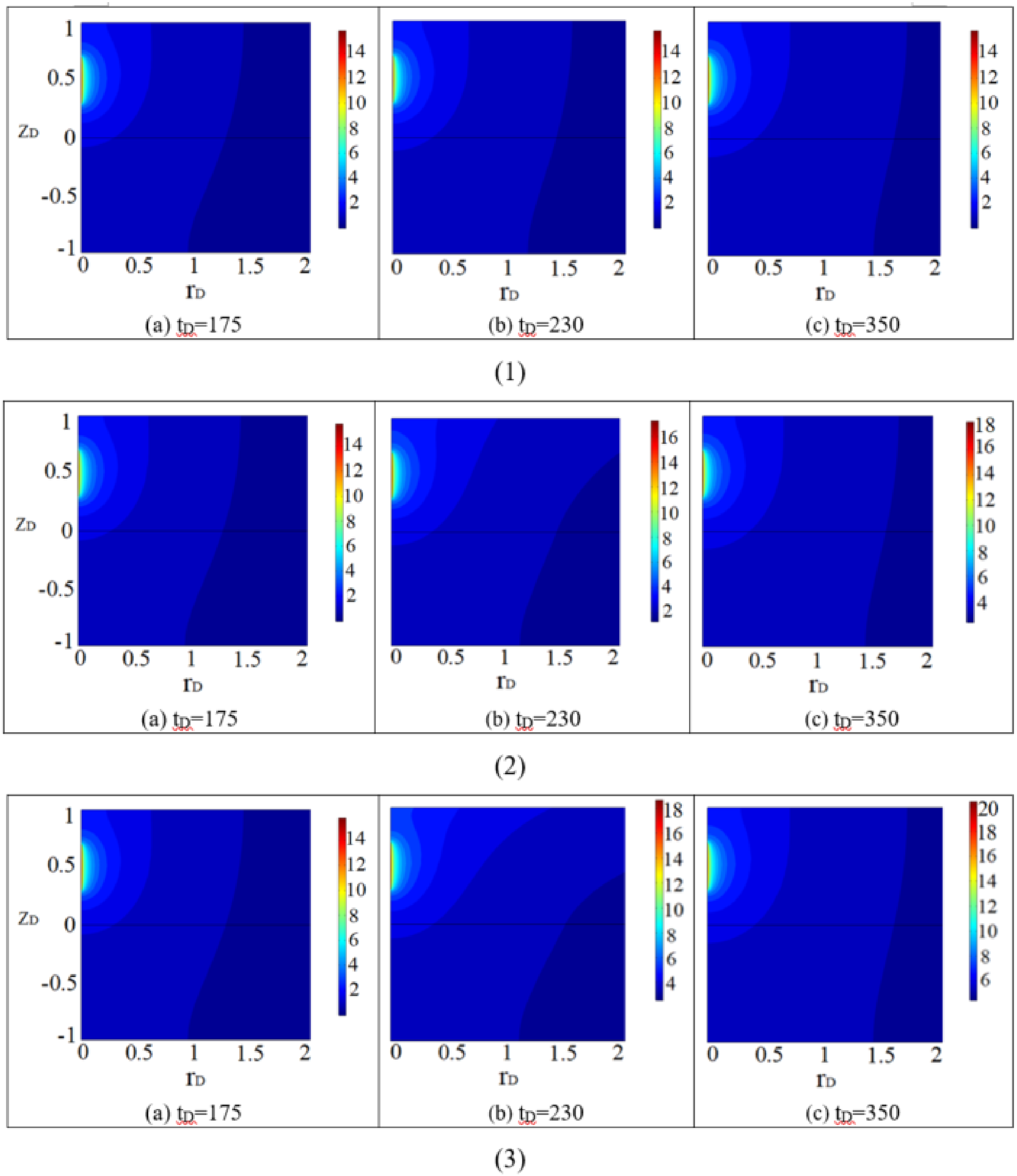

Figure 2-8 The profile contours of u_D ($z_D > 0$) and s_D ($z_D < 0$) with different GSF I_D applied during $t_D \in [200, 250]$, where $\omega_D = 1\times10^{-2}$, $S_{yD} = 1\times10^{3}$, and $K_D = 1$: (1) the profile contours with $I_D = 0$ at (a) $t_D = 175$, (b) $t_D = 230$, and (c) $t_D = 350$; (2) the profile contours with $I_D = 0.5$ at (a) $t_D = 175$, (b) $t_D = 230$, and (c) $t_D = 350$; and (3) the profile contours with $I_D = 1$ at (a) $t_D = 175$, (b) $t_D = 230$, and (c) $t_D = 350$.

2.4.2 Influences of GSF generated by evapotranspiration

Figure 2-9 shows the hydraulic head increments change with the dimensionless GSF generated by evapotranspiration $I_D = -0.3$ during $t_D \in [10^{-2}, 50)$ (solid curves) and without I_D (dotted curves) for the dimensionless constitutive exponent $\omega_D = 5 \times 10^{-3}, 8 \times 10^{-3}, 1 \times 10^{-2}$ and 1×10^{-1}, where $S_{yD} = 1 \times 10^3$ and $K_D = 1$. In Figure 2-9, the presence of I_D decreases u_D and s_D and a smaller ω_D leads to smaller u_D and s_D. ω_D represents the storage capacity and/or thickness of the unsaturated zone. A smaller ω_D means that more water can be evaporated through the ground surface and less water drains downward into the saturated zone, resulting in smaller u_D and s_D. When ω_D is very small, u_D and s_D may become negative for some time and then increases after I_D stops.

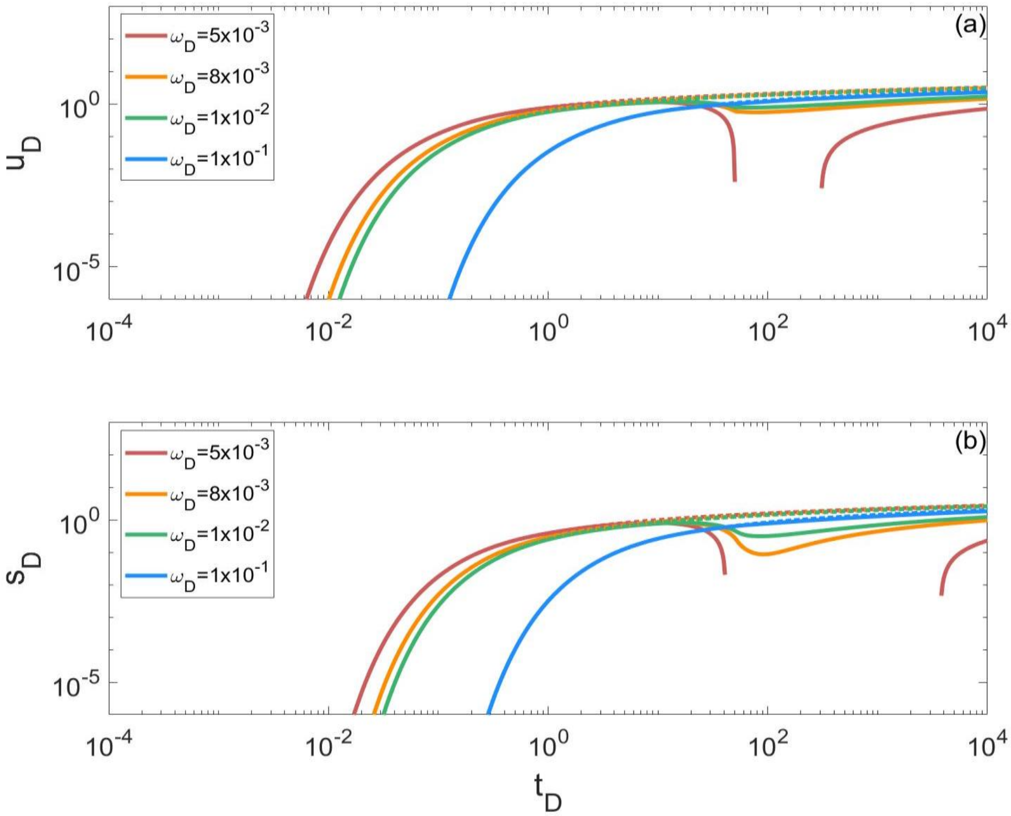

Figure 2-9 The dimensionless time t_D vs. the dimensionless hydraulic head increments u_D and s_D with I_D = -0.3 during $t_D \in [10^{-2}, 50]$ (solid curves) and without I_D (dotted curves): (a) t_D vs. u_D for different values of the dimensionless unsaturated constitutive exponent ω_D, where r_D = 0.1, z_D = 0.1, $S_{yD} = 1\times10^3$ and K_D = 1; (b) t_D vs. s_D for different values of the dimensionless unsaturated constitutive exponent ω_D, where r_D = 0.1, z_D = -0.1, $S_{yD} = 1\times10^3$ and K_D = 1.

Figure 2-10 shows the hydraulic head increments change with the dimensionless GSF generated by evapotranspiration $I_D = -0.3$ during $t_D \in [10^{-2}, 50)$ (solid curves) and without I_D (dotted curves) for the dimensionless specific yield $S_{yD} = 5\times10^2, 8\times10^2, 1\times10^3$ and 1×10^4, where $\omega_D = 1\times10^{-2}$ and $K_D = 1$. Like in Figure 2-9, the presence of I_D decreases u_D and s_D. A smaller S_{yD} leads to smaller u_D and s_D, for the reason that it represents a smaller storage capacity of the unsaturated zone. When S_{yD} is very small, u_D and s_D may become negative for some time and then increases after I_D stops.

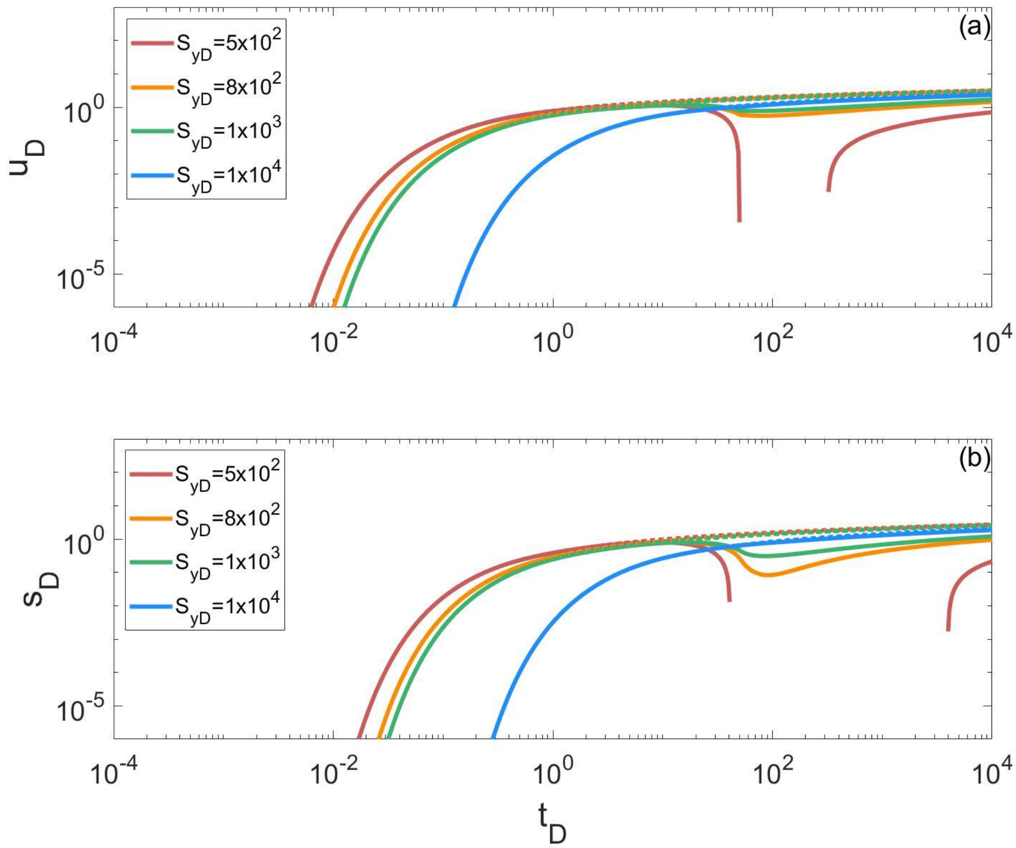

Figure 2-10 The dimensionless time t_D vs. the dimensionless hydraulic head increments u_D and s_D with I_D = -0.3 during $t_D \in [10^{-2}, 50]$ (solid curves) and without I_D (dotted curves): (a) t_D vs. u_D for different values of the dimensionless specific yield S_{yD}, where r_D = 0.1, z_D = 0.1, $\omega_D = 1\times10^{-2}$ and K_D = 1; (b) t_D vs. s_D for different values of the dimensionless specific yield S_{yD}, where r_D = 0.1, z_D = -0.1, $\omega_D = 1\times10^{-2}$ and K_D = 1.

Figure 2-11 shows the hydraulic head increments change with the dimensionless GSF generated by evapotranspiration $I_D = -0.3$ during $t_D \in [10^{-2}, 50)$ (solid curves) and without I_D (dotted curves) for the hydraulic conductivity anisotropy $K_D = 0.01, 0.1, 1, 10$, where $\omega_D = 1 \times 10^{-2}$ and $S_{yD} = 1 \times 10^3$. The presence of I_D decreases

u_D and s_D. The smaller the K_D, the later this influence occurs. The reason is that a smaller K_D indicates that the horizontal flow is dominant in the unsaturated zone at early stage and it is more difficult for water to be evaporated through the ground surface. Then the influence of GSF generated by evapotranspiration on s_D in the saturated zone is also delayed.

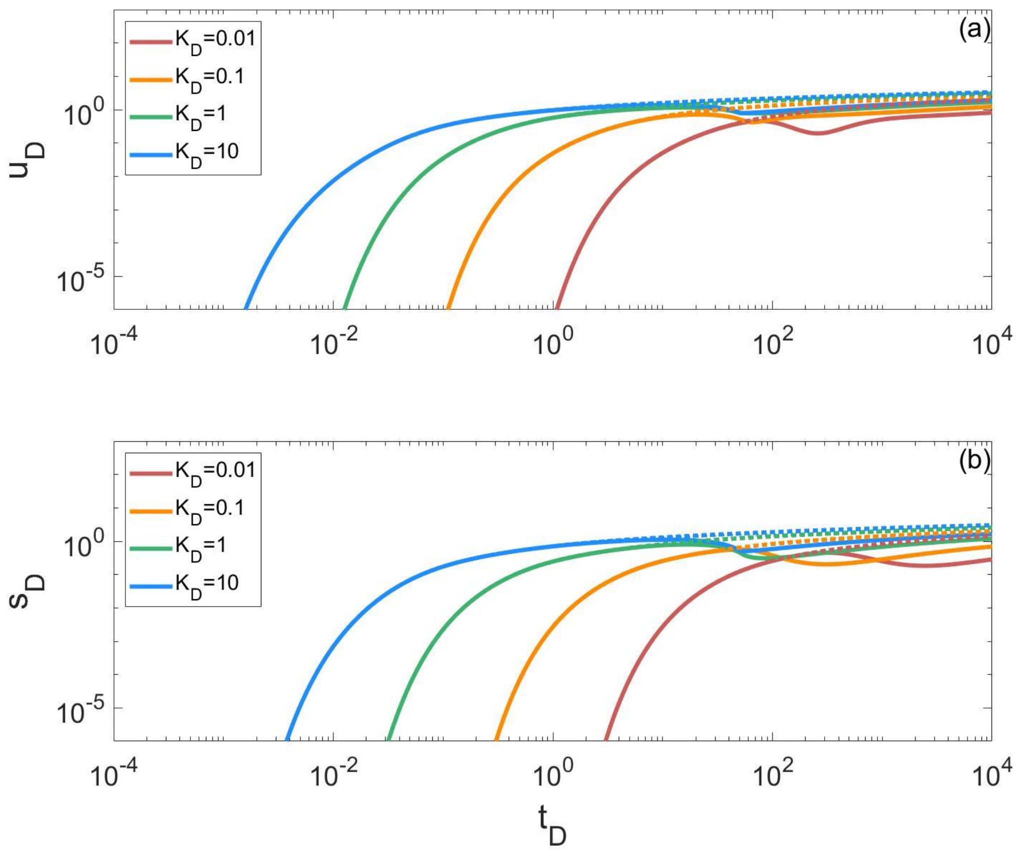

Figure 2-11 The dimensionless time t_D vs. the dimensionless hydraulic head increments u_D and s_D with I_D = -0.3 during $t_D \in [10^{-2}, 50]$ (solid curves) and without I_D (dotted curves): (a) t_D vs. u_D for different values of the hydraulic conductivity anisotropy K_D, where $r_D = 0.1$, $z_D = 0.1$, $\omega_D = 1\times10^{-2}$, and $S_{yD} = 1\times10^3$; (b) t_D vs. s_D for different values of the hydraulic conductivity anisotropy K_D, where $r_D = 0.1$, $z_D = -0.1$, $\omega_D = 1\times10^{-2}$, and $S_{yD} = 1\times10^3$.

Figure 2-12 shows the hydraulic head increments change with different values of dimensionless GSF generated by evapotranspiration $I_D = 0, -0.1, -0.3, \text{and} - 0.5$, where $\omega_D = 1 \times 10^{-2}$, $S_{yD} = 1 \times 10^3$, and $K_D = 1$. In Figure 2-12(1), I_D is applied during $t_D \in [10^{-2}, 50)$. u_D and s_D decrease as the absolute value of I_D increases. A larger absolute value of I_D means that more water is evaporated through the ground surface, leading to faster decrease of u_D. When the absolute value of I_D is very large, the evapotranspiration effect is so strong that water will move upward through the saturated zone, leading to negatives values of s_D. In Figure 2-12(2), I_D is applied during $t_D \in [200, 250)$. After relatively long VZW injection, the GSF is applied, which causes gradual decreases of u_D and s_D. The decreases of u_D and s_D are less than those in Figure 2-12(1). For short time VZW injection, injected water only flows in the vicinity of the well. GSF generated by evapotranspiration is playing a dominating role and can lead to more hydraulic head decreases over most parts of aquifer that are not in the vicinity of the injection well.

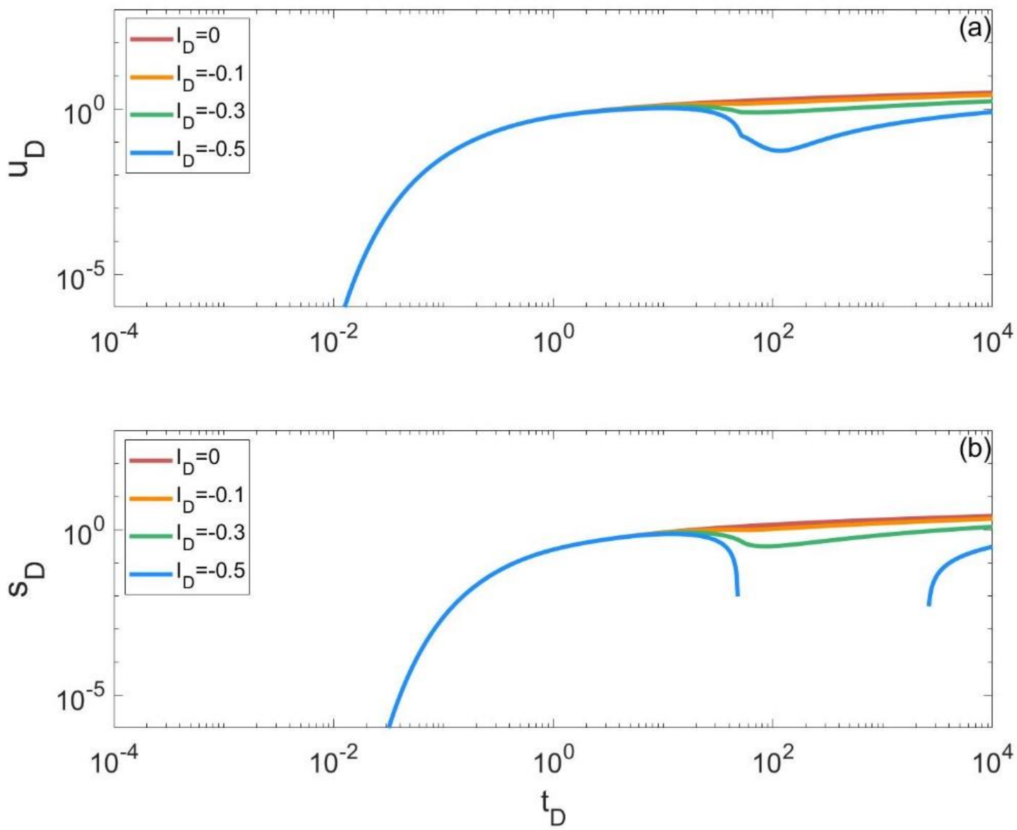

(1)

Figure 2-12 The dimensionless time t_D vs. the dimensionless hydraulic head increments for different values of the dimensionless GSF generated by evapotranspiration, where $r_D = 0.1$, $\omega_D = 1\times10^{-2}$, $S_{yD} = 1\times10^3$, and $K_D = 1$: (1) I_D is applied during $t_D \in [10^{-2}, 50]$: (a) t_D vs. u_D ($z_D = 0.1$); (b) t_D vs. s_D ($z_D = -0.1$). (2) I_D is applied during $t_D \in [200, 250]$: (a) t_D vs. u_D ($z_D = 0.1$); (b) t_D vs. s_D ($z_D = -0.1$).

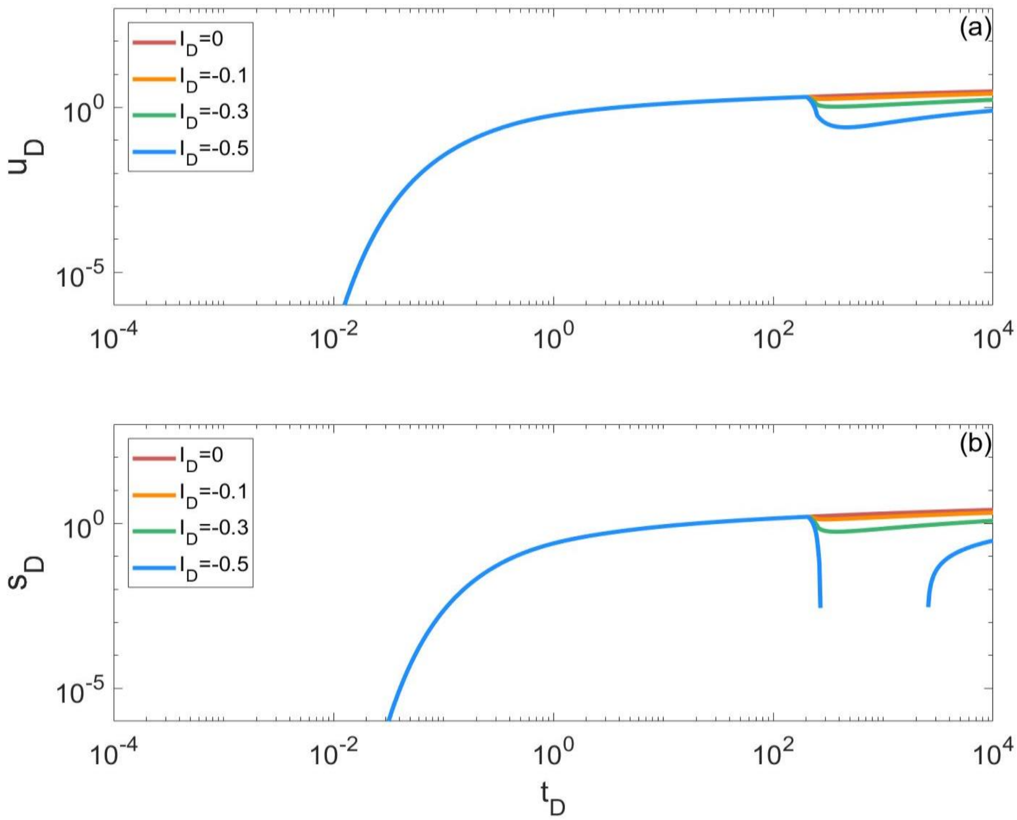

(2)

Figure 2-12 Continued.

Figure 2-13 demonstrates how the dimensionless infiltration rate at the interface of the unsaturated and saturated zones changes with different dimensionless GSF generated by evapotranspiration $I_D = 0, -0.3, -0.5, \text{and} -1$ during $t_D \in [10^{-2}, 50)$ where $\omega_D = 1 \times 10^{-2}$, $S_{yD} = 1 \times 10^3$, and $K_D = 1$. For $I_D = 0$, q_D increases as t_D increases at the early stage and then reaches a constant value. The presence of I_D decreases q_D and a larger I_D induces a smaller q_D. The figure at the lower right corner of Figure 2-13 zooms in the curves of $t_D \in [45, 55)$. It shows that after $t_D = 50$ when I_D stops, q_D gradually increases to a constant value, which is not influenced by the value of

I_D. The reason is that GSF generated by evapotranspiration reduces the water into the unsaturated zone and the saturated zone, giving rise to a lower q_D. When I_D stops, this influence also stops.

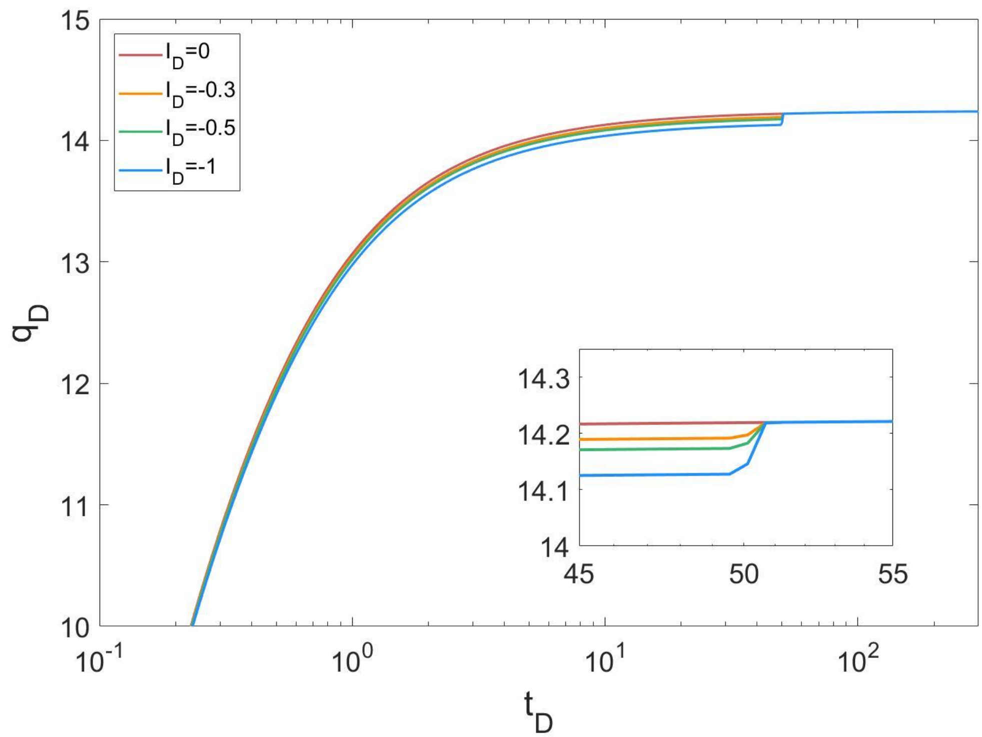

Figure 2-13 The dimensionless time t_D vs. the dimensionless infiltration rate at the interface of the unsaturated and saturated zones q_D for different values of the dimensionless GSF I_D generated by evapotranspiration, where r_D = 0.1, $\omega_D = 1\times10^{-2}$, $S_{yD} = 1\times10^{3}$, and K_D = 1.

2.5 Discussion

In this study, there are several assumptions and limitations which are needed to discuss here:

1) The coupled unsaturated and saturated flow system is difficult to solve because of the nonlinear nature of Richards' equation and the presence of a moving

interface (water table) between two different (saturated and unsaturated) flow regimes. To solve this problem, the method of perturbation expansion was employed by Kroszynski and Dagan (1975) to simplify the Richards' equation by linearization. This method assumes that the flow departs only slightly from equilibrium and expands the dependent variables in Richards' equation in perturbation series. Neglecting higher order terms in the series and substituting the remaining terms into the equation can obtain a first-order linearized equation. These simplifications have been tested and applied in previous studies on coupling unsaturated-saturated flow problems (Chang et al., 2018; Dagan, 1967; Liang et al., 2017a; Lin et al., 2017; Mathias and Butler, 2006; Tartakovsky and Neuman, 2007). For instance, Mishra et al. (2012) solved the problem of constant-rate pumping in a coupled saturated and unsaturated flow system and compared the drawdown curves predicted by the analytical solution with the Gardner's model and the numerical solution with the van Genuchten-Mualem soil constitutive model. The comparison showed good agreement in the predicted drawdown curve at early and late times. This indicates that the linearization method can be adopted for approximating the flow induced by VZW injection and GSF for a coupled unsaturated-saturated system when the flow differs slightly from its equilibrium state. However, this method may not be valid when flow differs considerably from its equilibrium state. For instance, when the injection rate is sufficiently large that the flow departs greatly from its equilibrium state. If this is true, one probably has to adopt a higher-order approximation to deal with the problem, which will make the analytical treatment difficult or even impossible. For such a case, we will recommend using a numerical approach rather than analytical approach to tackle the problem of concern. All of these issues are out of the scope of this investigation and should be examined separately.

2) This study applies Gardner (1958) constitutive model (the two-parameter model) and assumes that the relative hydraulic conductivity and water content vary exponentially with incremental capillary pressure head relative to the air entry pressure head. As the three- and four- parameters constitutive models (Mathias and Butler, 2006; Mishra and Neuman, 2010) have been proposed, the application of more flexible constitutive models in VZW injection should be investigated in the future.

3) The well radius is assumed to be infinitely small in this study while Bouwer (2002) referred that VZWs are usually 1-2 m in diameter. For such finite radius wells, the wellbore storage may cause errors in prediction of hydraulic head changes at the early stage of VZW injection. And the presence of well skin during injection can change the hydraulic properties around the well and affect the recharge capacity. The effects of wellbore storage and well skin should not be ignored in the future.

4) In VZW management, clogging of VZW is another issue that has not been included in this study but could affect the performance of VZW in real applications. Clogging of VZWs may include the physical clogging in which fine materials block the entrance of the well screen, or biological clogging in which growth of bacterial blocks the pathways of the well screen. Clogging can also reduce the permeability of formations immediately adjacent to VZWs. Further investigation is certainly needed to address the clogging issue of VZWs, which has been reported in several field applications (Bloetscher et al., 2014; Jeong et al., 2018; Martin, 2013).

2.6 Conclusion

The conclusions of this study are summarized as follows:

1. The presence of GSF generated by infiltration can increase the hydraulic head increments in the unsaturated and saturated zones, and the magnitude of this influence depends on properties of unsaturated and saturated zones and the value of GSF. Smaller ω_D and S_{yD} lead to larger increases of u_D and s_D when GSF is the same. A small K_D can delay the increases of u_D and s_D and the value of K_D does not affect the final values of u_D and s_D. In addition, larger values of GSF generated by infiltration lead to larger increases of u_D and s_D.
2. The presence of GSF generated by evapotranspiration can decrease the hydraulic head increments in the unsaturated and saturated zones, and the magnitude of this influence depends on properties of unsaturated and saturated zones and the value of GSF. Smaller ω_D and S_{yD} lead to larger decreases of u_D and s_D when GSF is the same. A small K_D can delay the decreases of u_D and s_D and the value of K_D does not affect the final values of u_D and s_D. In addition, larger absolute values of GSF generated by evapotranspiration lead to larger decreases of u_D and s_D.
3. The presence of GSF generated by infiltration can increase the infiltration rate at the interface of the unsaturated and saturated zones and larger values of GSF lead to larger increases of q_D. After GSF stops, the infiltration rate gradually decreases to a constant value, which is not influenced by the value of GSF generated by infiltration.

4. The presence of GSF generated by evapotranspiration can decrease the infiltration rate at the interface of the unsaturated and saturated zones and larger absolute values of GSF lead to larger decreases of q_D. After GSF stops, the infiltration rate gradually increases to a constant value, which is not influenced by the value of GSF generated by evapotranspiration.

CHAPTER 3

GOEMETRIC AND SOIL PROPERTY CONTROL ON THE RECHARGE OF VADOSE ZONE INJECTION WELLS

This study focuses on improving the knowledge of VZW performance by conducting numerical experiments. A finite-element numerical VZW model based on the commonly used Van Genuchten (1980) - Mualem (1976) constitutive model (the VGM model) is developed by COMSOL Multiphysics. Then numerical experiments are conducted to investigate the geometric and soil properties control on the performance of VZW injection and to evaluate their influences on the arrival time and cumulative infiltration volume of injected water. In addition, the influences of different arrangements of injection plan with a given total injection water volume are also investigated in this study. We will try to answer the question that when the total volume of injection is given, is it able to improve recharge of VZW by injecting with a larger rate within a relatively shorter duration, or is it able to improve recharge of VZW by injecting with a smaller rate within a relatively longer duration?

3.1 The conceptual model

Figure 3-1 demonstrates the conceptual model of this study: a vadose zone well is drilled into a slightly compressible unconfined aquifer resting on a horizontal impermeable boundary. Both the unsaturated and saturated zones are homogeneous, anisotropic, and extend sufficiently far laterally. The initial water table is horizontal and the saturated zone has a uniform thickness of *b*. The unsaturated zone is lying above the saturated zone and has a uniform thickness of *a*. A vadose zone well with a constant recharge rate *Q* is screened from *j* to *d*, where *j* and *d* are distances from the top and bottom of the screen to the initial position of water table, respectively. The origin of the cylindrical coordinate system is set at the intercept of the central axis of the well and the ground surface. The *r*-axis is along the horizontally radial water flow direction, and the *z*-axis is vertically upward. The initial water table is at the elevation $z = -a$.

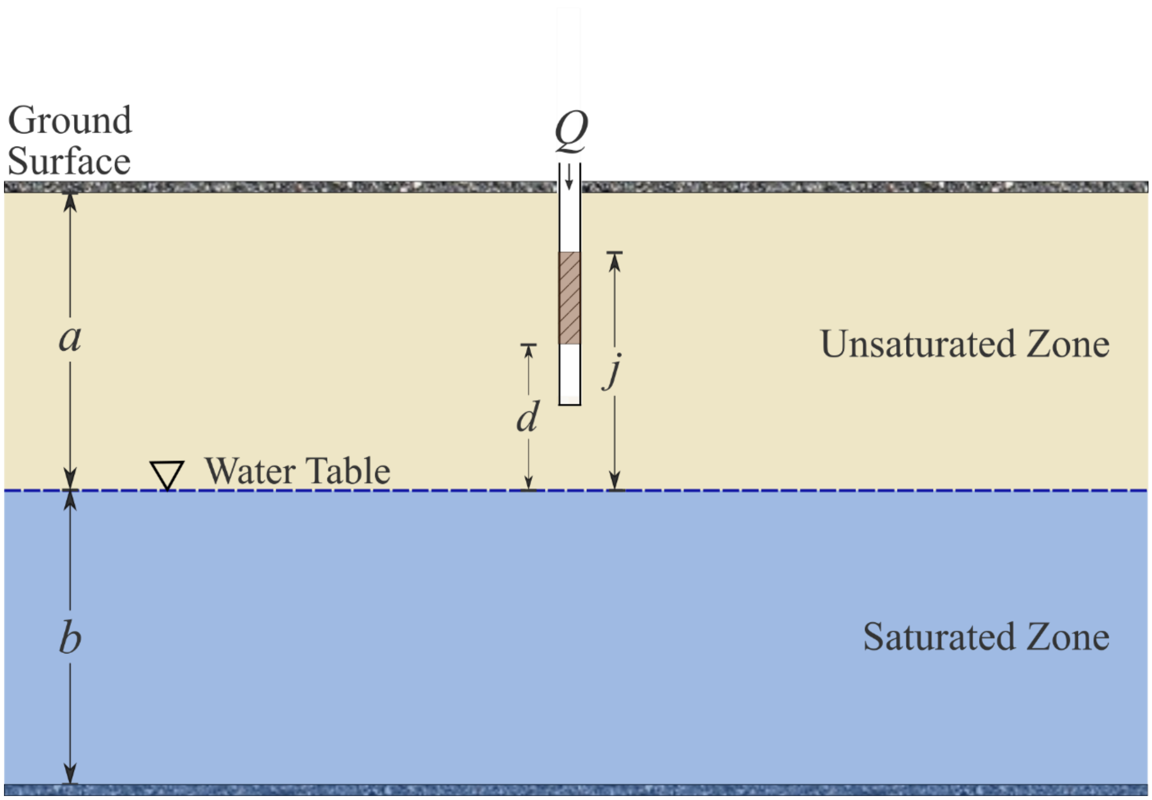

Figure 3-1 The schematic diagram of unsaturated-saturated flow induced by the vadose zone well injection.

3.2 The numerical model

The 2D axisymmetric numerical model is established by COMSOL Multiphysics and its geometry is shown in Figure 3-2. The Richards' equation governs the saturated-unsaturated flow of water in the aquifer:

$$(C + S_e S_s)\frac{\partial \psi}{\partial t} + \nabla \cdot \left(-K_s k_r \nabla(\psi + D)\right) = 0 \qquad (3.1)$$

where C is the specific soil moisture capacity $[\mathrm{L}^{-1}]$ and $C = \frac{d\theta}{d\psi}$; S_e is the effective saturation of the soil $[-]$; S_s is the specific storage $[\mathrm{L}^{-1}]$; ψ is the pressure head [L]; t is time [T]; K_s is the saturated hydraulic conductivity $[\mathrm{LT}^{-1}]$; k_r is the relative permeability of the soil and $k_r = \frac{K}{K_s}$ $(0 \le k_r \le 1)$ $[-]$, K is the hydraulic conductivity at water content θ $[\mathrm{LT}^{-1}]$; D is the elevation head [L].

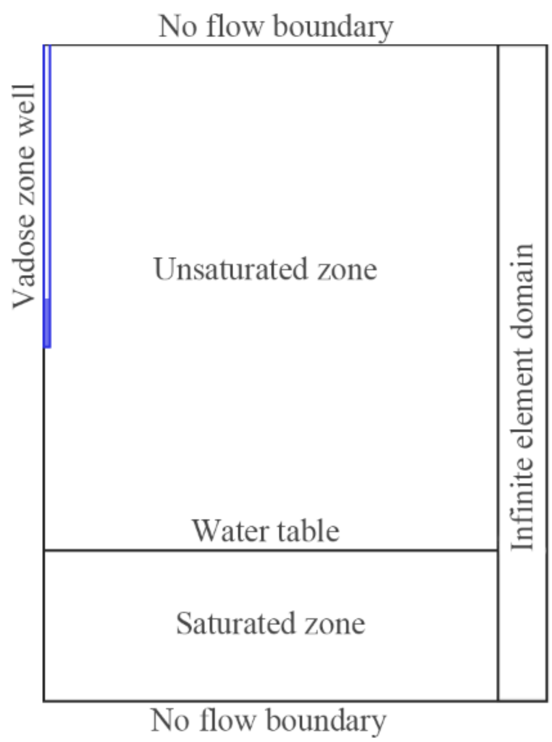

Figure 3-2 The geometry of the 2D axisymmetric numerical model.

The VGM model is used to describe the water retention and relative hydraulic conductivity of the unsaturated zone:

$$S_e = \begin{cases} \frac{1}{[1+|\alpha\psi|^n]^m} & \psi < 0 \\ 1 & \psi \geq 0 \end{cases} \tag{3.2}$$

$$k_r = \begin{cases} {S_e}^l \left[1 - \left(1 - {S_e}^{\frac{1}{m}}\right)^m\right]^2 & \psi < 0 \\ 1 & \psi \geq 0 \end{cases} \tag{3.3}$$

where α is a parameter corresponding approximately to the inverse of the air-entry value [L^{-1}]; n and m are shape parameters [$-$] and $m = 1 - \frac{1}{n}$; l is the pore size interaction term and an optimal value of 0.5 for l is derived by Mualem (1976) when using measured K_s as the matching point.

The top and bottom boundaries of the model are set as no flow boundaries. The right boundary of the model is assigned as a pressure head boundary with pressure head $\psi = -(z + a)$ m. The rectangular domain near the right boundary is set as the infinite element domain to simulate the region of infinite extent. Infinite elements represent a region that is stretched along certain coordinate axes such that boundary conditions on the outside of the infinite element layer are effectively applied at a very large distance. This feature enables us to truncate the model to a reasonable size and accurately capture the behavior in the region of interest. The left boundary of the model is on the symmetry axis and is set as the axial symmetry node. The initial condition in the domain is specified in terms of the pressure head ψ and is set as $-(z + a)$ m. The initial saturated zone thickness b is 3 m and the unsaturated zone thickness a is 10 m. The vadose zone well injection rate Q is $0.0015\ \mathrm{m}^3/\mathrm{s}$ and the well is screened from $d = 4$ m to $j = 5\ m$.

The values of hydraulic properties of different soil materials used in this study are summarized in Table 3-1 based on the research of Carsel and Parrish (1988).

Table 3-1 Values of hydraulic properties of different soil materials

Soil Texture (USDA)	θ_r (m^3/m^3)	θ_s (m^3/m^3)	α (cm^{-1})	n (-)	K_s (cm/d)	l (-)
Clay Loam	0.095	0.41	0.019	1.31	6.24	0.5
Loam	0.078	0.43	0.036	1.56	24.96	0.5
Sandy Loam	0.065	0.41	0.075	1.89	106.08	0.5

Source: Data from Carsel and Parrish (1988).
θ_r - residual water content; θ_s - saturated water content;
α - a parameter corresponding approximately to the inverse of the air-entry value;
n - shape parameter; K_s - the saturated hydraulic conductivity;
l - the pore size interaction term.

The simulation domain is discretized by triangular elements. Since the injection flow changes significantly around the injection well and the interface between the unsaturated and saturated zones, the finite-element discretization meshes are refined at these positions with the minimum element size of 0.001 m and an element size growth rate of 1.01. The total number of triangular elements is 13795. The settings of the simulation time vary with different numerical tests, which will be given in the following sections.

3.3 Issues of the soil constitutive model and numerical versus analytical approaches

Before analyzing the results, it is essential to address a few issues associated with the selected soil constitutive model and the numerical and analytical approaches to solve the mathematical model discussed above. We will first discuss the issue related to the chosen constitutive model and then address the issue associated with the approach, either numerical or analytical.

First, we need to point out that although the VGM model is selected here as the constitutive model, this model is only an approximation of the unsaturated soil and usually cannot capture the entire complex soil moisture dynamics. In another word, uncertainty is inherent and inevitable when using a constitutive model with a few controlling parameters to describe the soil moisture dynamics in a complex soil structure. It is also likely that different investigators may use different constitutive models to deal with the same unsaturated soil. Therefore, how will the result depend on the chosen constitutive model should be addressed.

Second, when a relatively complex constitutive model such as the VGM model is used, it is almost impossible to develop an analytical solution for the pressure head (or hydraulic head) distribution, and numerical solution appears to be the choice for solving the mathematical model. The highly nonlinear Richard's equation is notorious for a host of numerical problems such as non-divergence (or slow convergence) of solutions and sometimes sizable numerical errors (Farthing and Ogden, 2017; Gao et al., 2019; Zha et al., 2019). Therefore, it is necessary to examine the performance of the numerical solution and if possible, assessing the numerical errors associated with the selected numerical method. Unfortunately, without an analytical solution, or a semi-analytical solution at least, the numerical solution cannot be benchmarked and tested. The semi-analytical solution is often the case for analytically solving the partial differential equation in Laplace domain if Laplace transform is used (or frequency domain if Fourier transform is used) and then subsequently obtaining the real-time solution using numerical inverse of Laplace transform (or solution in space domain using numerical inverse of Fourier transform).

Facing with above challenges, we propose the following method to resolve the issue. First, we are trying to find a constitutive model that is not as complex as the VGM model but it can still faithfully describe the soil moisture dynamics, and furthermore, such a constitutive model is amendable for analytical treatment. The Gardner's model (or G model hereinafter) (Gardner, 1958) is selected and it has the following equations to describe the relative permeability and volumetric water content.

$$k_r = e^{\omega(\psi-\psi_a)} \quad (3.4)$$

$$\theta = \theta_r + S_y e^{\omega(\psi-\psi_a)} \quad (3.5)$$

where θ is volumetric water content $[-]$; θ_r is the residual water content $[-]$; θ_s is the saturated water content $[-]$; ψ_a is the air entry pressure head ($\psi \leq \psi_a \leq 0$); $S_y = \theta_s - \theta_r$ is the specific yield $[-]$; $\omega > 0$ is a constitutive exponent [L^{-1}], reflecting the ability of the water holding in the unsaturated zone.

If one recalls the definition of the effective saturation S_e as $S_e = (\theta - \theta_r)/(\theta_s - \theta_r) = (\theta - \theta_r)/S_y$, then from above Eqs. (3.4) and (3.5), one can see that S_e=k_r for the G model. In another word, the two separate equations used to describe S_e and k_r in the VGM model now merge into a single equation in the G model. In this sense, one may regard the G model as a simplified version of the VGM model. The relatively simple G model (in contrast to the more complex VGM model) is amendable for analytical solution and thus has been used extensively in modeling soil moisture dynamics in the unsaturated zone, including the study associated with VZW (Liang et al., 2018; Qi et al., 2020). In Chapter 2, a mathematical model of VZW injection with ground surface flux is established based on linearized Richards' equation considering the G model for the unsaturated zone, and the semi-analytical solutions of hydraulic head increments and recharge rate at water table are derived. To use the solutions in Chapter 2, proper parameter values of the G model must be known in advance. For a loam aquifer previously described by the VGM model whose parameters listed in Table 3-1, we can use the G model to best-fit the VGM model by the least square method. Specifically, this is done by choosing the parameters of the G model that would minimize the deviations of the fitted G model from the VGM model. The effective saturation (S_e) curve and the relative hydraulic conductivity (k_r) curve of the G model become one curve as explained above. This curve is used to fit the S_e and k_r curves of the VGM model at the same time. The goodness of the fitting is evaluated by the adjusted R^2 and its value of 0.932 is generally considered acceptable, where the adjusted R^2 is a modified version of the conventional R^2 value that has been adjusted for the number of predictors of concern, and it is always less than the R^2 value. For detailed explanation of the adjusted R^2, one can consult the reference of Westfall and Arias (2020). Figure 3-3 shows the best fit of the G model (dashed curves) to the VGM model (solid curves). The S_e curves are represented by blue curves and the k_r curves are represented by red curves. The best-fitting yields parameter estimations of $\omega = 0.0318$ cm^{-1} and $\psi_a = 0$ cm for the G model. The ground surface flux is set as 0. The values of other parameters are the same as used in the developed numerical model. The total simulation time is 1005 hr and the time step grows exponentially, starting at 1×10^{-2} hr. One can see that discrepancy is inevitable between the G model and the VGM model. More specifically, the G model gives an identical S_e (and k_r) curve that is between the curves of S_e and k_r for the VGM model.

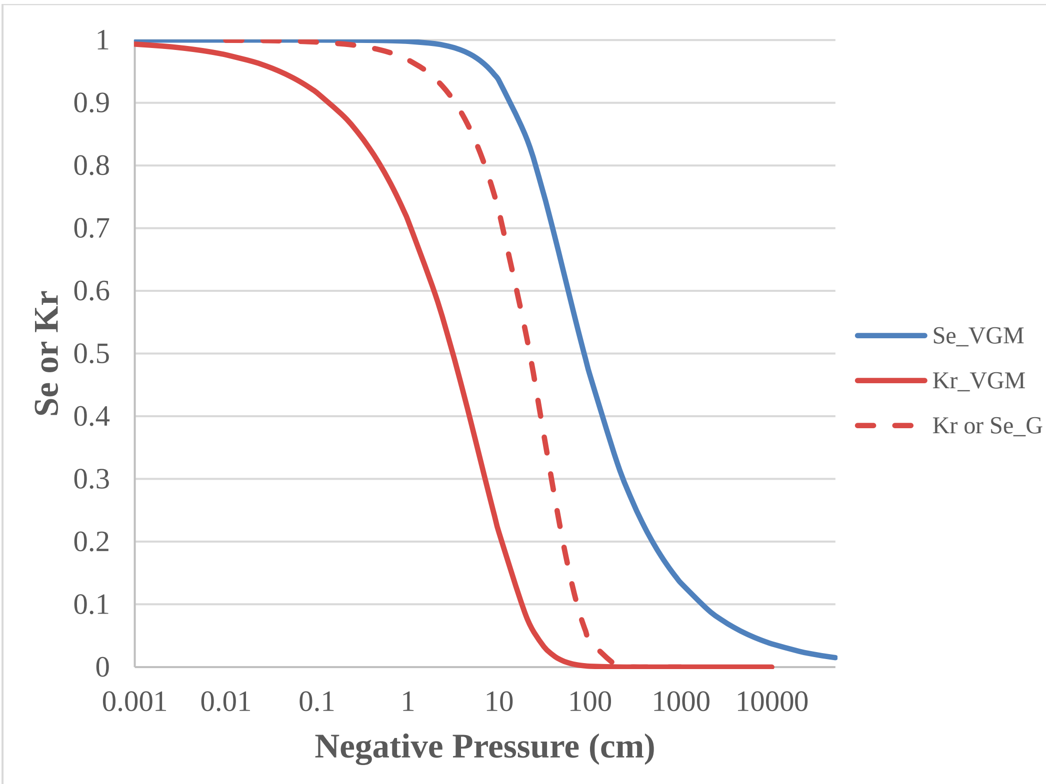

Figure 3-3 The best least square fit of the G model (dashed curve) to the VGM model (solid curves) for loam.

For the G model, a numerical simulation with exactly the same finite-element mesh design and conceptual model setup as this study has been conducted in Chapter 2 for homogenous aquifer. The numerical simulation result was compared with the analytical result and they agreed with each other very well. This implies that the numerical errors associated with the finite-element method are controlled under a negligible level, at least for the case when the soil is described by the G model. Although one cannot completely assure that the same conclusion can be made when the soil is described by a different soil constitutive model such as the VGM model, there is no reason to believe that the change of a different soil constitutive model will dramatically introduce significant numerical errors, provided that the conceptual model and the numerical scheme both remain the same. Based on this argument, we assume that any discrepancy between the hydraulic head distributions computed using the VGM model and the best-fitted G model comes from the different choices of the constitutive model, not from the numerical errors of the numerical simulation.

Figure 3-4 shows the comparison of the numerical solutions (dashed curves) (using the VGM model) with the semi-analytical solutions (solid curves) (using the best-fitted G model). The hydraulic head increments induced by VZW injection are plotted with time in a semi-logarithmic fashion for points with different values of z, where $r = 1\ m$. The changes of u at different points of the two solutions are similar. As z decreases from -5 m to -9 m, both solutions of u get a delayed increase and reach a smaller value at later stage.

In summary, although the overall trend of the numerical solution and semi-analytical solution are similar in Figure 3-4, the differences between the solutions for different soil constitutive models are clearly visible. Given the fact that the actual soil characteristics can be complex and may be approximated by different soil constitutive models such as the VGM model and the G model by different investigators, the inherent uncertainty of results associated with the choice of the soil constitutive model should not be overlooked. Given the popularity of the VGM model, it will be used in the following numerical simulations of both homogeneous and heterogeneous soils.

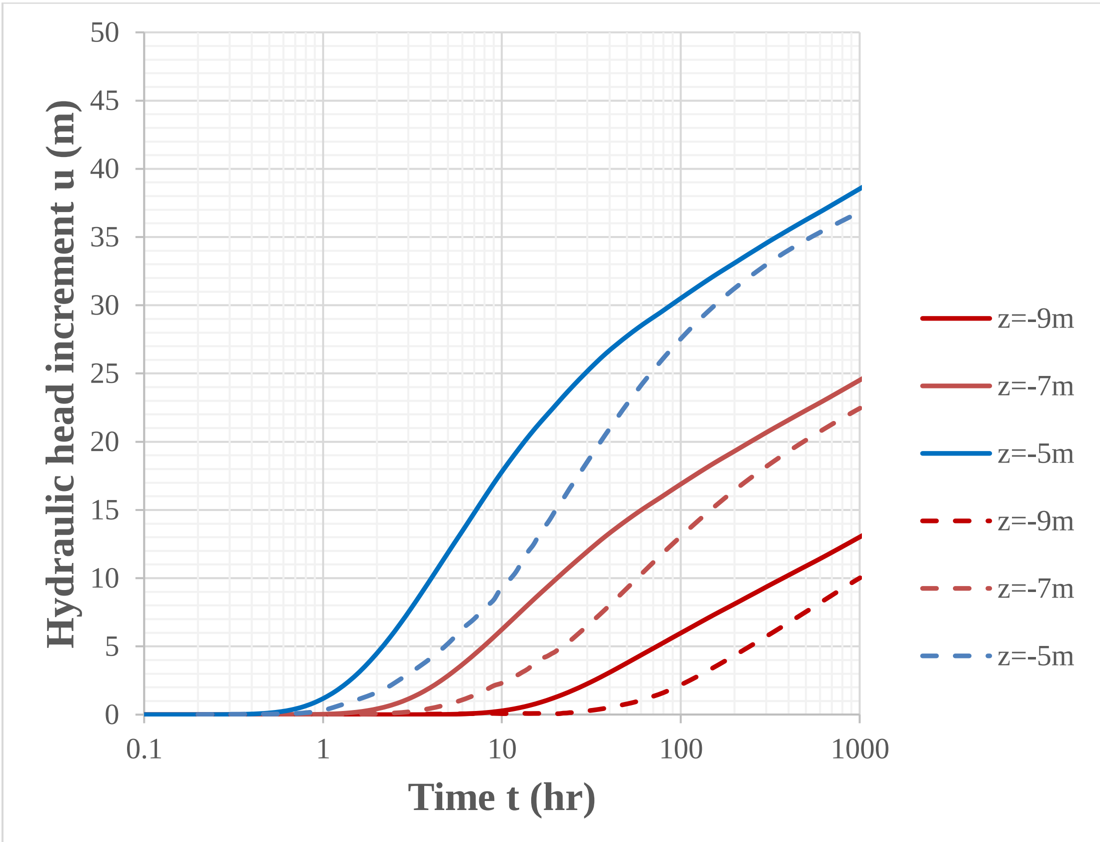

Figure 3-4 Comparison of the numerical solutions (dashed curves) with the semi-analytical solutions (solid curves): the time *t* (hr) vs. the hydraulic head increments *u* (m) in the unsaturated zone (*z* = -9, -7 and -5 m), where *r* = 1 m.

3.4 Numerical experiments

The developed 2D axisymmetric model is applied to investigate the geometric and soil property control on the performance of VZW injection. As VZW injection is conducted in the region of infinite radial extent and the injection rate is relatively small, the flow departs slightly from equilibrium and the water table position remains unchanged, except for the area directly below and near the VZW. Therefore, the initial water table is considered as the observation surface and two solutions are used to evaluate the performance of VZW injection during the numerical experiments. One solution is the characteristic arrival time of the injected water t_a, which is the travel time of injected water to reach the saturated zone. It has great effects on the geometric design of the VZW because the characteristic arrival time can tell us how long it takes for the injected water to recharge the water table through the vadose zone. A small enough recharge index σ (such as 1%-5%) is defined as the ratio of the overall volumetric recharge rate reaching the water table (Q_{wt}) over the injection rate Q of VZW to quantify the characteristic arrival time. In the following analysis, we choose σ=2% as an example to compute the characteristic arrival time. The VZW injection rate Q is set as $0.0015\ \mathrm{m}^3/\mathrm{s}$ based on the VZW design in Scottsdale, Arizona (ToddGroundwater, 2019). The other solution is the cumulative recharge volume V_{wt} at the initial water table, which gives the estimation of amount of water entering the saturated zone. V_{wt} is computed using the integration of Q_{wt} over time.

To investigate the soil property control on the performance of VZW injection, three soils (sandy loam, loam, and clay loam) are selected as the aquifer materials to simulate VZW performance and the values of the aquifer parameters are summarized in Table 3-1. The total simulation time for sandy loam is $240\ \mathrm{hr}$, for loam is $480\ \mathrm{hr}$, and for clay loam is $720\ \mathrm{hr}$. The values of other parameters are the same as described in chapter 3.2.

To investigate the well geometric control on the performance of VZW injection, two geometric parameters are considered in the simulation: the screen length (*SL*) and the screen depth (*SD*) where the screen depth refers to the depth of the center of the well screen. Two groups of numerical experiments are conducted in the loam aquifer to study their influences. The first group is designed to test the influences of *SL* on VZW performance. The *SD* is set as 6.5 m below the ground surface and remains the same during the simulation. The *SL* of 0.5, 1, and 1.5 m are tested and the total simulation time is 480 hr. The values of other parameters are the same as described in chapter 3.2. The second group is intended to test the influences of *SD* on VZW performance. The *SL* is remained as a constant of 1 m and the *SD* of 6, 6.5, and 7.5 m are tested. The total simulation time is 480 hr. The values of other parameters are the same as described in chapter 3.2.

Another important factor controlling the performance of VZW is the injection plan, which is also investigated in this study for the loam aquifer with a VZW screened from $d = 3$ m to $j = 4\ m$. The total volume of injected water is fixed at 2592 m^3. In plan 1, the water is injected through VZW with an injection rate of 0.0015 m^3/s for 480 hr. In plan 2, the water is injected through VZW with an injection rate of 0.0025 m^3/s for 288 hr. In plan 3, the VZW injection rate is 0.002 m^3/s for the first 240 hr and then is reduced to 0.001 m^3/s for the second 240 hr. In plan 4, the VZW injection rate is 0.001 m^3/s for the first 240 hr and then increases to 0.002 m^3/s for the second 240 hr. The values of other parameters are the same as described in chapter 3.2.

The purpose to investigate different injection plans is to optimize the engineering application of the VZWs.

3.5 Results

3.5.1 Soil property control on recharge of VZW

Figure 3-5 demonstrates the flow of injected water in sandy loam, loam and clay loam aquifers by the effective saturation S_e profiles at different times. For coarser soils, the pore sizes are larger and the initial hydraulic conductivity $K(\theta)$ is lower in the unsaturated zone. During VZW injection, the wetting front gradually advances and eventually reaches the water table. After the arrival of the wetting front, the volumetric water content θ increases and $K(\theta)$ finally reaches the saturated hydraulic conductivity K_s. As coarser soils have larger K_s, the wetting area in the sandy loam aquifer is larger than that of the other two aquifers at the same time. And it takes much less time for the injected water to reach the saturated zone in coarser soils. To learn about the soil properties control on the recharge of VZW injection, the volumetric infiltration rate at water table Q_{wt} and the cumulative infiltration volume at water table V_{wt} are calculated and plotted in the following figures.

The simulation results for the sandy loam, loam and clay loam aquifers are plotted and compared in Figure 3-6. Figures 3-6a and 3-6b show the recharge of VZW in three aquifers through the change of Q_{wt} with time and the change of V_{wt} with time, respectively. The changes of Q_{wt} are similar for three aquifers: Q_{wt} increases rapidly at the early stage and then gradually approaches to an asymptotic value as time increases.

For coarse grained aquifers, it takes less time for water to reach the water table and the asymptotic value of Q_{wt} is larger. Besides, the cumulative recharge volume V_{wt} is larger in coarse grained aquifers and less water is trapped in the vadose zone. The comparison of VZW injection in three different aquifers indicates that aquifer properties have a great influence on recharge of VZW. Coarse grained aquifers have larger pore sizes and it is easier for injected water to infiltrate into the saturated zone. The performance of VZW injection is greatly improved in the aquifer of coarser soils with much less travel time of the injected water and more cumulative recharge volume to the saturated zone.

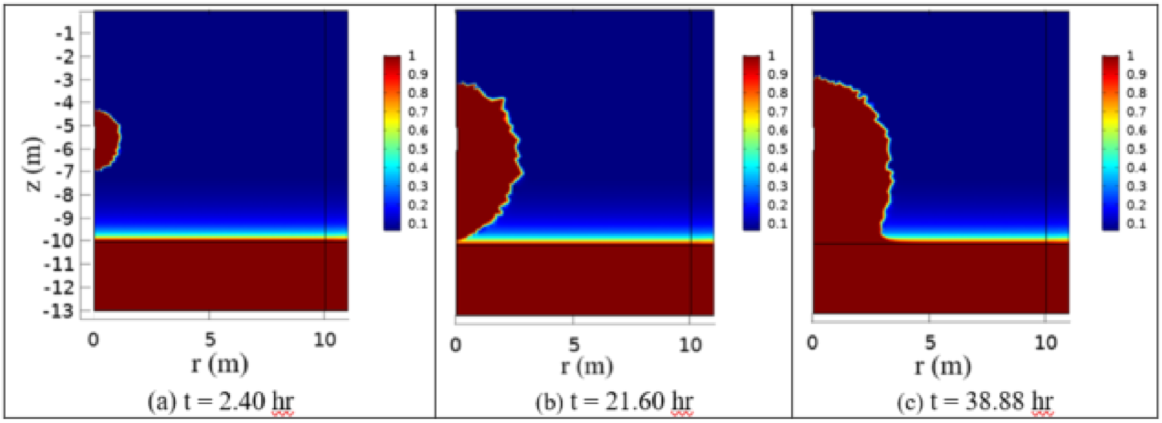

(1)

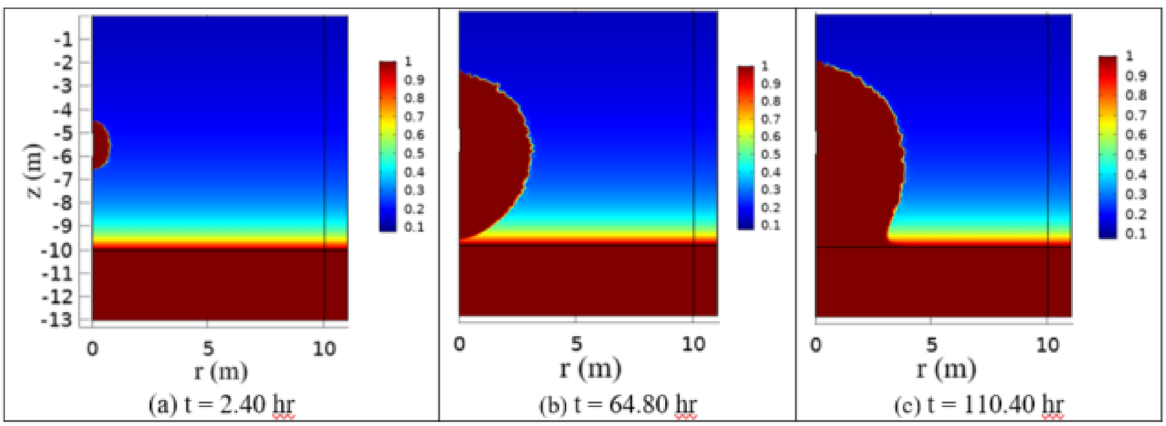

(2)

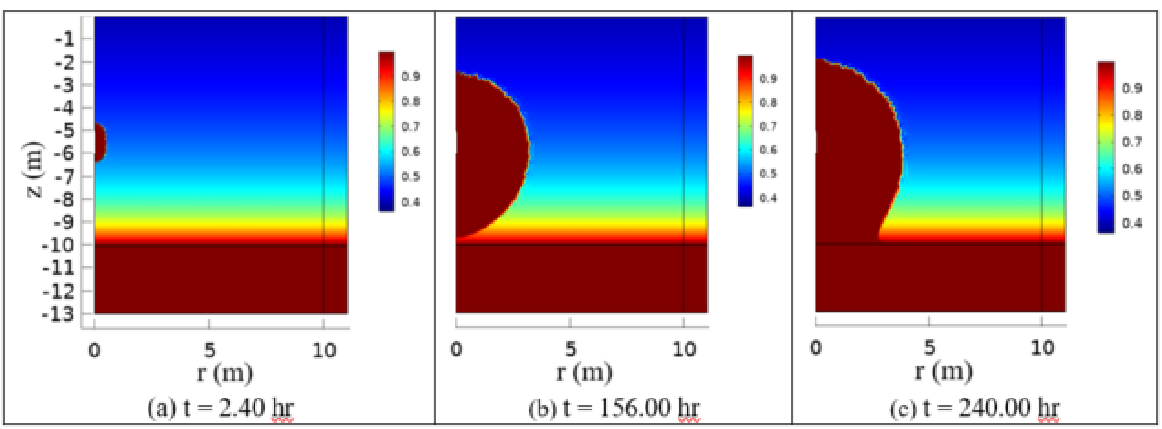

(3)

Figure 3-5 The effective saturation S_e profiles for sandy loam, loam and clay loam aquifers: (1) S_e profiles for sandy loam aquifer at t = 2.40, 21.60 and 38.88 hr; (2) S_e profiles for loam aquifer at t = 2.40, 64.80 and 110.40 hr; (3) S_e profiles for clay loam aquifer at t = 2.40, 156.00 and 240.00 hr.

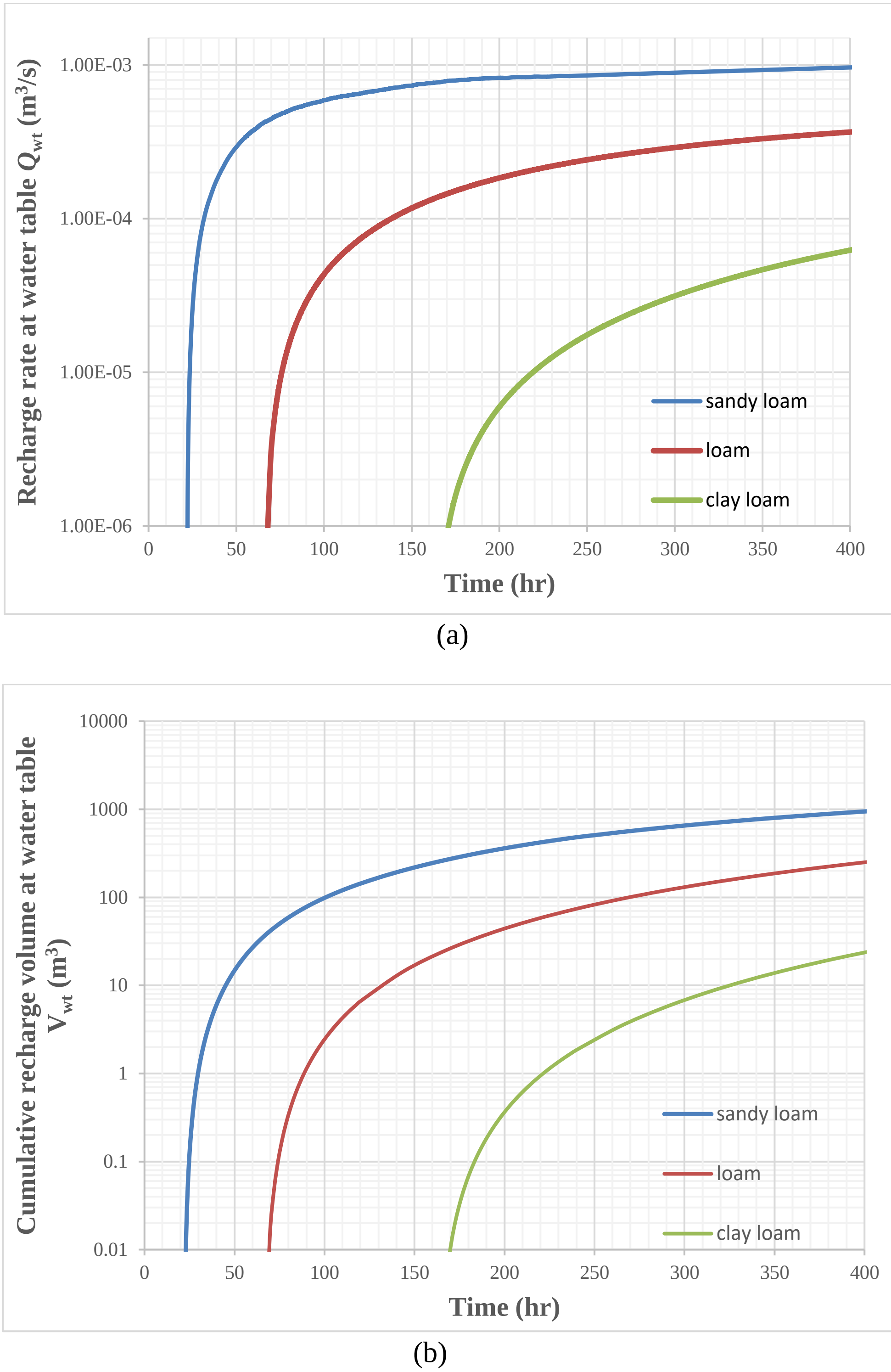

Figure 3-6 (a) The recharge rate Q_{wt} vs. time t for sandy loam, loam and clay loam aquifers; (b) the cumulative recharge volume V_{wt} vs. time t for sandy loam, loam and clay loam aquifers.

3.5.2 Geometric property control on recharge of VZW

The simulation results in the loam aquifer for different SL (0.5, 1 and 1.5 m) are plotted in Figure 3-7, where the *SD* is -6.5 m: Figure 3-7a demonstrates the change of Q_{wt} with time and Figure 3-7b demonstrates the change of V_{wt} with time. In Figure 3-7a, the curves of Q_{wt} for different *SL* have slight differences at early times and the values of Q_{wt} at the same time increase slightly when the *SL* increases. These differences of Q_{wt} gradually diminish over time. During the tests, the injection rate Q is set as a constant and *SD* remains the same. The increase of SL enables water to infiltrate through a larger area and promotes the diffusion of injected water in the unsaturated zone, causing slight influences on Q_{wt} at early times. In Figure 3-7b, the change of V_{wt} corresponds to that of Q_{wt} and small differences of V_{wt} curves appear at early times, then diminish over time.

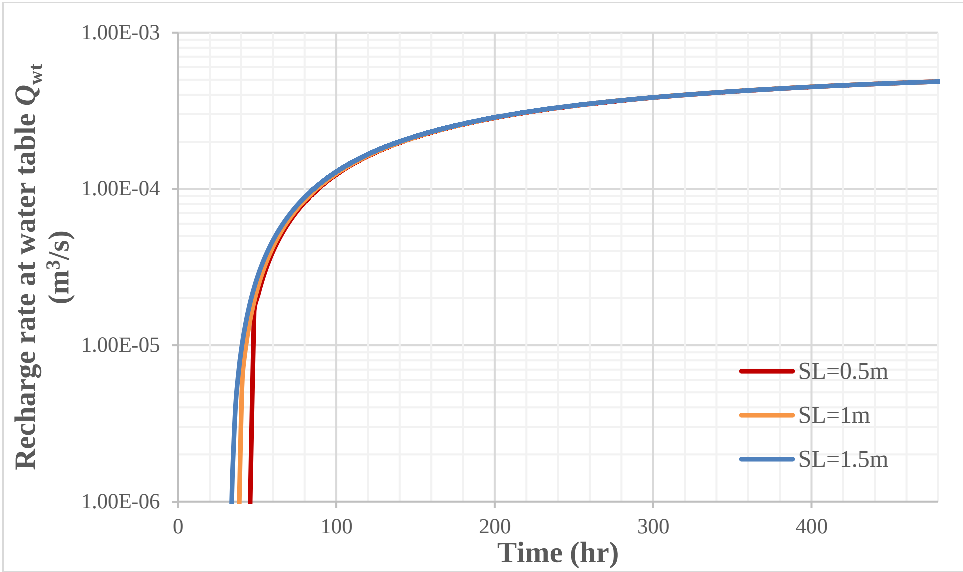

(a)

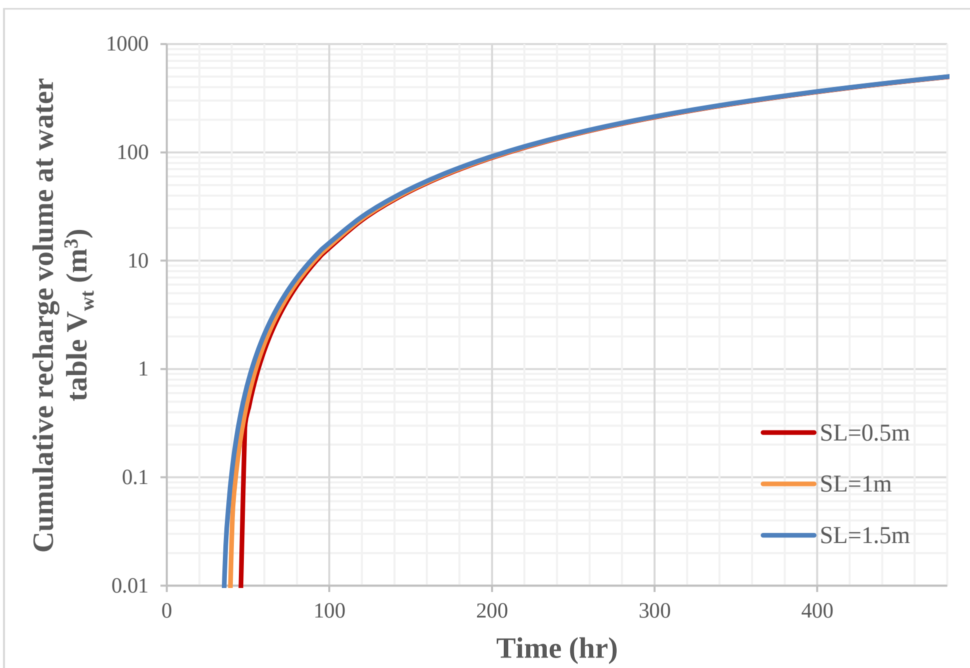

(b)

Figure 3-7 The recharge rate Q_{wt} and cumulative recharge volume V_{wt} at water table in the loam aquifer for SL = 0.5, 1 and 1.5 m, where SD is -6.5 m: (a) Q_{wt} vs. t; (b) V_{wt} vs. t.

The simulation results in the loam aquifer for different SD ($-6, -6.5$ and -7.5 m) are plotted in Figure 3-8, where SL is 1 m: Figure 3-8a demonstrates the change of Q_{wt} with time and Figure 3-8b demonstrates the change of V_{wt} with time. SD has a profound impact on the performance of VZW injection when other factors remain the same. In Figure 3-8a, t_a decreases when SD becomes deeper. When SD becomes deeper, the distance between the well screen and the water table decreases, reducing the travel time of injected water to reach the water table. Figure 3-8b shows that V_{wt} increases with SD. When SD becomes deeper, more water flows into the saturated zone in a shorter period of time.

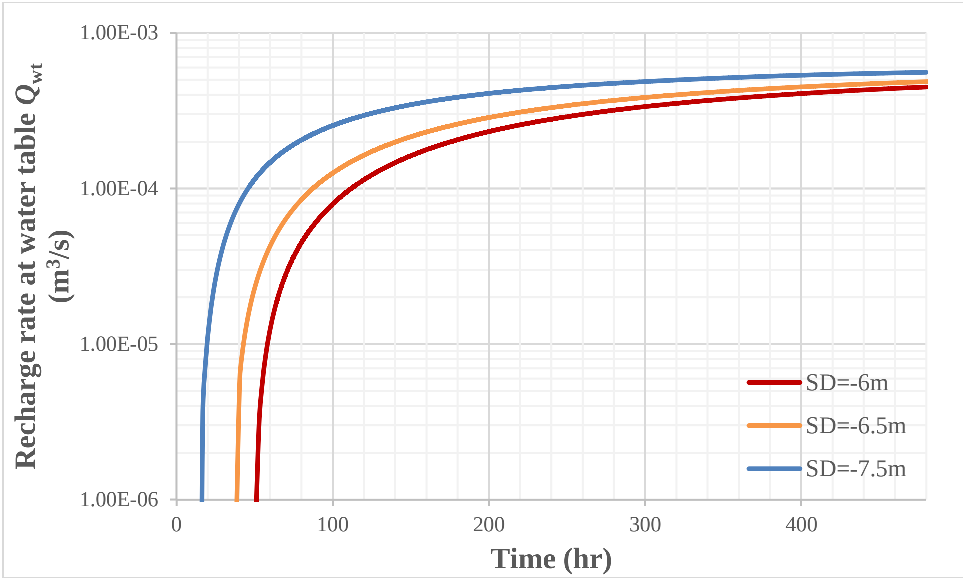

(a)

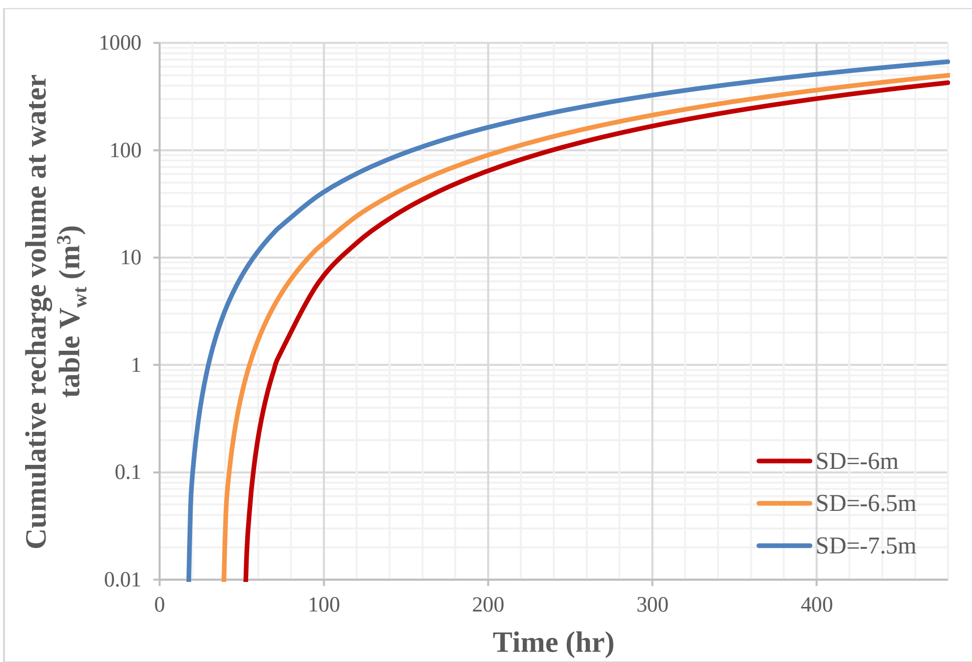

(b)

Figure 3-8 The recharge rate Q_{wt} and cumulative recharge volume $\boldsymbol{V_{wt}}$ at water table in the loam aquifer for SD = -6, -6.5 and -7.5 m, where SL is 1 m: (a) Q_{wt} vs. t; (b) V_{wt} vs. t.

The well geometric control on the performance of VZW injection is mainly reflected in the travel distance of the injected water to recharge the aquifer. The increases of *SL* and *SD* can shorten the travel distance, which reduce the time of recharging the target aquifer and improve the performance of VZW injection.

3.5.3 Injection plan influence on recharge of VZW

The simulation results in the loam aquifer for different injection plans are plotted in Figure 3-9: Figure 3-9a presents the change of Q_{wt} with time and Figure 3-9b presents the change of V_{wt} with time. Plans 1 and 2 inject 2592 m^3 water by VZW with a constant injection rate. In plan 1, VZW injects water at the rate of $0.0015\ \mathrm{m}^3/\mathrm{s}$ for 480 hr and t_a is 75.36 hr. The recharge rate Q_{wt} keeps as 0 at the beginning and then increases rapidly after the injected water reaches the water table. After the VZW injection stops for a while, Q_{wt} starts to decrease. In plan 2, VZW injects water at the rate of $0.0025\ \mathrm{m}^3/\mathrm{s}$ for 288 hr and t_a is 59.44 hr. The increase of Q_{wt} is larger than that in plan 1 and Q_{wt} starts to decrease earlier than that in plan 1 since VZW injection stops at 288 hr. The cumulative recharge volume at the water table V_{wt} is larger than that in plan 1 and this difference decreases with time after VZW injection stops.

Plans 3 and 4 inject 2592 m^3 water by VZW with different injection rates at different stages. In plan 3, the VZW injects water at $0.002\ \mathrm{m}^3/\mathrm{s}$ for the first 240 hr and then at $0.001\ \mathrm{m}^3/\mathrm{s}$ for the second 240 hr. The value of t_a in plan 3 is 65.73 hr. Compared with Q_{wt} in plan 1, Q_{wt} is larger at the first injection stage and smaller at the second injection stage in plan 3. The value of Q_{wt} at 480 hr in plan 3 is smaller than that in plan 1. V_{wt} increases with time in plan 3, which is larger than that in plan 1. In plan 4, the VZW injects water at $0.001\ \mathrm{m}^3/\mathrm{s}$ for the first 240 hr and then at $0.002\ \mathrm{m}^3/\mathrm{s}$ for the second 240 hr. Compared with Q_{wt} in plan 1, Q_{wt} is smaller at the first injection stage and larger at the second injection stage in plan 4. The value of t_a is 93.12 hr in plan 4. In plan 4 V_{wt} increases with time and is smaller than that in plan 1.

Comparison of different injection plans indicates that the arrangement of injection plan has great influences on the performance of VZW injection when the total amount of injected water is constant. Adopting a larger injection rate at early stage of VZW injection can shorten the arrival time and increase the cumulative recharge water volume.

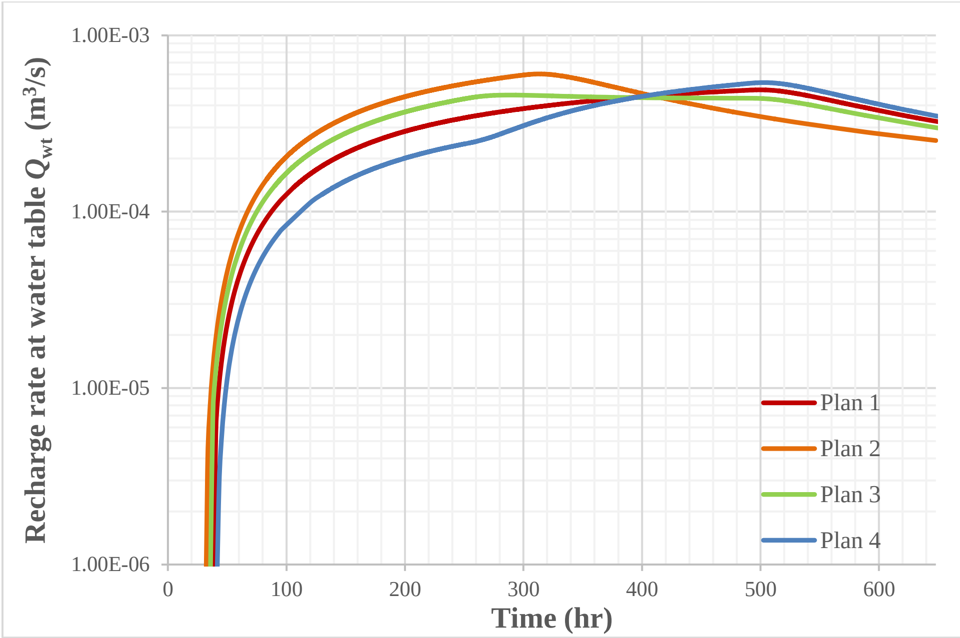

(a)

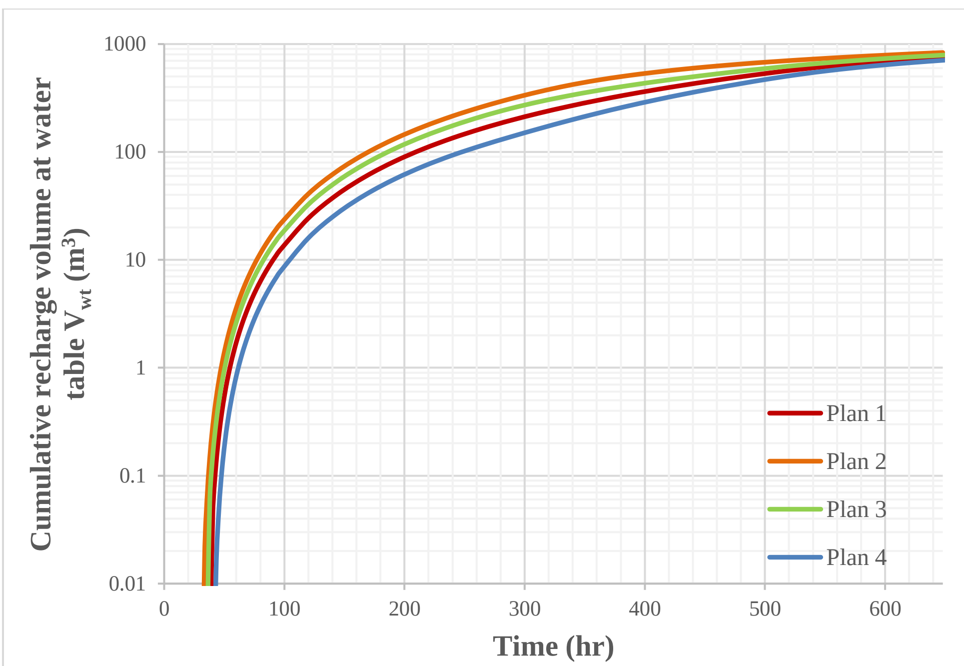

(b)

Figure 3-9 The recharge rate Q_{wt} and cumulative recharge volume V_{wt} at water table in the loam aquifer for different injection plans: (a) Q_{wt} vs. t; (b) V_{wt} vs. t.

3.6 Discussion

There are several issues about assumptions and limitations of this study that deserve further discussion.

Firstly, clogging, as one of the major obstacles to the sustainable operation of MAR, is not included in this study. There are four main types of clogging occurred in MAR: physical clogging, chemical clogging, biological clogging, and mechanical clogging (Martin, 2013; Xian et al., 2019; Zhang et al., 2020). VZW system is vulnerable and is easily affected by clogging. Clogging can cause declines in recharge rates and ultimately the failure of artificial recharge systems (Jeong et al., 2018). Various techniques have been proposed to estimate and predict clogging in MAR. The clogging issues of VZW such as decrease of injection rate certainly need further investigations in future studies.

Secondly, this study simulates VZW injection in a homogeneous aquifer to access the impacts of various factors, which contribute to a better understanding of the role played by each factor. However, the heterogeneous aquifers are more common in field cases (Maples et al., 2019; Ward et al., 2008). Two types of media heterogeneity usually appear in the vadose zone: one type is layering as the aquifer is composed of several soil layers with different hydraulic properties; the other type is isolated lens in the aquifer with higher or lower hydraulic conductivity. The aquifer heterogeneity can substantially complicate the flow pattern of injected water and increase the difficulty in VZW management. Further investigations on including the aquifer heterogeneity into the model are valuable to provide more guidance on VZW design and they are presented in Chapter 4.

3.7 Conclusion

The conclusions of this study are summarized as follows:

1. The soil properties of the aquifer have great influences on the performance of VZW injection. Coarser soils are beneficial to the flow of injected water in the aquifer. Due to the significant decrease of travel time and increase of cumulative recharge volume, the performance of VZW can be greatly improved in coarser soils.
2. The well geometric properties have relatively large impacts on the performance of VZW injection as well. When the injection rate and *SD* remain the same, the increase of *SL* leads to minor decrease of arrival time and minor increase of cumulative recharge water volume. When the injection rate and *SL* remain the same, the increase of *SD* leads to significant decrease of arrival time and considerable increase of cumulative recharge volume. By shortening the travel distance of injected water through changing the well geometric properties, the performance of VZW injection can be improved greatly.
3. When the total amount of injected water is constant, the arrangement of injection plan has a great influence on the performance of VZW injection. The volumetric recharge rate at water table Q_{wt} increases with the injection rate and the application of a higher injection rate at early times can shorten the arrival time t_a. By adopting a larger injection rate at early stage of VZW injection, the performance of VZW can be

improved with less arrival time and increased cumulative recharge volume to the saturated zone.

CHAPTER 4

VADOSE ZONE WELL INJECTION IN HETEROGENEOUS AQUIFER

This study focuses on improving the knowledge of VZW recharge by conducting numerical experiments to study the influences of subsurface heterogeneity. A finite-element numerical VZW model based on the commonly used VGM constitutive model is developed by COMSOL Multiphysics. Then numerical experiments are conducted to investigate subsurface heterogeneity control on the recharge of VZW injection. The subsurface heterogeneity in this study is considered as the deterministic subsurface heterogeneity which is presented as a low permeable layer/lens in the vadose zone. When the geologic records show that the horizontal strata are continuous and have distinctively different hydraulic properties which can be quantified using various hydrological and geophysical methods such as slug tests (Bouwer and Rice, 1976), multi-level tests with inflatable packers (Holloway and Waddell, 2008), flow meters (Hanson and Nishikawa, 1996), etc., the layered subsurface heterogeneity can be characterized in great details and our model can be used to represent such deterministic subsurface heterogeneity.

4.1 The conceptual model

Figure 4-1 shows the conceptual model of this study: a vadose zone well is drilled in a slightly compressible unconfined aquifer resting on a horizontal impermeable boundary. The saturated zone is homogeneous and extend sufficiently far laterally from the well. The initial water table is horizontal and the thickness of the saturated zone is *b*. The unsaturated zone lies above the saturated zone and has a uniform thickness of *a*. A low permeable layer is considered in the unsaturated zone and it is horizontal. A vadose zone well with a constant recharge rate *Q* is screened from *j* to *d*, where *j* and *d* are distances from the top and bottom of the screen to the initial position of water table, respectively. The origin of the cylindrical coordinate system is set at the intercept of the central axis of the well and the ground surface. The *r*-axis is along the horizontally radial water flow direction, and the *z*-axis is vertically upward. The initial water table is at the elevation $z = -a$.

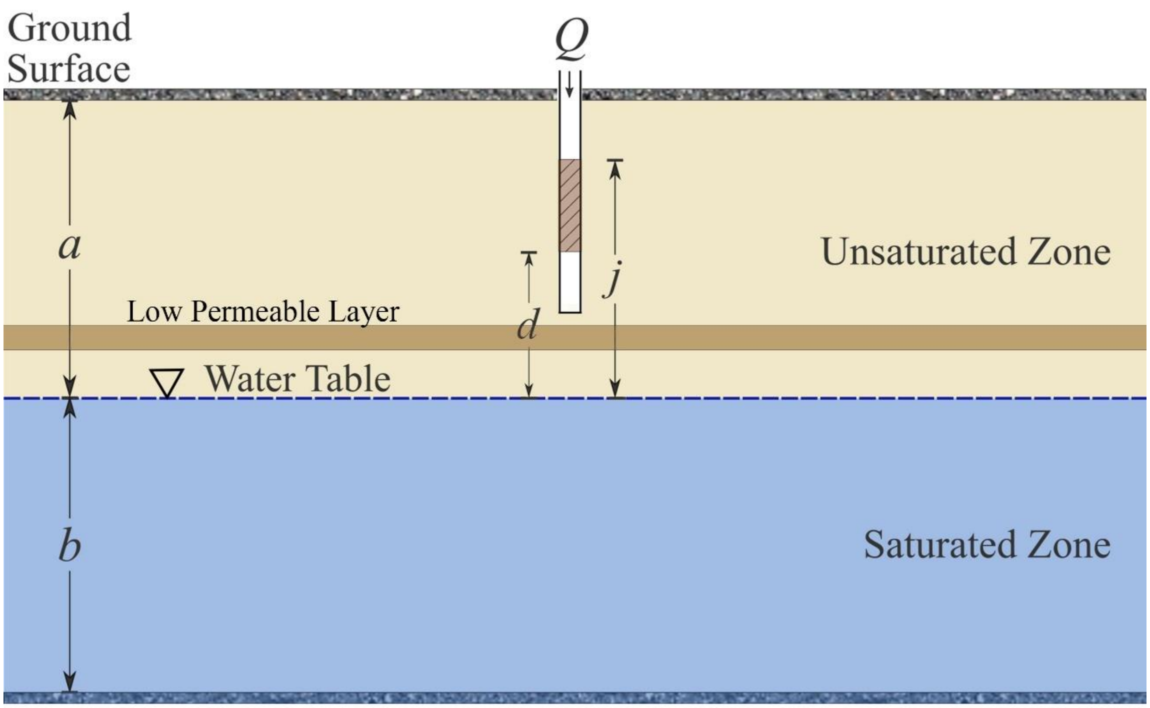

Figure 4-1 The schematic diagram of vadose zone well injection in heterogeneous aquifer.

4.2 The numerical model

The two-dimensional (2D) axisymmetric numerical model is established by COMSOL Multiphysics and its geometry is shown in Figure 4-2. The saturated-unsaturated flow of water induced by VZW injection is governed by Richards' equation:

$$(C + S_e S_s)\frac{\partial \psi}{\partial t} + \nabla \cdot \left(-K_s k_r \nabla(\psi + D)\right) = 0 \tag{4.1}$$

where C is the specific soil moisture capacity [$\mathrm{L^{-1}}$] and $C = \frac{d\theta}{d\psi}$; S_e is the effective saturation of the soil [$-$]; S_s is the specific storage [$\mathrm{L^{-1}}$]; ψ is the pressure head [L]; t is time [T]; K_s is the saturated hydraulic conductivity [$\mathrm{LT^{-1}}$]; k_r is the relative permeability of the soil and $k_r = \frac{K}{K_s}$ $(0 \leq k_r \leq 1)$ [$-$], K is the hydraulic conductivity at water content θ [$\mathrm{LT^{-1}}$]; D is the elevation head [L].

The VGM model is used to describe the water retention and relative hydraulic conductivity of the unsaturated zone:

$$S_e = \begin{cases} \frac{1}{[1+|\alpha\psi|^n]^m} & \psi < 0 \\ 1 & \psi \geq 0 \end{cases} \tag{4.2}$$

$$k_r = \begin{cases} {S_e}^l \left[1 - \left(1 - S_e^{\frac{1}{m}}\right)^m\right]^2 & \psi < 0 \\ 1 & \psi \geq 0 \end{cases} \tag{4.3}$$

where α is a parameter corresponding approximately to the inverse of the air-entry value [$\mathrm{L^{-1}}$]; n and m are shape parameters [$-$] and $m = 1 - \frac{1}{n}$; l is the pore size interaction term and an optimal value of 0.5 for l is derived by Mualem (1976) when using measured K_s as the matching point.

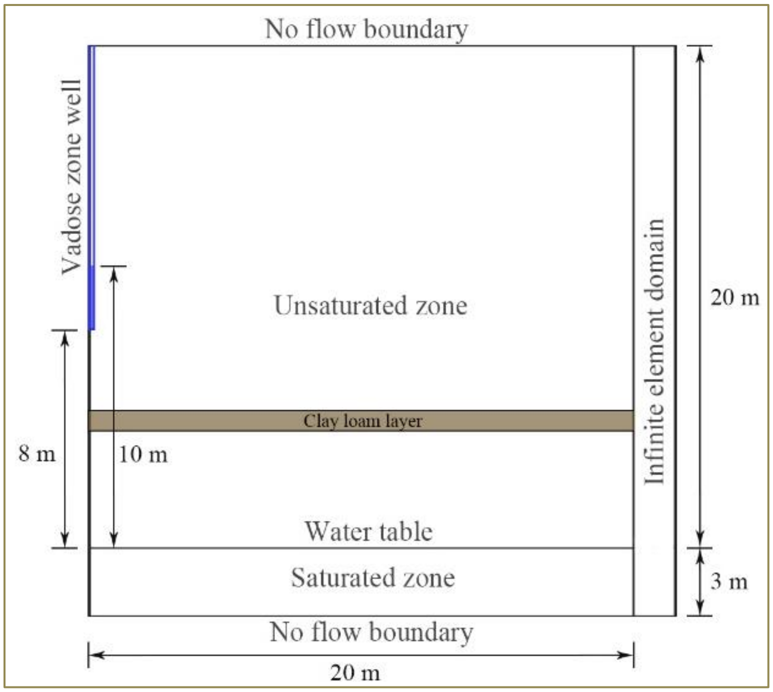

(a)

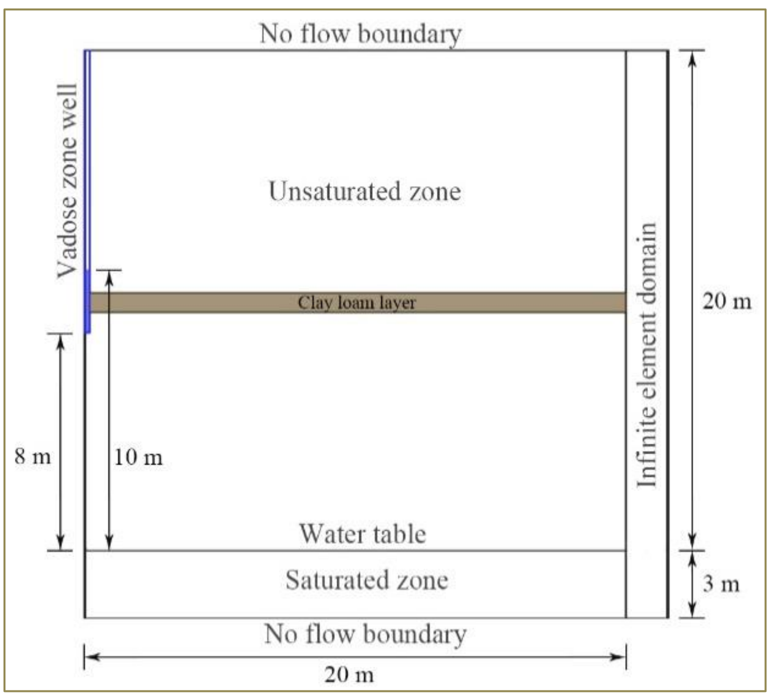

(b)

Figure 4-2 The schematic diagram of the 2D axisymmetric numerical model with a low permeable layer or lens: (a) the low permeable layer lies below the well screen; (b) the well screen cuts through the low permeable layer; (c) the low permeable lens lies below the well screen; and (d) the well screen cuts through the low permeable lens.

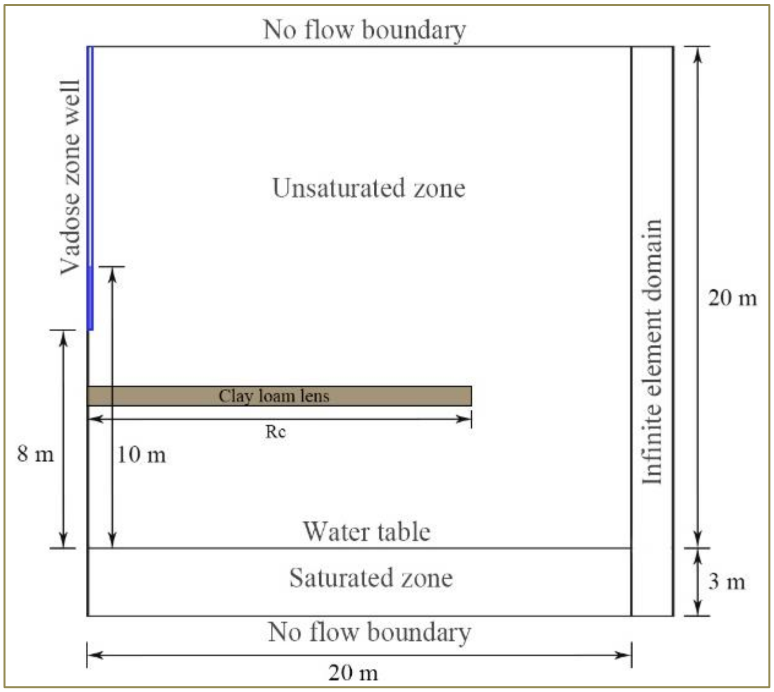

(c)

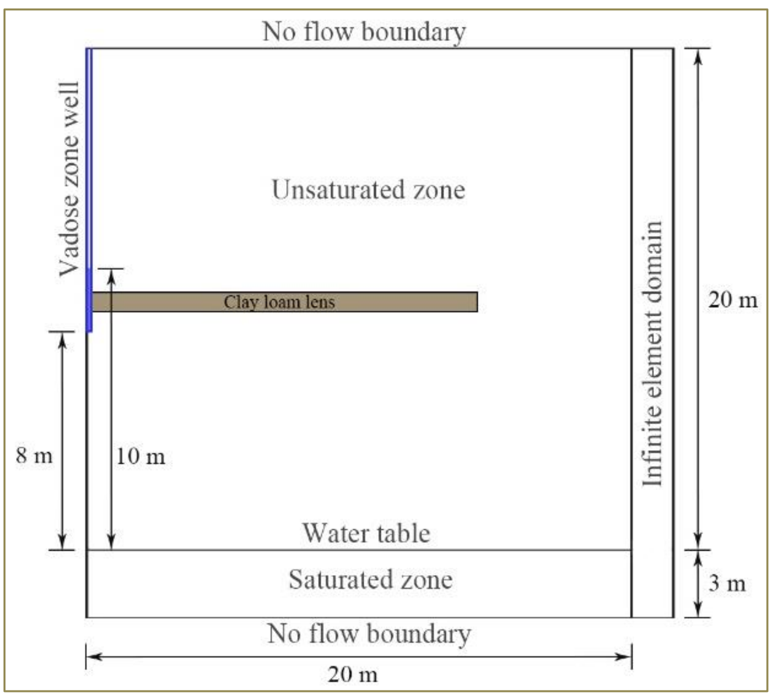

(d)

Figure 4-2 Continued.

The top and bottom boundaries of the model are set as no flow boundaries. The right boundary of the model is assigned as a pressure head boundary with pressure head $\psi = -(z + a)$ m. The rectangular domain near the right boundary is set as the infinite element domain to simulate the region of infinite extent. Infinite elements represent a region that is stretched along certain coordinate axes such that boundary conditions on the outside of the infinite element layer are effectively applied at a very large distance. This feature enables us to truncate the model to a reasonable size and accurately capture the behavior in the region of interest. The left boundary of the model is on the symmetry axis and is set as the axial symmetry node. The initial condition in the domain is specified in terms of the pressure head ψ and is set as $-(z + a)$ m. The initial saturated zone thickness b is 3 m and the unsaturated zone thickness a is 20 m. The vadose zone well injection rate Q is $0.0015\ \mathrm{m}^3/s$ and the well is screened from $d = 8$ m to $j = 10\ m$. The values of hydraulic properties of different soil materials used in this study are summarized in Table 3-1 based on the research of Carsel and Parrish (1988).

Compared to homogeneous aquifers, heterogeneous aquifers are more common in field cases. Subsurface heterogeneity usually appears in two types in the vadose zone: one type is layering as the aquifer is composed of several soil layers with different hydraulic properties; the other type is isolated lens in the aquifer with higher or lower hydraulic conductivity. Investigation of subsurface heterogeneity is usually time consuming and expensive in terms of data collection and analysis, and its uncertainty is often inevitable even with massive effort. The scenarios in which layered subsurface heterogeneity presents either as high permeable layer or low permeable layer in the soil will have profound effects on MAR and attract significant attention during MAR development and management, thus will be the primary concern of this investigation. The high permeable layer will not hinder the infiltration of the injected water. In fact, it will facilitate the infiltration of the injected water. The low permeable layer, on the other hand, can hinder the infiltration of the injected water, thus becomes a major concern in field practice. Therefore, we will only focus on the influences of the low permeable layer on the recharge of VZW in this study. In numerical tests, the aquifer material is set as loam and the low permeable layer material is set as clay loam. Figure 4-2 shows the geometry of the 2D axisymmetric numerical model with a low permeable layer or lens. For the numerical experiments considering the low permeable layer, Figure 4-2a shows the schematic diagram of the numerical model when the low permeable layer is directly below the well and Figure 4-2b shows the schematic diagram of the numerical model when the well screen cuts through the low permeable layer. For the numerical experiments considering the low permeable lens, Figure 4-2c shows the schematic diagram of the numerical model when the low permeable lens is directly below the well and Figure 4-2d shows the schematic diagram of the numerical model when the well screen cuts through the low permeable lens.

The simulation domain is discretized by triangular elements. Since the injection flow changes significantly around the injection well and the interface between the unsaturated and saturated zones, the finite-element discretization meshes are refined at these positions with the minimum element size of 0.001 m and an element size growth rate of 1.01. The total number of triangular elements is 24760. The total simulation time is 60 d and the time step settings vary with different numerical tests. The mass balance error is checked by COMSOL at the end of simulation. It is calculated by comparing the total amount of water injected with the recharge volume and the volume stored in the unsaturated zone. The mass balance errors were below 1% and these values are generally considered acceptable.

4.3 Numerical experiments

The developed 2D axisymmetric model is applied to investigate the subsurface heterogeneity control on groundwater recharge of VZW. As VZW injection is conducted in the region of infinite radial extent and the injection rate is relatively small, the flow departs slightly from equilibrium and the water table position remains unchanged, except for the area directly below and near the VZW. Therefore, the initial water table is considered as the observation surface and two solutions of the numerical simulation are used to evaluate the recharge of VZW. One solution is the characteristic arrival time of the injected water t_a, which is the travel time of injected water to reach the saturated zone. A small enough recharge index σ (such as 1%-5%) is defined as the ratio of the overall volumetric recharge rate reaching the water table (Q_{wt}) over the injection rate Q of VZW. A pre-determined recharge index σ is used to quantify the characteristic arrival time. In the following analysis, we choose σ=2% as an example to compute the characteristic arrival time. The VZW injection rate Q is set as $0.0015\ \mathrm{m}^3/\mathrm{s}$ based on the VZW design in Scottsdale, Arizona (ToddGroundwater, 2019). The other solution is the cumulative recharge volume V_{wt} at the initial water table, which gives the estimation of amount of water entering the saturated zone. V_{wt} is computed using the integration of Q_{wt} over time.

The numerical experiments simulating VZW injection in homogeneous aquifer are conducted as base cases. The aquifer is set as loam aquifer and the influences of the VGM parameters α ($\alpha = 0.036, 0.07, \text{and } 0.1 \text{ cm}^{-1}$), n ($n = 1.3, 1.56 \text{ and } 1.8$) and K_s ($K_s = 24.96, 50 \text{ and } 100 \text{ cm/d}$) on the recharge of VZW are investigated. The values of α, n and K_s are selected within the limits of variation in loam, which is summarized by Carsel and Parrish (1988). The values of other parameters in the model are the same as described in chapter 4.2.

Several numerical experiments are conducted to investigate the effects of low permeable layer's depth (the depth of the top surface of the clay loam layer $D_c = 10, 10.75, 11.5, 13.5, 15.5 \text{ and } 17.5 \text{ m}$), lateral extension (the width of the clay loam layer $R_c = 1, 3, \text{and } 5 \text{ m}$), thickness ($B_c = 0.2, 0.5, \text{and } 1 \text{ m}$) and hydraulic conductance ($\frac{K_s}{B_c} = 0.062, 0.312, \text{and } 0.1248 \text{ d}^{-1}$) on the recharge of VZW. The values of D_c are selected based on the depth of the well screen and the thickness of the unsaturated zone. The values of R_c are selected based on the change of the infiltration radius in base case simulation. The values of K_s are selected based on the range of K_s of loam aquifer in Carsel and Parrish (1988). The values of B_c are selected based on the length of the well screen and the value of the hydraulic conductance. When investigating the effects of lateral extension, the clay loam layer becomes a clay loam lens in the vadose zone with a certain value of width. In field cases, the low permeable layer/lens can appear anywhere in the aquifer, but it has the greatest impact on the recharge when it is directly below the well (i.e., the worst-case scenario). We consider this worst-case scenario in our study as shown in Figure 4-2. When the low permeable layer/lens is deep, it is usually below the well screen; when the low permeable layer/lens is shallow, the well screen cuts through the layer/lens. The values of other parameters in the model are the same as described in chapter 4.2.

4.4 Results

4.4.1 Base case analysis

Figures 4-3, 4-4 and 4-5 demonstrates the recharge of VZW in the aquifers with different values of the VGM parameters α, n and K_s, respectively. In Figure 4-3, the change of Q_{wt} with time and the change of V_{wt} with time are presented for $\alpha = 0.036, 0.07, \text{and } 0.1\ \text{cm}^{-1}$ with $n = 1.56$ and $K_s = 24.96\ \text{cm/d}$. Figure 4-3 indicates that the influence of α on the recharge of VZW is small and the increase of α leads to a slight increase of the recharge volume. In Figure 4-4, the change of Q_{wt} with time and the change of V_{wt} with time are presented for $n = 1.3, 1.56$ and 1.8 with $\alpha = 0.036\ \text{cm}^{-1}$ and $K_s = 24.96\ \text{cm/d}$. Figure 4-4 indicates that the influence of n on the recharge of VZW is relatively small and the increase of n can lead to a slight increase of recharge rate and recharge volume. In Figure 4-5, the change of Q_{wt} with time and the change of V_{wt} with time are presented for $K_s = 25, 50$ and $100\ \text{cm/d}$ with $\alpha = 0.036\ \text{cm}^{-1}$ and $n = 1.56$. Figure 4-5 indicates that K_s has great influences on the recharge of VZW. Larger K_s is beneficial to the infiltration of injected water into the saturated zone, resulting in shorter t_a and larger Q_{wt} and V_{wt}. The investigation of influences of VGM parameters on the recharge of VZW is necessary and of great practical value. In field cases, the measurement of VGM parameters can be time-consuming and expensive, and often has high uncertainty. Since the influences of α and n on the recharge of VZW are relatively small, the requirement for measuring these parameters can be reduced appropriately, saving much time and cost for field projects.

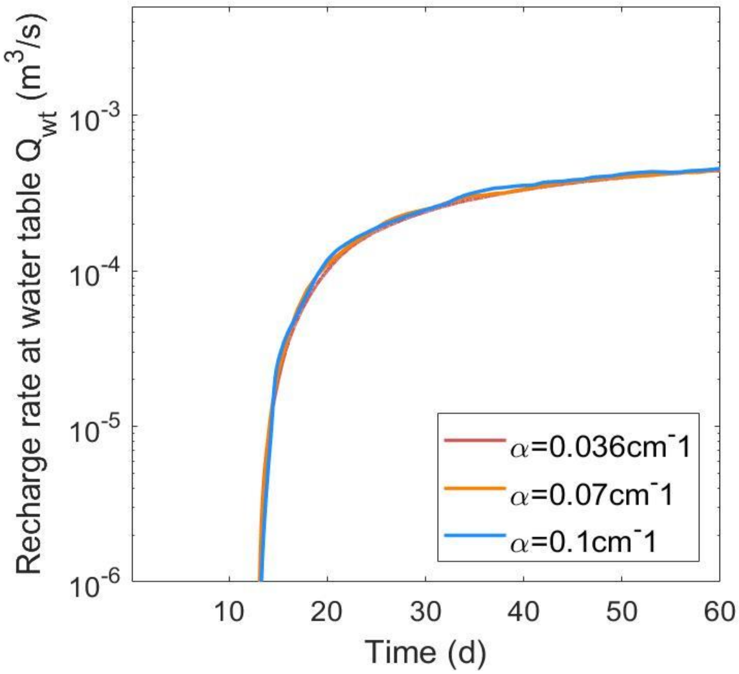

(a)

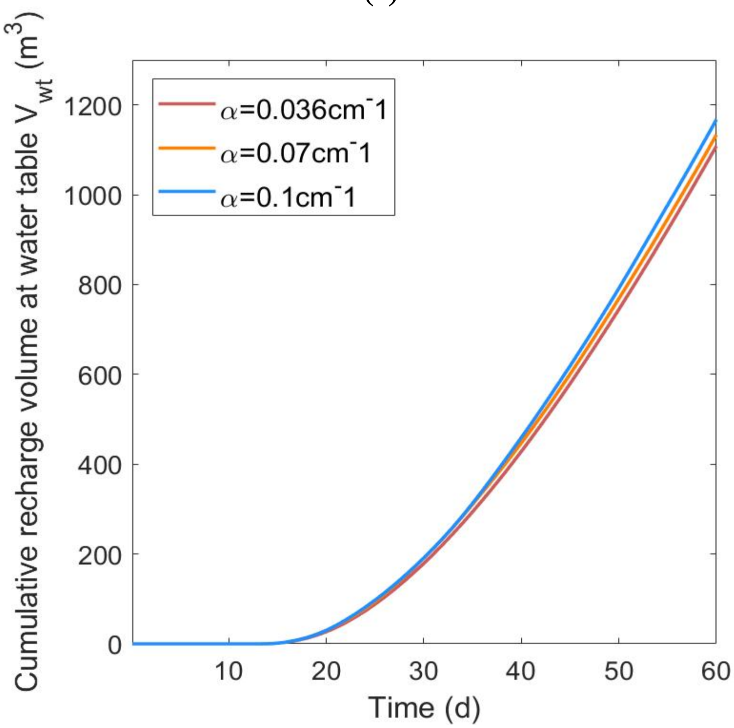

(b)

Figure 4-3 The recharge rate Q_{wt} and cumulative recharge volume V_{wt} at water table in the loam aquifer for different values of α with n = 1.56 and K_s = 24.96 cm/d: (a) Q_{wt} vs. t; (b) V_{wt} vs. t.

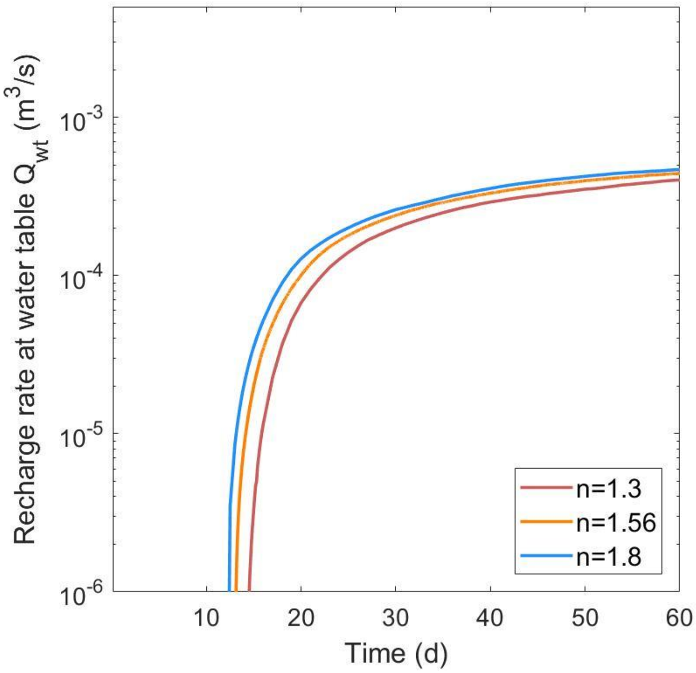

(a)

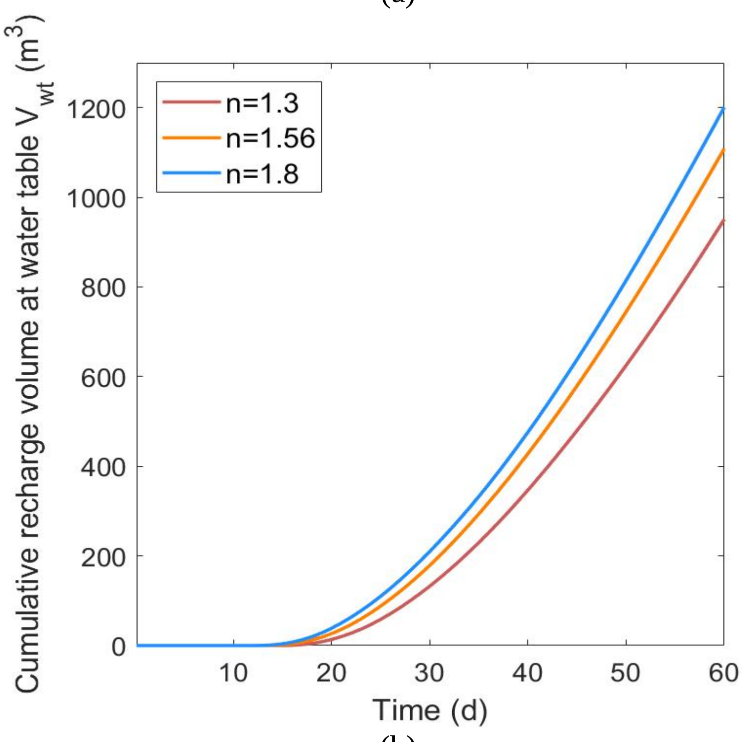

(b)

Figure 4-4 The recharge rate Q_{wt} and cumulative recharge volume V_{wt} at water table in the loam aquifer for different values of n with α = 0.036 cm^{-1} and K_s = 24.96 cm/d: (a) Q_{wt} vs. t; (b) V_{wt} vs. t.

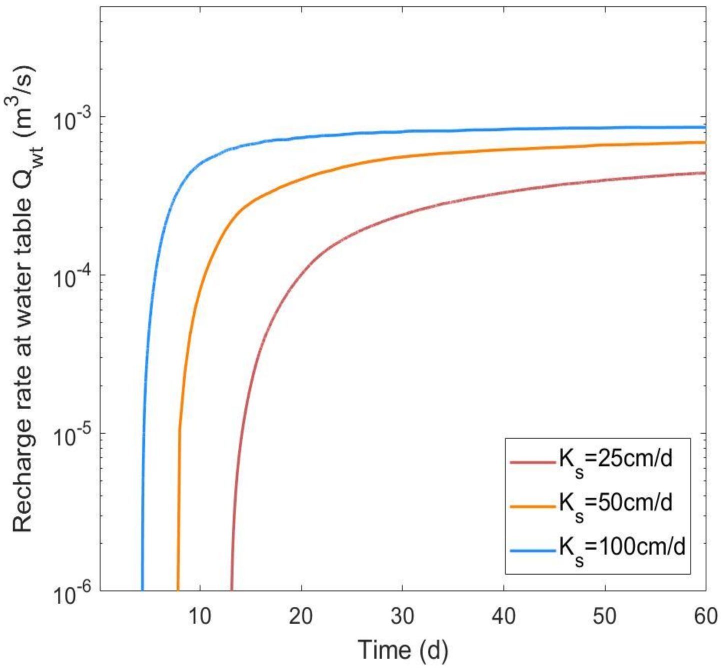

(a)

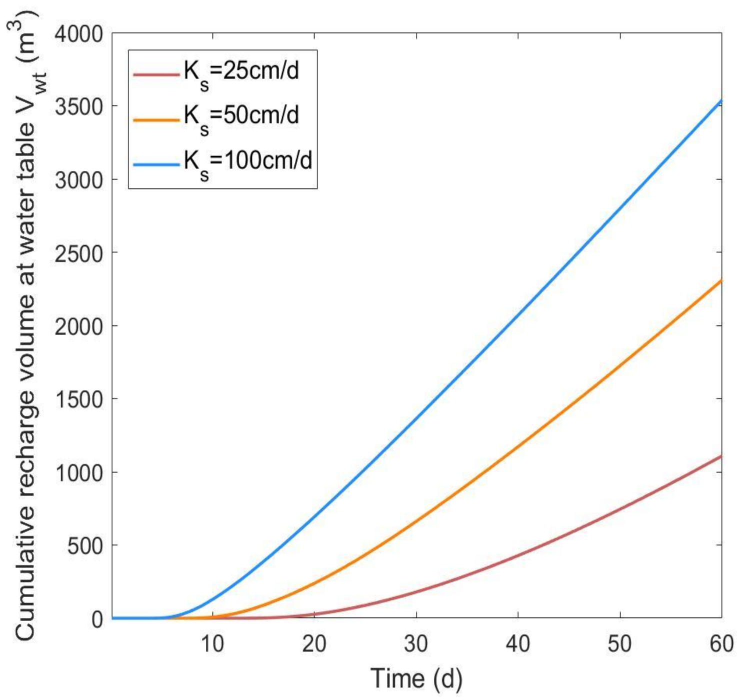

(b)

Figure 4-5 The recharge rate Q_{wt} and cumulative recharge volume V_{wt} at water table in the loam aquifer for different values of K_s with α = 0.036 cm^{-1} and n = 1.56: (a) Q_{wt} vs. t; (b) V_{wt} vs. t.

4.4.2 Subsurface heterogeneity control on recharge of VZW

The simulation results in the loam aquifer for depth of the clay loam layer $D_c = 10, 10.75$ and 11.5 m and $D_c = 13.5, 15.5$ and 17.5 m with $B_c = 0.5$ m are plotted in Figure 4-6 and Figure 4-8, respectively (D_c represents the depth of the top surface of the clay loam layer). The grey line represents the reference case in which water is injected by VZW into the homogeneous loam aquifer. In Figure 4-6, the clay loam layer is shallow and the well screen cuts through it. In Figure 4-8, the clay loam layer is deep and below the well screen.

The comparison with the reference case indicates that the presence of clay loam layer hinders the infiltration of injected water and reduces Q_{wt} and V_{wt}. When the well screen cuts through the clay loam layer, Figure 4-6 shows that Q_{wt} and V_{wt} decrease as D_c increases. In this situation, the well screen can be divided into three parts based on the location of the clay loam layer: an upper part which is above the clay loam layer, a lower part which is below the clay loam layer, and a middle part contacting the clay loam layer. The downward infiltration of water injected through the upper part of the well screen is hindered by the clay loam layer. The downward infiltration of water injected through the lower part of the well screen is not affected by the clay loam layer. As D_c increases, the upper part of the well screen becomes larger and the lower part of the well screen becomes smaller, thus the influences of the clay loam layer on recharge increases. Figure 4-7 demonstrates the profiles of change of pressure head in the aquifer. The change of pressure head is the difference between the calculated pressure head and the initial pressure head in the aquifer. Figures 4-7(a), (b) and (c) show the profiles for

VZW injection in a heterogeneous loam aquifer with D_c = 11.5 m and B_c = 0.5 m. Figures 4-7(d), (e) and (f) show the profiles for VZW injection in a homogeneous loam aquifer. Figure 4-7 shows that the water injected through the upper part of the screen tends to flow horizontally and its downward infiltration is slowed down by the clay loam layer. As the injected water flows horizontally, much water is absorbed by the aquifer medium and stored in the unsaturated zone, resulting in an increase in the pressure head and a decrease in the cumulative recharge volume. The change of pressure head is the highest around the screen and decreases with distance to the screen. When the well screen cuts through the clay loam layer, the areas with higher change of pressure head extend horizontally to a larger size compared to profiles of VZW injection in a homogeneous aquifer.

When the clay loam layer is deep and below the well screen, Figure 4-8 shows that its presence reduces Q_{wt} and V_{wt} and the change of D_c only has mild influences on recharge. In this scenario, the injection of water is not directly affected by the clay loam layer at the beginning. However, when the injected water reaches the clay loam layer, it will be slowed down because of the low-permeability nature of the clay loam layer. As D_c increases, the distances between the bottom of the clay loam layer and the water table decreases. Consequently, the total time required for the injected water to reach the water table decreases. Figure 4-9 demonstrates the profiles of change of pressure head in the aquifer. Figures 4-9(a), (b) and (c) show the profiles for VZW injection in heterogeneous loam aquifer with D_c = 15.5 m and B_c = 0.5 m. Figures 4-9(d), (e) and (f) show the profiles for VZW injection in a homogeneous loam aquifer. Figure 4-9 shows that as the injected water approaches the clay loam layer, part of water tends to flow horizontally and the infiltration radius increases, reducing Q_{wt} and V_{wt}. The change of pressure head gradually decreases with depth. Since the clay loam layer is deep, the infiltrated areas affected by the clay loam layer have lower change of pressure head than that when the well screen cuts through the clay loam layer. In this case, less water is absorbed by the unsaturated zone than that when the well screen cuts through the clay loam layer.

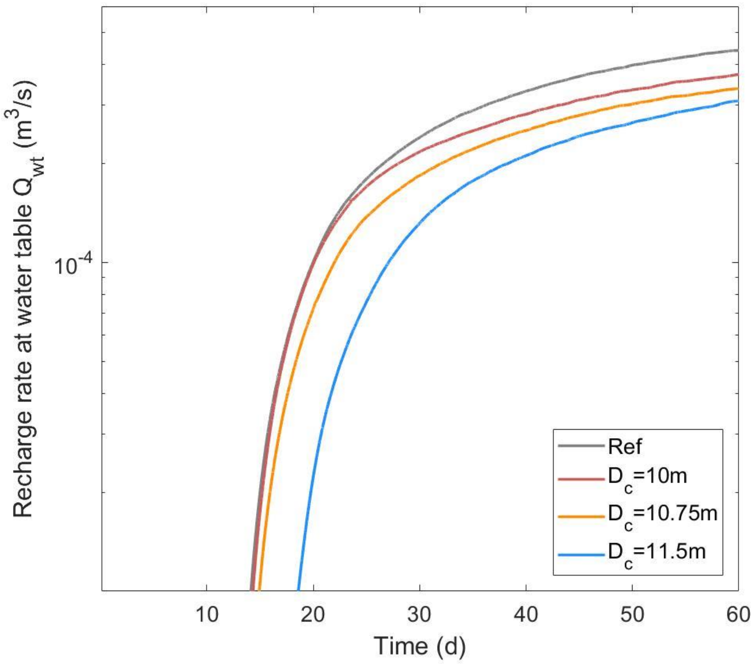

(a)

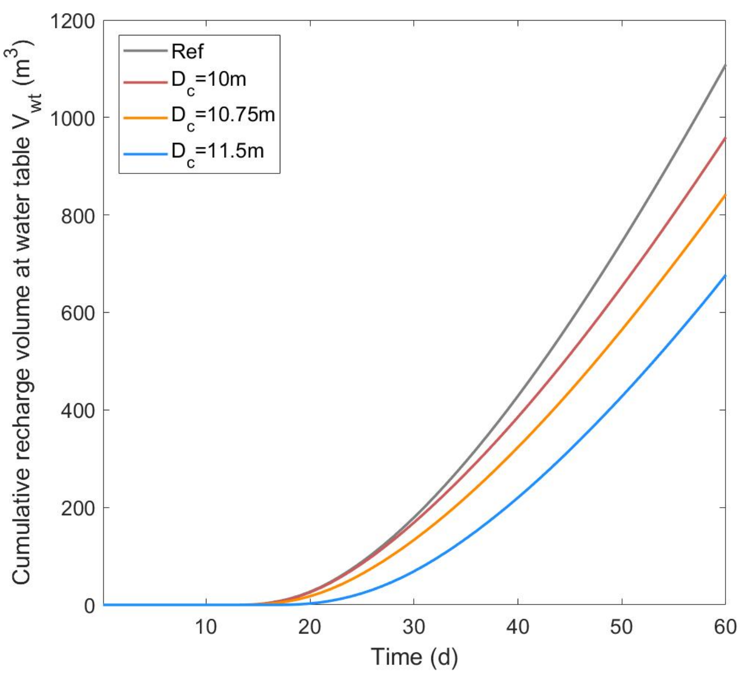

(b)

Figure 4-6 The recharge rate Q_{wt} and cumulative recharge volume V_{wt} at water table in the loam aquifer for different values of D_c when the well screen cuts through the clay loam layer (B_c = 0.5 m): (a) Q_{wt} vs. t; (b) V_{wt} vs. t.

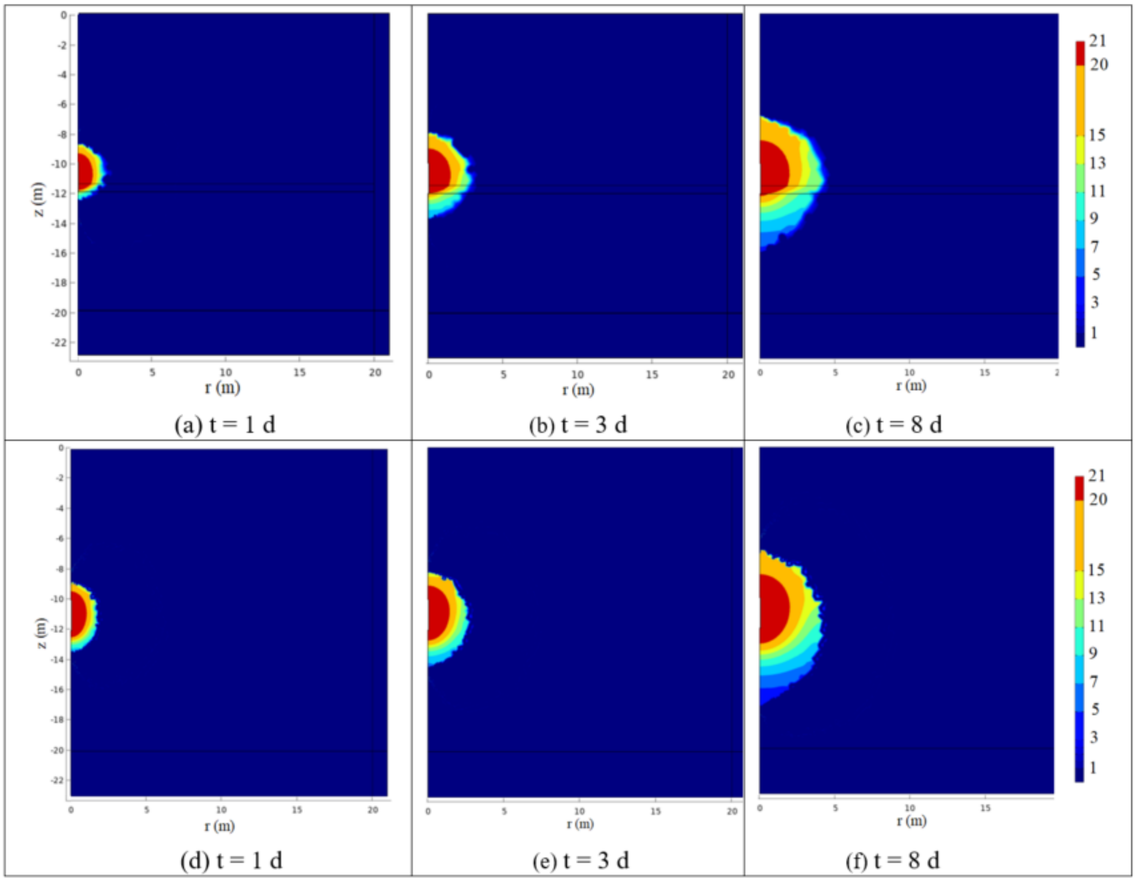

Figure 4-7 The profiles of change of pressure head in the aquifer: (a), (b) and (c) are profiles for VZW injection in heterogeneous loam aquifer (D_c = 11.5 m and B_c = 0.5 m) at $t = 1, 3$ and 8 d, respectively; (d), (e) and (f) are profiles for VZW injection in homogeneous loam aquifer at $t = 1, 3$ and 8 d, respectively.

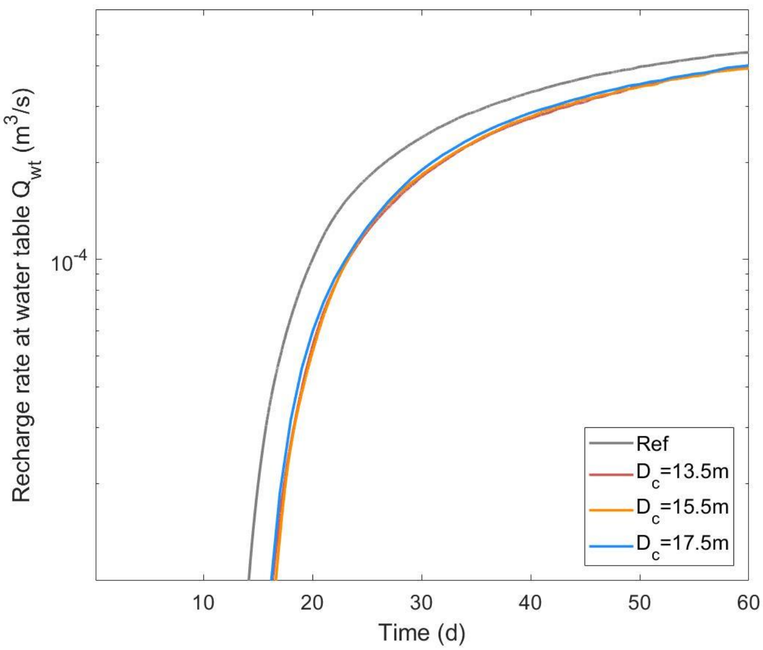

(a)

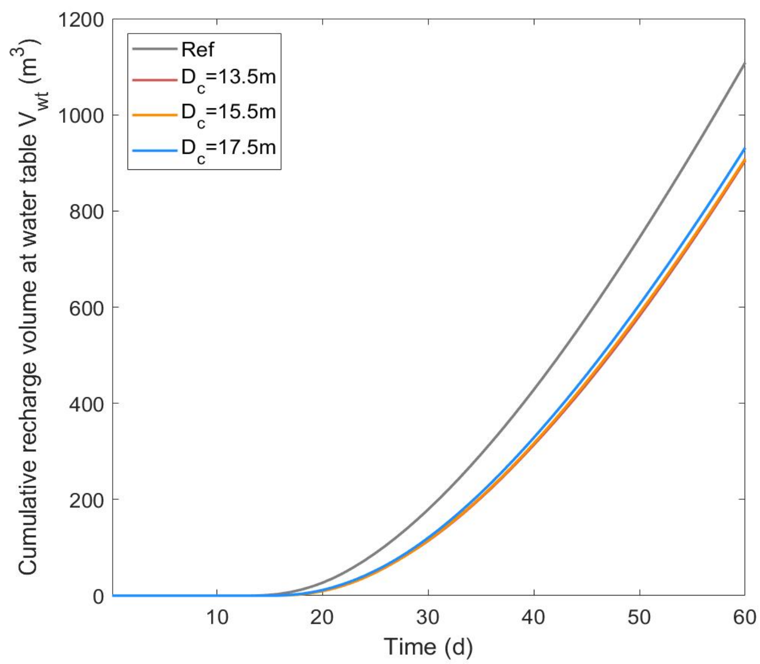

(b)

Figure 4-8 The recharge rate Q_{wt} and cumulative recharge volume V_{wt} at water table in the loam aquifer for different values of D_c when the clay loam layer lies below the well screen (B_c = 0.5 m): (a) Q_{wt} vs. t; (b) V_{wt} vs. t.

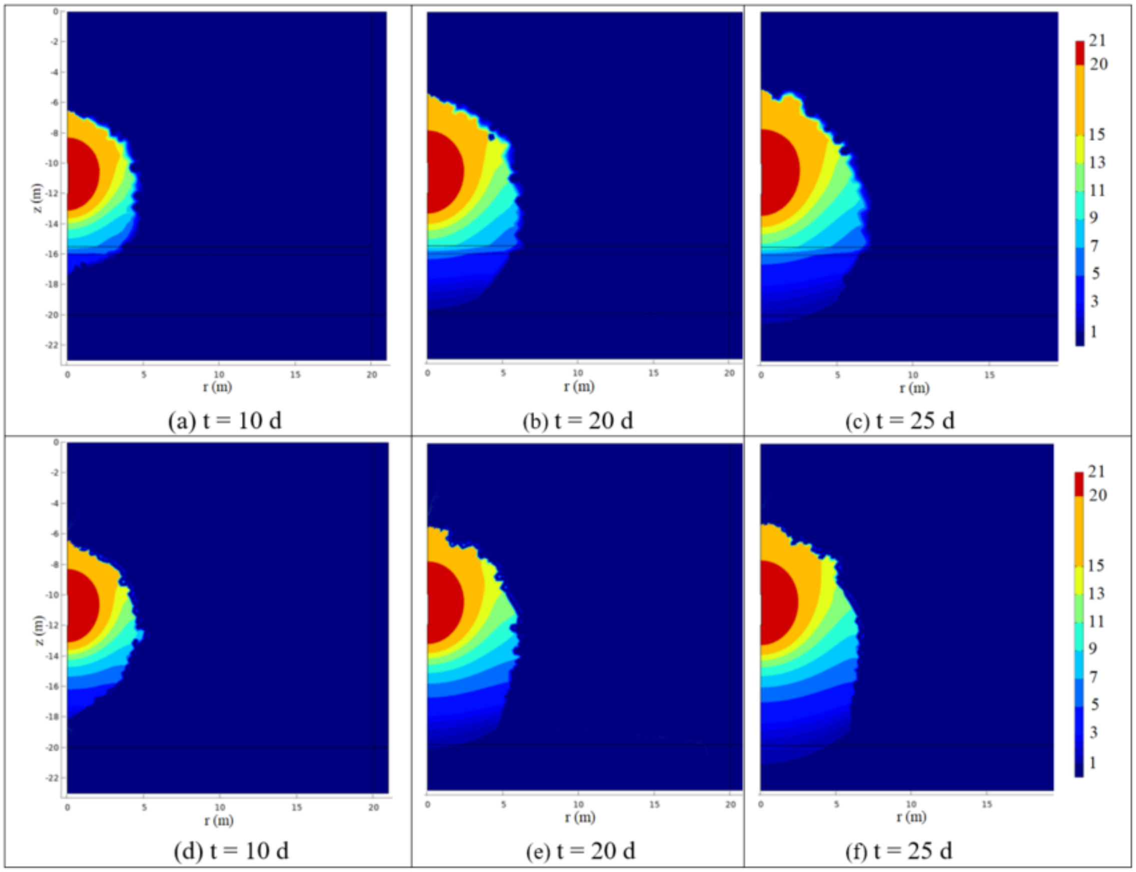

Figure 4-9 The profiles of change of pressure head in the aquifer: (a), (b) and (c) are profiles for VZW injection in heterogeneous loam aquifer (D_c = 15.5 m and B_c = 0.5 m) at $t = 10, 20$ and 25 d, respectively; (d), (e) and (f) are profiles for VZW injection in homogeneous loam aquifer at $t = 10, 20$ and 25 d, respectively.

The simulation results in the loam aquifer for lateral extension of the clay loam lens $R_c = 1, 3,$ and 5 m with $B_c =$ 0.5 m and $D_c = 10.75$ m are plotted in Figure 4-10. The simulation results in the loam aquifer for lateral extension of the clay loam lens $R_c = 1, 3,$ and 5 m with $B_c =$ 0.5 m and $D_c = 15.5$ m are plotted in Figure 4-11. The grey line represents the reference case in which water is injected by VZW into the homogeneous loam aquifer. Figure 4-10 shows that when $D_c = 10.75$ m, the increase of R_c can lead to slight decrease of Q_{wt} and V_{wt}. Figure 4-11 shows that when $D_c =$

15.5 m, the change of Q_{wt} and V_{wt} for $R_c = 1$ m are similar to that in the homogeneous aquifer. When R_c increases, the values of Q_{wt} decrease in the early stage of VZW injection and then reach to similar asymptotic values in the later stage. During VZW injection, the infiltration radius gradually increases with time. For small values of R_c, the infiltration radius will become larger than R_c after a certain period. After that time period, the downward infiltration of injected water is less affected by the low permeable lens since water can bypass it. As R_c increases, the area of the low permeable lens increases and it can lead to longer t_a and smaller V_{wt}. When the well screen cuts through the low permeable lens, the infiltration area with higher water content extends horizontally to a larger size, causing more water to be absorbed by the unsaturated zone, and less water to infiltrate downward to reach the saturated zone. When the clay loam layer is below the well screen, the infiltration area with relatively low water content extends horizontally. The water being absorbed by the unsaturated zone in this condition is less than that when the well screen cuts through the low permeable lens.

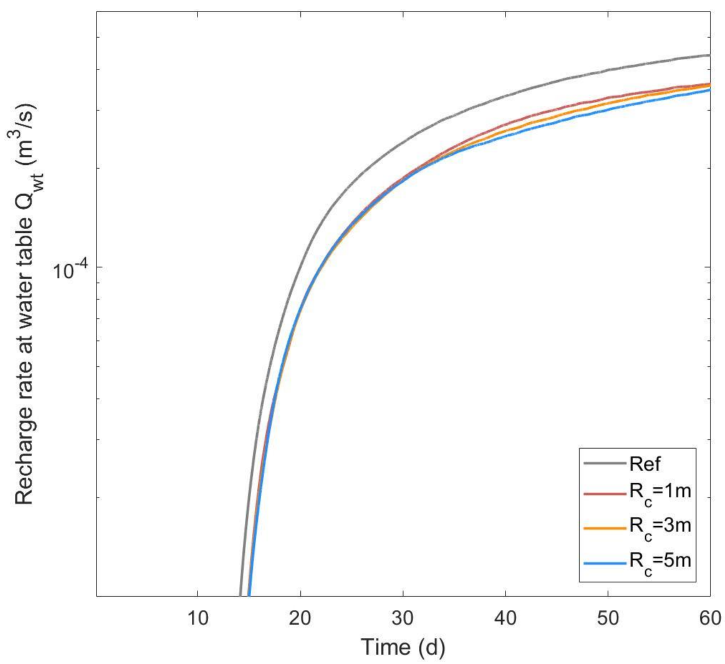

(a)

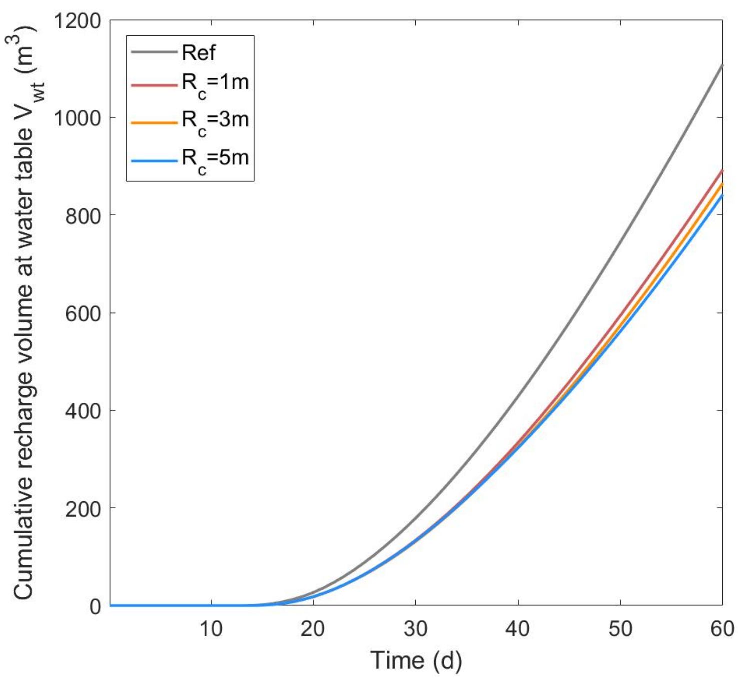

(b)

Figure 4-10 The recharge rate Q_{wt} and cumulative recharge volume V_{wt} at water table in the loam aquifer for different values of R_c with B_c = 0.5 m and D_c = 10.75 m: (a) Q_{wt} vs. t; (b) V_{wt} vs. t.

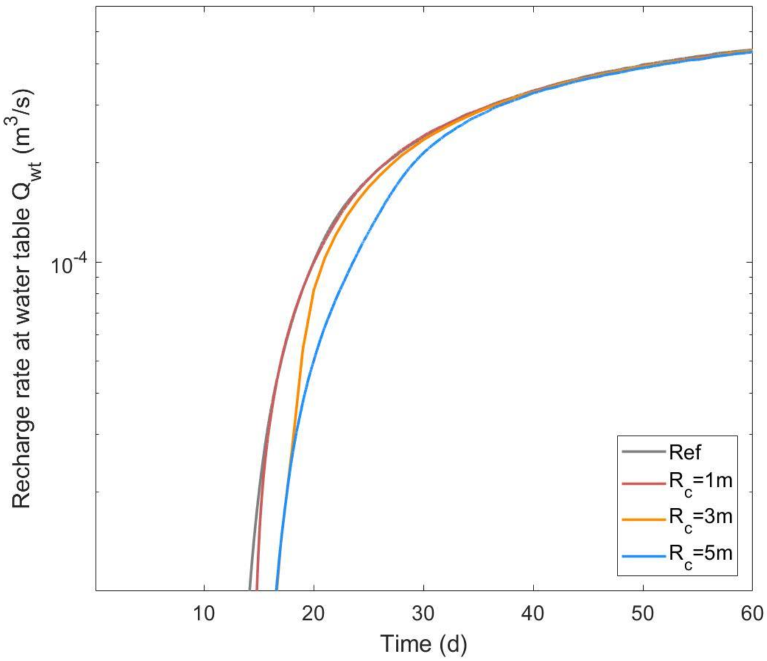

(a)

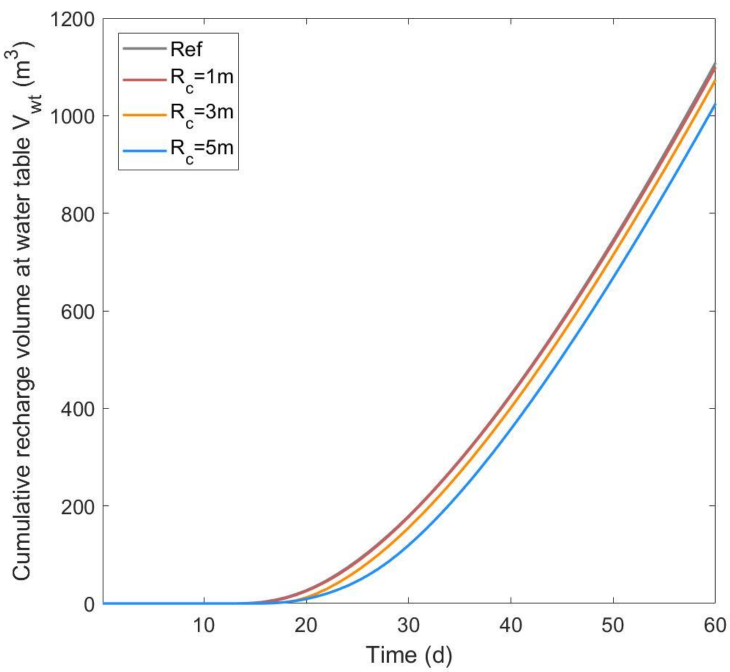

(b)

Figure 4-11 The recharge rate Q_{wt} and cumulative recharge volume V_{wt} at water table in the loam aquifer for different values of R_c with B_c = 0.5 m and D_c = 15.5 m: (a) Q_{wt} vs. t; (b) V_{wt} vs. t.

The simulation results in the loam aquifer for hydraulic conductance of the clay loam layer $\frac{K_s}{B_c} = 0.062, 0.312,$ and 0.1248 d^{-1} are plotted in Figure 4-8. Figures 4-8a and 4-8b show cases in which the clay loam layer has depth $D_c = 10.75$ m and Figures 4-8c and 4-8d show cases in which the clay loam layer has depth $D_c = 15.5$ m. The thickness B_c and hydraulic conductivity K_s are both important parameters that affect the flow of water in the porous media, and they are often combined into a single parameter hydraulic conductance $\frac{K_s}{B_c}$ to be applied in field projects (Bear, 2013). In the numerical tests, we investigate the influences of B_c and K_s on the recharge of VZW and the feasibility of using hydraulic conductance $\frac{K_s}{B_c}$ to describe the effects of low permeable layer on the recharge of VZW. In Figure 4-8, the grey line represents the reference case in which water is injected by VZW into the homogeneous loam aquifer. The solid lines represent cases in which B_c changes from 0.2 m to 1 m and K_s stays the same as 6.24 cm/d. The dashed lines represent cases in which B_c stays the same as 0.5 m and K_s changes for different values. The solid and dashed lines with the same color have the same value of $\frac{K_s}{B_c}$. Figures 4-8a and 4-8b indicate that when the well screen cuts through the clay loam layer, the change of B_c have a greater impact on water recharge than K_s. When B_c increases, water injected above the low permeable layer has to infiltrate through the thicker layer at a smaller rate, leading to decrease of recharge and increase of water absorbed by the vadose zone. Figures 4-8c and 4-8d indicate that when the clay loam layer is below the well screen, the increase of B_c or the decrease of K_s can lead to decrease of Q_{wt} and V_{wt}. And their influences on the recharge of VZW are similar when the value of $\frac{K_s}{B_c}$ is the same. In this situation, the hydraulic conductance $\frac{K_s}{B_c}$ can be used to describe the effects of low permeable layer on the recharge of VZW.

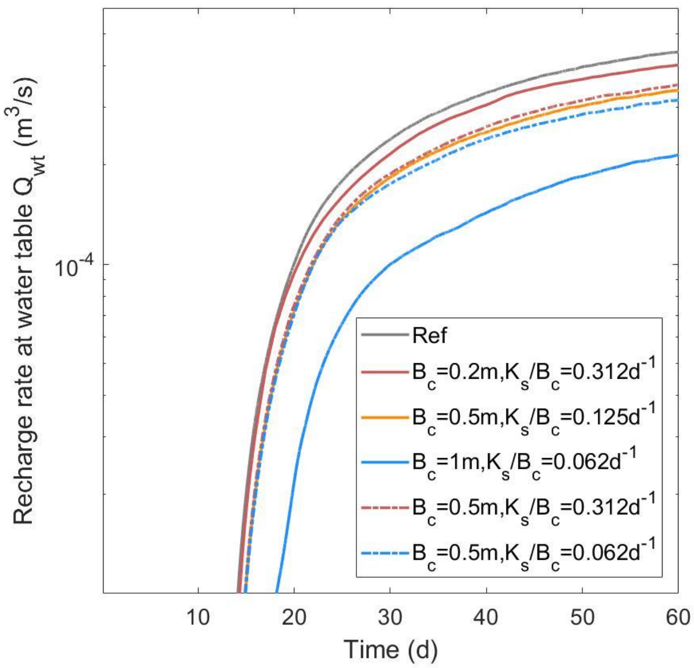

(a)

Figure 4-12 The recharge rate Q_{wt} and cumulative recharge volume V_{wt} at water table in the loam aquifer for different values of K_s/B_c: (a) Q_{wt} vs. t with D_c = 10.75 m; (b) V_{wt} vs. t with D_c = 10.75 m; (c) Q_{wt} vs. t with D_c = 15.5 m; (d) V_{wt} vs. t with D_c = 15.5 m.

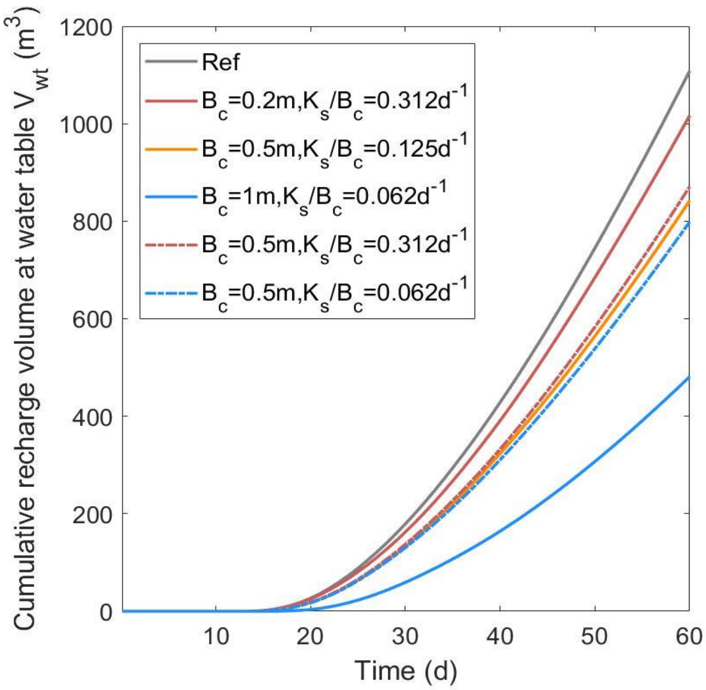

(b)

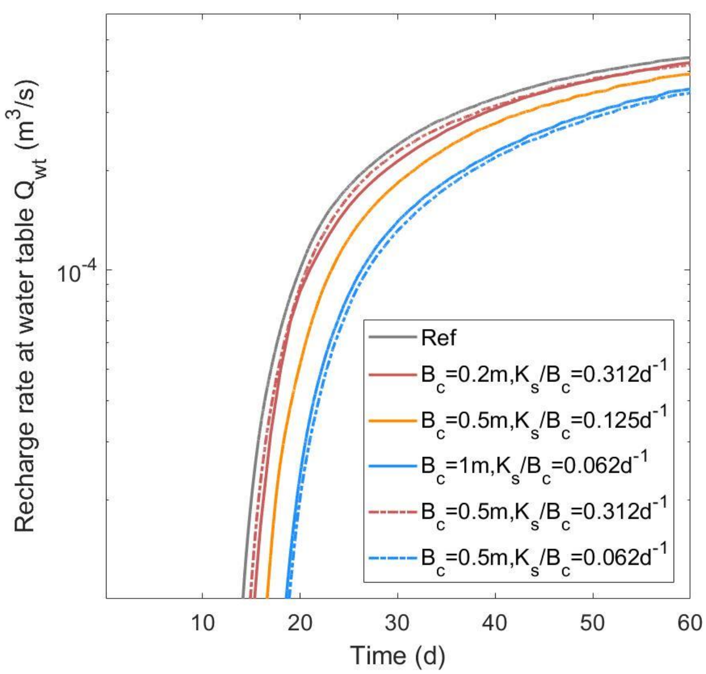

(c)

Figure 4-12 Continued.

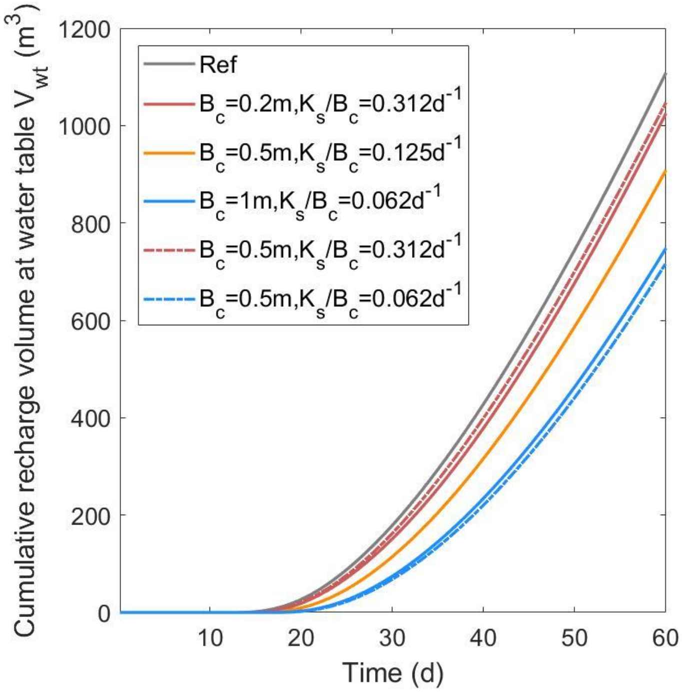

(d)

Figure 4-12 Continued.

4.5 Discussion

There are some issues about assumptions and limitations of this study that deserve further discussion.

Firstly, the preferential flow is not considered in this study. The preferential flow refers to that water movement and solute transport occur through a small fraction of the medium along preferential paths (Nimmo and Likens, 2009). The common types of preferential flow include (1) macropore flow, through pores distinguished from other pores by their larger size, greater continuity, or other attributes that can enhance flow; (2) funnel flow, caused by flow-impeding features of the medium that concentrate flow in adjacent zones that are highly wetted and conductive; and (3) finger flow, which concentrates flow in wet, conductive fingers (Nimmo and Likens, 2009; Zhang et al., 2016). The presence of preferential flow in VZW injection can shorten the residence time of water in the vadose zone and complicate the recharge model. Further studies are needed to investigate the influences of preferential flow on the recharge of VZW.

Secondly, there are limited published studies on experiments of VZW injection. Many difficulties exist in experimental studies of VZW injection. For example, the fluid flow can cause the particles in the column test to rearrange and change the hydraulic properties of the porous media. More research is still in need to improve the experimental setup for VZW injection. And numerical model is a good method to learn about the recharge of VZW and guide the design of well tests. Difficulties also lie in the development of numerical model of VZW injection. Because of the nonlinearity of Richards' equation, it may take more than 20 hours in a Dell Precision workstation (Processor: Intel Core i7-10700) to solve the model. Therefore, the setting of dimension and time step of numerical model should be carefully considered on the basis of accuracy and feasibility.

4.6 Conclusion

The conclusions of this study are summarized as follows:

1. Subsurface heterogeneity has large influences on groundwater recharge of VZW. The presence of the low permeable layer in the aquifer hinders the infiltration of injected water and reduces Q_{wt} and V_{wt}. And its influences depend on depth D_c, lateral extension R_c, thickness B_c and hydraulic conductivity K_s of the low permeable layer.

2. When R_c, B_c and K_s remain the same, the influences of D_c on the recharge of VZW have two forms. When the well screen cuts through the low permeable layer, Q_{wt} and V_{wt} decrease a lot as D_c increases. When the low permeable layer is below the well screen, the change of D_c only has slightly influences on recharge. Besides, when the low permeable layer is cut through by the bottom of the well screen, its impacts on water recharge are greater than that when the low permeable layer lies below the well screen.
3. When D_c, B_c and K_s remain the same, the influences of R_c on the recharge of VZW have two different characteristics as well. When the well screen cuts through the low permeable lens, the increase of R_c can lead to slightly decrease of Q_{wt} and V_{wt} and this effect is more obvious in the later stage of VZW injection. When the low permeable lens is below the well screen, the increase of R_c makes Q_{wt} decrease in the early stage of VZW injection and then Q_{wt} for different values of R_c reach to similar asymptotic values in the later stage. In addition, when the well screen cuts through the low permeable lens, the impacts on water recharge are greater than that when the low permeable lens lies below the well screen.
4. When D_c and R_c remain the same, the influences of B_c and K_s on the recharge of VZW have two distinctive forms. When the well screen cuts through the low permeable layer, the change of B_c have a greater impact on water recharge than K_s and the hydraulic conductance $\frac{K_s}{B_c}$ cannot be used to describe the combined impacts of B_c and K_s. When the low permeable layer is below the well screen, the cases with the

same value of $\frac{K_s}{B_c}$ have similar changes of Q_{wt} and V_{wt} and the hydraulic conductance $\frac{K_s}{B_c}$ can be used to describe the effects of low permeable layer on the recharge of VZW.

CHAPTER 5

CONCLUSIONS AND FUTURE WORK

To improve the understanding of VZW injection performance, three studies are conducted to investigate the influences of time-dependent GSF generated by infiltration or evapotranspiration on the VZW injection, the geometric and soil properties control on the recharge of VZW, and the subsurface heterogeneity control on the recharge of VZW. The conclusions of three studies are summarized in the following section and the future works are also discussed.

5.1 Conclusions of three studies on VZW injection

To investigate the influences of time-dependent GSF generated by infiltration or evapotranspiration, the semi-analytical solutions for the hydraulic head increment and infiltration rate at the interface of the unsaturated and saturated zones are derived by applying the Laplace and Hankel transforms to the coupled unsaturated-saturated governing equations. The unsaturated flow is described by a linearized Richards' equation and the saturated flow is described by a three-dimensional groundwater flow equation. The unsaturated and saturated flows are coupled by interface conditions representing continuity of pressure and normal flux across the water table. The time-domain solutions are obtained by using the de Hoog algorithm and they are tested by comparing with the numerical simulation results solved by COMSOL Multiphysics. The analysis of results indicates that the presence of GSF generated by infiltration can increase the hydraulic head increments in the unsaturated and saturated zones and the recharge rate at the water table. The presence of GSF generated by evapotranspiration plays the opposite effects on VZW injection and it can decrease the hydraulic head increments in the unsaturated and saturated zones The magnitude of the influence of GSF on VZW depends on properties of unsaturated and saturated zones and the value of GSF.

The geometric and soil property control on the recharge of VZW is investigated by developing a finite-element numerical model in COMSOL Multiphysics. Different injection plans including injection rates and injection durations are also assessed for the sake of optimizing the application of VZWs. The flow induced by VZW injection is described by the Richards' equation and the VGM model is used to describe the water retention and relative hydraulic conductivity of the unsaturated zone. The simulation results indicate that the soil properties of the aquifer have great influences on the recharge of VZW and coarser soils are beneficial to the flow of injected water. The well geometric properties have relatively large impacts on the performance of VZW injection and the impacts are reflected mainly in affecting the travel distance of injected water. The arrangement of injection plan given a constant total volume of injected water has a great influence on the performance of VZW injection. The application of a higher injection rate at early times can shorten the arrival time and improve the recharge of VZW.

The subsurface heterogeneity control on the recharge of VZW is investigated by developing a finite-element numerical model in COMSOL Multiphysics. The flow induced by VZW injection is described by the Richards' equation and the VGM model is used to describe the water retention and relative hydraulic conductivity of the unsaturated zone. The subsurface heterogeneity is considered as the presence of a low permeable layer or lens in the unsaturated zone. Several numerical experiments are conducted to evaluate the influences of subsurface heterogeneity on the recharge of VZW. The simulation results indicate that subsurface heterogeneity has large influences on groundwater recharge of VZW and the presence of the low permeable layer in the aquifer hinders the infiltration of injected water. The influences of the low permeable layer on recharge of VZW depend on depth, lateral extension, thickness and hydraulic conductance of the low permeable layer. The influences of the low permeable layer on recharge of VZW also depend on the position of the low permeable layer relative to the well screen.

5.2 Future works

As discussed in previous chapters, clogging is one of the obstacles that hinders the application and ongoing development of MAR. Bloetscher et al. (2014) reviewed 204 aquifer storage and recovery sites in the United States and examined the reasons for the terminated projects. They found that different degrees and types of clogging were encountered by 37% of these sites and clogging problems led to termination of 27% of the sites. Clogging generally occurs at the interface between MAR facilities and the aquifer, and it involves four types process: physical clogging associated with the accumulation of suspended solids; biological clogging including the growth and accumulation of bacteria and algae; chemical clogging involving precipitation of elements; and mechanical clogging such as entrained air or gas binding (Glass et al., 2020; Martin, 2013). To evaluate clogging during MAR operation, some analytical models have been proposed. Bianchi et al. (1978) developed an exponentially reduced permeability model to reflect the clogging effect on aquifer permeability:

$$K(t) = K_\infty + (K_0 - K_\infty)^{-\lambda t} \tag{5.1}$$

where K_0 and K_∞ denote the initial and asymptotic hydraulic conductivity, respectively $[\mathrm{LT}^{-1}]$; λ is the permeability reduction rate $[\mathrm{T}^{-1}]$. The applicability of Eq. (5.1) has been supported in laboratory testing and numerical modeling (Chu et al., 2019; Reddi et al., 2000; Reddi et al., 2005; Zheng et al., 2014). This model has been widely used in developing clogging-related analytical or semi-analytical solutions for artificial recharge. For instance, Li et al. (2020) considered exponentially decayed model of Bianchi et al. (1978) and developed analytical solutions for aquifer recharge using partially penetrating wells in confined aquifers based on analysis of in-situ observation data.

At present, the analytical or semi-analytical solutions for VZW injection considering clogging is still lacking. One direction for the next step of our research is to include the exponentially decayed model of Bianchi et al. (1978) in the coupled unsaturated-saturated equations for VZW injection and to develop the mathematical model for VZW injection with clogging-induced permeability reduction.

Besides, many laboratory experiments and numerical models have been proposed to investigate the clogging process during MAR. Chu et al. (2019) conducted a 1D laboratory column experiment to simulate recharge by surface infiltration basin and developed a numerical transient model coupled with experimental monitoring data to simulate the evolution of the permeability affected by suspended solids clogging. They found that clogging led to reduction of the hydraulic conductivity in the upper layer which extended to a depth of approximately 50 cm during the experimental period of 129 hr and the clogging rates decreased with the depth. Glass et al. (2020) conducted two laboratory experiments representing recharge from infiltration basins and injection wells, respectively, and corresponding numerical models were developed by HYDRUS-2D to describe the implementation and validation of a simplified representation of clogging into the variably saturated flow model. They focused only on the infiltration process in MAR systems and their simulation results showed the successful implementation of using a time-dependent scaling factor decreasing exponentially with time to represent hydraulic conductivity changes over time.

For VZW, such variably saturated flow model considering clogging is still lacking. The other research that we are going to conduct is to develop a variably saturated flow model for VZW by COMSOL Multiphysics and include effects of clogging as time-variable hydraulic conductivities to investigate the influences of clogging on the recharge of VZW. We believe that these studies will be innovative contributions to MAR by improving the knowledge of the recharge of VZW and will be valuable to serve as guidance for VZW design and management.

REFERENCES

Bear, J., 2013. Dynamics of fluids in porous media. Courier Corporation.

Beven, K., 1979. A sensitivity analysis of the Penman-Monteith actual evapotranspiration estimates. Journal of Hydrology, 44(3-4): 169-190.

Bianchi, W.C., Nightingale, H.I., McCormick, R.L., 1978. A case history to evaluate the performance of water-spreading projects. Journal (American Water Works Association): 176-180.

Bloetscher, F., Sham, C.H., Danko III, J.J., Ratick, S., 2014. Lessons learned from aquifer storage and recovery (ASR) systems in the United States. Journal of Water Resource and Protection, 6(17): 1603.

Bouwer, H., 2002. Artificial recharge of groundwater: hydrogeology and engineering. Hydrogeology Journal, 10(1): 121-142.

Bouwer, H. et al., 2008. Design, operation and maintenance for sustainable underground storage facilities. Report, American Water Works Association Research Foundation, Denver, CO.

Bouwer, H., Rice, R., 1976. A slug test for determining hydraulic conductivity of unconfined aquifers with completely or partially penetrating wells. Water resources research, 12(3): 423-428.

Carsel, R.F., Parrish, R.S., 1988. Developing joint probability distributions of soil water retention characteristics. Water resources research, 24(5): 755-769.

Chang, C.-H., Huang, C.-S., Yeh, H.-D., 2018. Analysis of three-dimensional unsaturated–saturated flow induced by localized recharge in unconfined aquifers. Hydrology and Earth System Sciences, 22(7): 3951-3963.

Chu, S.T., 1978. Infiltration during an unsteady rain. Water Resources Research, 14(3): 461-466.

Chu, T., Yang, Y., Lu, Y., Du, X., Ye, X., 2019. Clogging process by suspended solids during groundwater artificial recharge: Evidence from lab simulations and numerical modelling. Hydrological Processes, 33(25): 3226-3235.

Dagan, G., 1967. A method of determining the permeability and effective porosity of unconfined anisotropie aquifers. Water Resources Research, 3(4): 1059-1071.

De Hoog, F.R., Knight, J., Stokes, A., 1982. An improved method for numerical inversion of Laplace transforms. SIAM Journal on Scientific and Statistical Computing, 3(3): 357-366.

DehghaniSanij, H., Yamamoto, T., Rasiah, V., 2004. Assessment of evapotranspiration estimation models for use in semi-arid environments. Agricultural water management, 64(2): 91-106.

Dillon, P., 2005. Future management of aquifer recharge. Hydrogeology journal, 13(1): 313-316.

Dillon, P. et al., 2010. Managed aquifer recharge: rediscovering nature as a leading edge technology. Water science and technology, 62(10): 2338-2345.

Edwards, E.C., Harter, T., Fogg, G.E., Washburn, B., Hamad, H., 2016. Assessing the effectiveness of drywells as tools for stormwater management and aquifer recharge and their groundwater contamination potential. Journal of Hydrology, 539: 539-553.

Farthing, M.W., Ogden, F.L., 2017. Numerical solution of Richards' equation: A review of advances and challenges. Soil Science Society of America Journal, 81(6): 1257-1269.

Gao, Y., Pu, S., Zheng, C., Yi, S., 2019. An improved method for the calculation of unsaturated–saturated water flow by coupling the FEM and FDM. Scientific reports, 9(1): 1-9.

García-Menéndez, O. et al., 2018. Using electrical resistivity tomography to assess the effectiveness of managed aquifer recharge in a salinized coastal aquifer. Environmental monitoring and assessment, 190(2): 100.

Gardner, W., 1958. Some steady-state solutions of the unsaturated moisture flow equation with application to evaporation from a water table. Soil science, 85(4): 228-232.

Ghayoumian, J., Saravi, M.M., Feiznia, S., Nouri, B., Malekian, A., 2007. Application of GIS techniques to determine areas most suitable for artificial groundwater recharge in a coastal aquifer in southern Iran. Journal of Asian Earth Sciences, 30(2): 364-374.

Glass, J., Šimůnek, J., Stefan, C., 2020. Scaling factors in HYDRUS to simulate a reduction in hydraulic conductivity during infiltration from recharge wells and infiltration basins. Vadose Zone Journal, 19(1): e20027.

Glover, R., 1953. Flow from a test-hole located above groundwater level. Theory and Problems of Water Percolation, 8: 69-71.

Gude, V.G., 2017. Desalination and water reuse to address global water scarcity. Reviews in Environmental Science and Bio/Technology, 16(4): 591-609.

Guo, W., Coulibaly, K., Maliva, R.G., 2015. Simulated effects of aquifer heterogeneity on ASR system performance. Environmental Earth Sciences, 73(12): 7803-7809.

Händel, F., Liu, G., Dietrich, P., Liedl, R., Butler Jr, J.J., 2014. Numerical assessment of ASR recharge using small-diameter wells and surface basins. Journal of hydrology, 517: 54-63.

Händel, F. et al., 2016. Assessment of small-diameter shallow wells for managed aquifer recharge at a site in southern Styria, Austria. Hydrogeology Journal, 24(8): 2079-2091.

Hanson, R., Nishikawa, T., 1996. Combined use of flowmeter and time - drawdown data to estimate hydraulic conductivities in layered aquifer systems. Groundwater, 34(1): 84-94.

Hao, Q., Shao, J., Cui, Y., Xie, Z., 2014. Applicability of artificial recharge of groundwater in the Yongding River alluvial fan in Beijing through numerical simulation. Journal of Earth Science, 25(3): 575-586.

Holloway, O.G., Waddell, J.P., 2008. Design and Operation of a Borehole Straddle Packer for Ground-Water Sampling and Hydraulic Testing of Discrete Intervals at US Air Force Plant 6, Marietta, Georgia. 2331-1258, US Geological Survey.

Jansen, H., Stenstrom, M., De Koning, J., 2007. Development of indirect potable reuse in impacted areas of the United States. Water science and technology, 55(1-2): 357-366.

Jeong, H.Y., Jun, S.-C., Cheon, J.-Y., Park, M., 2018. A review on clogging mechanisms and managements in aquifer storage and recovery (ASR) applications. Geosciences Journal, 22(4): 667-679.

Jokela, P., Kallio, E., 2015. Sprinkling and well infiltration in managed aquifer recharge for drinking water quality improvement in Finland. Journal of Hydrologic Engineering, 20(3): B4014002.

Kargas, G., Kerkides, P., Poulovassilis, A., 2012. Infiltration of rain water in semi-arid areas under three land surface treatments. Soil and Tillage Research, 120: 15-24.

Karlsen, R.H., Smits, F., Stuyfzand, P., Olsthoorn, T., Van Breukelen, B., 2012. A post audit and inverse modeling in reactive transport: 50 years of artificial recharge in the Amsterdam Water Supply Dunes. Journal of Hydrology, 454: 7-25.

Kim, J., Warnock, A., Ivanov, V.Y., Katopodes, N.D., 2012. Coupled modeling of hydrologic and hydrodynamic processes including overland and channel flow. Advances in Water Resources, 37: 104-126.

Kroszynski, U.I., Dagan, G., 1975. Well pumping in unconfined aquifers: The influence of the unsaturated zone. Water Resources Research, 11(3): 479-490.

Kuster, M., Díaz-Cruz, S., Rosell, M., de Alda, M.L., Barceló, D., 2010. Fate of selected pesticides, estrogens, progestogens and volatile organic compounds during artificial aquifer recharge using surface waters. Chemosphere, 79(8): 880-886.

Lacher, L., Turner, D., Gungle, B., Bushman, B., Richter, H., 2014. Application of hydrologic tools and monitoring to support managed aquifer recharge decision making in the upper San Pedro River, Arizona, USA. Water, 6(11): 3495-3527.

Li, J., Chen, J.-J., Zhan, H., Li, M.-G., Xia, X.-H., 2020. Aquifer recharge using a partially penetrating well with clogging-induced permeability reduction. Journal of Hydrology, 590: 125391.

Liang, X., Zhan, H., You-Kuan, Z., Liu, J., 2017a. On the coupled unsaturated-saturated flow process induced by vertical, horizontal, and slant wells in unconfined aquifers. Hydrology and Earth System Sciences, 21(2): 1251.

Liang, X., Zhan, H., Zhang, Y.K., 2018. Aquifer Recharge Using a Vadose Zone Infiltration Well. Water Resources Research, 54(11): 8847-8863.

Liang, X., Zhan, H., Zhang, Y.K., Schilling, K., 2017b. Base flow recession from unsaturated - saturated porous media considering lateral unsaturated discharge and aquifer compressibility. Water Resources Research, 53(9): 7832-7852.

Lin, Y.-C., Li, M.-H., Yeh, H.-D., 2017. An analytical model for flow induced by a constant-head pumping in a leaky unconfined aquifer system with considering unsaturated flow. Advances in Water Resources, 107: 525-534.

Liu, G. et al., 2016. Field Investigation of a New Recharge Approach for ASR Projects in Near - Surface Aquifers. Groundwater, 54(3): 425-433.

Liu, H.-L., Bao, A.-M., Pan, X.-L., Chen, X., 2013. Effect of land-use change and artificial recharge on the groundwater in an arid inland river basin. Water resources management, 27(10): 3775-3790.

Liu, J. et al., 2017. Water scarcity assessments in the past, present, and future. Earth's future, 5(6): 545-559.

Lluria, M., 2009. Successful application of managed aquifer recharge in the improvement of the water resources management of semi-arid regions: Examples from Arizona and the Southwestern USA. Boletín geológico y minero, 120(2): 111-120.

Maples, S.R., Fogg, G.E., Maxwell, R.M., 2019. Modeling managed aquifer recharge processes in a highly heterogeneous, semi-confined aquifer system. Hydrogeology Journal, 27(8): 2869-2888.

Martin, R., 2013. Clogging issues associated with managed aquifer recharge methods. IAH Commission on Managing Aquifer Recharge.

Mathias, S., Butler, A., 2006. Linearized Richards' equation approach to pumping test analysis in compressible aquifers. Water resources research, 42(6).

Mishra, P.K., Neuman, S.P., 2010. Improved forward and inverse analyses of saturated - unsaturated flow toward a well in a compressible unconfined aquifer. Water Resources Research, 46(7).

Mishra, P.K., Vesselinov, V.V., Kuhlman, K.L., 2012. Saturated–unsaturated flow in a compressible leaky-unconfined aquifer. Advances in water resources, 42: 62-70.

Mualem, Y., 1976. A new model for predicting the hydraulic conductivity of unsaturated porous media. Water resources research, 12(3): 513-522.

Nimmo, J., Likens, G., 2009. Vadose water.

Ogata, H., 2005. A numerical integration formula based on the Bessel functions. Publications of the Research Institute for Mathematical Sciences, 41(4): 949-970.

Patil, M. et al., 2019. Assessment of rainfall recharge using rainfall infiltration factor method and empirical equations. Discovery Nature, 13: 1-8.

Philip, J.R., 1969. Theory of infiltration, Advances in hydroscience. Elsevier, pp. 215-296.

Qi, C., Zhan, H., Liang, X., Ma, C., 2020. Influence of time-dependent ground surface flux on aquifer recharge with a vadose zone injection well. Journal of Hydrology, 584: 124739.

Qi, T. et al., 2021. Water Distribution from Artificial Recharge via Infiltration Basin under Constant Head Conditions. Water, 13(8): 1052.

Rahman, M.A., Rusteberg, B., Gogu, R., Ferreira, J.L., Sauter, M., 2012. A new spatial multi-criteria decision support tool for site selection for implementation of managed aquifer recharge. Journal of environmental management, 99: 61-75.

Reddi, L.N., Ming, X., Hajra, M.G., Lee, I.M., 2000. Permeability reduction of soil filters due to physical clogging. Journal of geotechnical and geoenvironmental engineering, 126(3): 236-246.

Reddi, L.N., Xiao, M., Hajra, M.G., Lee, I.M., 2005. Physical clogging of soil filters under constant flow rate versus constant head. Canadian geotechnical journal, 42(3): 804-811.

Ringleb, J., Sallwey, J., Stefan, C., 2016. Assessment of managed aquifer recharge through modeling—a review. Water, 8(12): 579.

San-Sebastián-Sauto, J., Fernández-Escalante, E., Calero-Gil, R., Carvalho, T., Rodríguez-Escales, P., 2018. Characterization and benchmarking of seven managed aquifer recharge systems in south-western Europe. Sustainable Water Resources Management, 4(2): 193-215.

Sasidharan, S., Bradford, S.A., Šimůnek, J., DeJong, B., Kraemer, S.R., 2018. Evaluating drywells for stormwater management and enhanced aquifer recharge. Advances in water resources, 116: 167-177.

Sasidharan, S., Bradford, S.A., Šimůnek, J., Kraemer, S.R., 2019. Drywell infiltration and hydraulic properties in heterogeneous soil profiles. Journal of hydrology, 570: 598-611.

Sasidharan, S., Bradford, S.A., Šimůnek, J., Kraemer, S.R., 2020. Groundwater recharge from drywells under constant head conditions. Journal of Hydrology, 583: 124569.

Scanlon, B.R. et al., 2006. Global synthesis of groundwater recharge in semiarid and arid regions. Hydrological Processes: An International Journal, 20(15): 3335-3370.

Shammas, M.I., 2008. The effectiveness of artificial recharge in combating seawater intrusion in Salalah coastal aquifer, Oman. Environmental geology, 55(1): 191-204.

Sharma, S.K., Kennedy, M.D., 2017. Soil aquifer treatment for wastewater treatment and reuse. International Biodeterioration & Biodegradation, 119: 671-677.

Shi, X. et al., 2016. The effects of artificial recharge of groundwater on controlling land subsidence and its influence on groundwater quality and aquifer energy storage in Shanghai, China. Environmental earth sciences, 75(3): 195.

Sprenger, C. et al., 2017. Inventory of managed aquifer recharge sites in Europe: historical development, current situation and perspectives. Hydrogeology Journal, 25(6): 1909-1922.

Stephens, D., Neuman, S.P., 1982. Free surface and saturated-unsaturated analyses of borehole infiltration tests above the water table. Advances in Water Resources, 5(2): 111-116.

Taneja, D., Khepar, S., 1996. Effect of Artificial Ground‐Water Recharge on Aquifer Parameters Using Cavity Well. Groundwater, 34(2): 335-340.

Tartakovsky, G.D., Neuman, S.P., 2007. Three‐dimensional saturated‐unsaturated flow with axial symmetry to a partially penetrating well in a compressible unconfined aquifer. Water Resources Research, 43(1).

ToddGroundwater, 2019. M1W Final Title 22 Engineering Report. April,2019.

Tzanakakis, V.A., Paranychianakis, N.V., Angelakis, A.N., 2020. Water supply and water scarcity. Multidisciplinary Digital Publishing Institute.

Vacher, H.L., Hutchings, W.C., Budd, D.A., 2006. Metaphors and models: The ASR bubble in the Floridan aquifer. Groundwater, 44(2): 144-154.

Van Genuchten, M.T., 1980. A closed-form equation for predicting the hydraulic conductivity of unsaturated soils 1. Soil science society of America journal, 44(5): 892-898.

Wang, J. et al., 2012. Field experiments and numerical simulations of confined aquifer response to multi-cycle recharge–recovery process through a well. Journal of hydrology, 464: 328-343.

Wang, T. et al., 2016. Feasibility analysis of using inverse modeling for estimating natural groundwater recharge from a large-scale soil moisture monitoring network. Journal of Hydrology, 533: 250-265.

Wang, W., Sun, X., Xu, Y., 2010. Recent advances in managed aquifer recharge in China, 2010 International Conference on Challenges in Environmental Science and Computer Engineering. IEEE, pp. 516-519.

Wang, X.P., Li, X.R., Xiao, H.L., Berndtsson, R., Pan, Y.X., 2007. Effects of surface characteristics on infiltration patterns in an arid shrub desert. Hydrological Processes: An International Journal, 21(1): 72-79.

Ward, J.D., Simmons, C.T., Dillon, P.J., 2008. Variable-density modelling of multiple-cycle aquifer storage and recovery (ASR): Importance of anisotropy and layered heterogeneity in brackish aquifers. Journal of Hydrology, 356(1-2): 93-105.

WEF, 2019. World Economic Forum. Global Risks Report 2019. Available online: https://www.weforum.org/reports/the-global-risks-report-2019.

Weiß, M., Menzel, L., 2008. A global comparison of four potential evapotranspiration equations and their relevance to stream flow modelling in semi-arid environments. Advances in Geosciences, 18: 15-23.

Westfall, P.H., Arias, A.L., 2020. Understanding regression analysis a conditional distribution approach, Boca Raton. DOI:https://doi.org/10.1201/9781003025764

Xian, Y., Jin, M., Zhan, H., Liu, Y., 2019. Reactive transport of nutrients and bioclogging during dynamic disconnection process of stream and groundwater. Water Resources Research, 55(5): 3882-3903.

Zha, Y. et al., 2019. Review of numerical solution of Richardson–Richards equation for variably saturated flow in soils. Wiley Interdisciplinary Reviews: Water, 6(5): e1364.

Zhang, H., Xu, Y., Kanyerere, T., 2020. A review of the managed aquifer recharge: Historical development, current situation and perspectives. Physics and Chemistry of the Earth, Parts A/B/C: 102887.

Zhang, Y., Zhang, M., Niu, J., Zheng, H., 2016. The preferential flow of soil: A widespread phenomenon in pedological perspectives. Eurasian Soil Science, 49(6): 661-672.

Zheng, X.-l., Shan, B.-b., Chen, L., Sun, Y.-w., Zhang, S.-h., 2014. Attachment–detachment dynamics of suspended particle in porous media: Experiment and modeling. Journal of Hydrology, 511: 199-204.